

DEPARTMENT OF MECHANICAL ENGINEERING  
COLLEGE OF ENGINEERING AND TECHNOLOGY  
OLD DOMINION UNIVERSITY  
NORFOLK, VIRGINIA 23529

**DRAG REDUCTION ON CIRCULAR CYLINDERS BY EJECTING  
JET FROM REAR STAGNATION REGION**

By  
S. Atsuchi, Graduate Research Assistant  
and  
Dr. S.N. Tiwari, Principal Investigator

Progress Report  
For the period ending June 30, 1997

Prepared for  
National Aeronautics and Space Administration  
Langley Research Center  
Hampton, VA 23681-0001

Under  
**Cooperative Agreement NCC1-232**  
Dr. Samuel E. Massenberg, Technical Monitor  
Office of Education  
**ODURF #163631**

**November 1997**



## FOREWORD

This is a progress report on the research work completed on the project "Institute for Scientific and Educational Technology (ISET)." The work was done under the subcategory "Institute for Computational and Applied Mechanics (ICAM)," and specific attention was directed on investigation of "Drag Reduction on Circular Cylinders by Ejecting Jet from Rear Stagnation Region."

The authors extend their sincere thanks to Drs. C. P. Britcher, S. .K. Chaturvedi, A. O. Demuren, A. S. Kheireddine, and A. C. Taylor for many useful and constructive suggestions during the course of this study and in the preparation of the final manuscript. Sincere thanks are also extended to T. M. Galloway, C. Contreras, V. Kalburgi, and J. Robertson for their support in conducting the experiments at Old Dominion University.

This work, in part, was supported by the NASA Langley Research Center through the Cooperative Agreement NCC1-232. The Cooperative Agreement was monitored by Dr. Samuel E. Massenberg, Director, Office of Education, Mail Stop 400, NASA Langley Research Center, Hampton, Virginia 23681-0001.

## **DRAG REDUCTION ON CIRCULAR CYLINDERS BY EJECTING JET FROM REAR STAGNATION REGION**

**S. Atsuchi and S. N. Tiwari**

### **SUMMARY**

Extensive work in the field of drag reduction has been done in the past. However, this field of study is highly desirable today because of various high-speed research programs. The present study attempts to investigate the feasibility of drag reduction on a cylinder by flow injection from the rear stagnation region. A two-dimensional circular cylinder at Reynolds number  $1 \times 10^5$  with a jet ejected from its tail is selected as a physical model. To tackle this problem, a numerical simulation as well as an experimental approach were used. Despite the recent development of computational fluid dynamics (CFD), computing a flow around a cylinder at a high Reynolds number is still difficult and expensive because of the massive separated region. A commercial CFD code was used in the present study after the various validations and sensitive analyses were performed. Full Navier-Stokes equations were solved in this code by the finite volume method and SIMPLE algorithm. To maximize the advantage of the implicit scheme used in the CFD code and to reduce the computational time, the computation was made under the steady-state assumption. On the other hand, a static pressure measurement and a smoke wire visualization were conducted to observe the effect of the jet experimentally. It is found that the drag can be reduced by relatively small amount of the jet ejection. When the drag is decreased the pressure in the downstream portion of the cylinder is increased. This augmentation extends from the rear stagnation point to about  $\pm 120^\circ$  where the minimum pressure is observed, while the jet has little effect on the front portion of the cylinder. It is also found that the flow behind the cylinder becomes rather symmetric when the drag reduction is being made. The numerical results show the same trend and reinforce the experimental results.

# TABLE OF CONTENTS

	<u>Page</u>
SUMMARY .....	iv
LIST OF TABLES .....	viii
LIST OF FIGURES .....	ix
LIST OF SYMBOLS .....	xii
 <u>Chapter</u>	
I. INTRODUCTION .....	1
II. THEORETICAL FORMULATION .....	5
2.1 Physical Problem .....	5
2.2 Governing Equations.....	8
2.2.1 Conservation equations .....	8
2.2.2 Pressure, Drag and Lift Coefficient.....	9
2.2.3 Strouhal Number .....	11
2.2.4 Jet-Blowing Momentum Coefficient.....	12
III. NUMERICAL PROCEDURE .....	13
3.1 REFLAN3D .....	13
3.2 Fluent .....	13
3.2.1 Discretization Equations .....	13
3.2.2 The SIMPLE Algorithm .....	16
3.2.3 The QUICK Scheme .....	18
3.2.4 Grid System .....	19
3.2.5 Boundary Conditions .....	24
3.2.6 Time Step .....	24
3.2.7 Residual.....	26
IV. EXPERIMENTAL ARRANGEMENT .....	28
4.1 Test Facility .....	28
4.2 Test Models .....	28

	<u>Page</u>
4.3 Static Pressure Measurement .....	33
4.4 Smoke Wire Visualization.....	34
V. COMPUTER CODE INVESTIGATION .....	36
5.1 Grid Topology Study.....	36
5.2 Reynolds Number Effect.....	43
5.3 Steady and Unsteady Computations .....	47
5.3.1 Drag Coefficient, Lift Coefficient and Residual History .....	47
5.3.2 Pressure Distributions .....	49
5.3.3 Streamlines.....	49
5.3.4 Velocity Vectors .....	58
5.4 Grid Size Dependency .....	58
5.5 Effect of Area of Physical Domain .....	58
VI. RESULTS AND DISCUSSION .....	67
6.1 Numerical Results.....	67
6.1.1 Pressure Distribution.....	67
6.1.2 Drag Coefficient and separation point .....	67
6.1.3 Streamlines.....	70
6.1.4 Velocity Vectors .....	75
6.2 Experimental Results .....	75
6.2.1 Static Pressure Measurement .....	75
6.2.2 Smoke Wire Visualization.....	86
6.3 Selected Comparative Study .....	86
6.3.1 No-Jet Case .....	86
6.3.2 Jet Case .....	89
6.3.3 Flow Field Pattern .....	89
VII. CONCLUSIONS AND RECOMMENDATIONS .....	92
REFERENCES .....	94
APPENDIX.....	98
A. REFLAN3D .....	99
A.1 Governing Equations.....	99

Page

A.2 Discretization of the Governing Equation.....	102
A.3 Modification for Non-Orthogonal Grid.....	104

## LIST OF TABLES

<u>Table</u>	<u>Page</u>
2.1 Conservation terms corresponding to Eq. (2.10) .....	10
5.1 Comparison of the time-averaged drag coefficient and Strouhal number for different grid systems ( $Re = 1 \times 10^5$ ) .....	40
5.2 Time-averaged drag coefficient and the Strouhal number at $Re = 1 \times 10^3$ .....	45
5.3 Comparison of the drag coefficient for steady and unsteady calculations .....	51
5.4 Comparison of the drag coefficient for the different grid sizes .....	64
5.5 Comparison of the drag coefficient for the different size of computational areas .....	66
A.1 Conservation terms corresponding to Eq. (A.1) .....	100

## LIST OF FIGURES

<u>Figure</u>	<u>Page</u>
2.1 Physical model for two-dimensional flow past a cylinder with jet .....	6
3.1 Non-staggered control volume.....	15
3.2 Body fitted rectangular grid system around a circular cylinder .....	20
3.3 O-type grid system around a circular cylinder.....	21
3.4 Improved O-type grid system around a circular cylinder .....	22
3.5 Boundary conditions for the body fitted rectangular grid system.....	25
3.6 Boundary conditions for the O-type grid systems .....	25
4.1 Schematic of Old Dominion University three by four foot low speed wind tunnel .....	29
4.2 Wind tunnel test model "A" .....	30
4.3 Wind tunnel test model "B" .....	31
4.4 Photograph of the model "B" in the Old Dominion University low-speed wind tunnel .....	32
4.5 Camera set up for smoke wire flow visualization .....	35
5.1 Time history of the drag coefficient for different grid systems.....	37
5.2 Time history of the lift coefficient for different grid systems .....	38
5.3 Comparison of pressure distributions along a circular cylinder at $Re = 1 \times 10^5$ for different grid systems .....	41
5.4 Time history of the drag coefficient at $Re = 1 \times 10^3$ .....	44
5.5 Time history of the lift coefficient at $Re = 1 \times 10^3$ .....	44
5.6 Comparison of pressure distributions along a circular cylinder at $Re = 1 \times 10^3$ and $Re = 1 \times 10^5$ .....	46
5.7 Drag and lift coefficient with number of iteration for $Re = 1 \times 10^5$ case .....	48
5.8 Residual history with number of iteration for $Re = 1 \times 10^5$ case .....	48
5.9 Drag and lift coefficient with number of iteration for $Re = 1 \times 10^3$ case .....	50
5.10 Residual history with number of iteration for $Re = 1 \times 10^3$ case .....	50



<u>Figure</u>	<u>Page</u>
5.11 Comparison of pressure distributions along a cylinder at $Re = 1 \times 10^5$ obtained from steady and unsteady calculations .....	52
5.12 Comparison of pressure distributions along a cylinder at $Re = 1 \times 10^3$ obtained from steady and unsteady calculations .....	53
5.13 Streamlines from the unsteady computation at $Re = 1 \times 10^5$ .....	54
5.14 Streamlines from the steady computation at $Re = 1 \times 10^5$ .....	55
5.15 Streamlines from the unsteady computation at $Re = 1 \times 10^3$ .....	56
5.16 Streamlines from the steady computation at $Re = 1 \times 10^3$ .....	57
5.17 Velocity vectors from the unsteady computation at $Re = 1 \times 10^5$ .....	59
5.18 Velocity vectors from the steady computation at $Re = 1 \times 10^5$ .....	60
5.19 Velocity vectors from the unsteady computation at $Re = 1 \times 10^3$ .....	61
5.20 Velocity vectors from the steady computation at $Re = 1 \times 10^3$ .....	62
5.21 Comparison of pressure distributions along a cylinder at $Re = 1 \times 10^5$ for different size of grids .....	63
5.22 Comparison of pressure distributions along a cylinder at $Re = 1 \times 10^5$ for different size of computational areas .....	65
6.1 Variations of pressure distribution with jet-blowing momentum coefficient $C_\mu$ .....	68
6.2 Variation of the drag coefficient and the separation point with the jet-blowing momentum coefficient $C_\mu$ .....	69
6.3 Streamlines for the no-jet case .....	71
6.4 Streamlines for the $C_\mu = 0.0005$ case .....	72
6.5 Streamlines for the $C_\mu = 0.004$ case .....	73
6.6 Streamlines for the $C_\mu = 0.05$ case .....	74
6.7 Velocity vectors for the no-jet case .....	76
6.8 Velocity vectors for the $C_\mu = 0.0005$ case .....	77
6.9 Velocity vector for the $C_\mu = 0.004$ case .....	78
6.10 Velocity vector for the $C_\mu = 0.05$ case .....	79
6.11 Pressure distributions along 3"-diameter cylinder (model "A") .....	80
6.12 Effect of the jet on pressure distribution .....	81

<u>Figure</u>	<u>Page</u>
6.13 Variation of the drag coefficient with Reynolds number for the non-jet cases .....	84
6.14 Variations of the drag coefficient with $C_\mu$ and Reynolds number .....	85
6.15 Smoke wire visualization of the flow field behind the cylinder.....	87
6.16 Comparison of pressure distributions from the numerical and experimental results for the non-jet cases .....	88
6.17 Comparison of the variations of the drag coefficient from the numerical and experimental results.....	90
6.18 Streak lines from the numerical results.....	91
A.1 Staggered grid with “backward boomerang” arrangement.....	101
A.2 Non-orthogonal grid.....	105

## LIST OF SYMBOLS

Unless otherwise stated the listed symbols are specified as follows.

$A$	area of cell face
$a$	convection/diffusion coefficient (in discretized equation)
$C_p$	pressure coefficient
$C_D$	drag coefficient
$C_L$	lift coefficient
$C_\mu$	blowing-jet momentum coefficient
$d$	cylinder diameter
$p$	pressure
$q$	dynamic pressure ( $\frac{1}{2}\rho u^2$ )
$Re$	Reynolds number
$S$	source
$t$	time
$u$	x-directional velocity component
$v$	y-directional velocity component
$V$	volume of control volume
$w_{slit}$	jet slit width
$\delta C_p$	uncertainty of pressure coefficient
$\theta$	angle from the front stagnation point [Rad]
$\rho$	density
$\sigma$	standard deviation
$\phi$	general field property function

### Subscript

$E, N, S, W$	neighboring cell centers (East, North, South, West)
$e, n, s, w$	cell face (east, north, south, west)
$f$	friction
$j$	jet condition
$P$	cell center
$p$	pressure
$\infty$	upstream condition

## Superscript

$n$	time level
$*$	guessed value
$'$	correction value

## Chapter I

### INTRODUCTION

The study of flow around a circular cylinder is one of the most classical problem in fluid dynamics. This is mainly because the mathematical analysis can be applied relatively easily to this problem for an ideal fluid case and because the geometry is simple. However, despite the geometrical simplicity, the fluid dynamical description of this problem is very complicated. The flow is, in general, asymmetric and unsteady. Moreover, it is known that there exists a three-dimensionality in the spanwise direction in real flows. On the other hand, because of its simple shape, a circular cylinder is a very common shape for practical applications: from a chimney to a fuselage of air plane. However, it is known that a circular cylinder has a very high drag coefficient, which means that it is not a suitable shape in a fluid dynamical sense. One should also note the adverse effect of its oscillation in flow due to the vortex shedding or the Karman vortex street behind a cylinder.

In aerospace engineering, drag reduction is an essential issue; and extensive study in this field has been done in the past. The cylindrical shape and bluff body configuration have been identified as important shapes for aerodynamic consideration. A high speed space vehicle must have a blunt body shape to overcome the aerodynamic heating. Therefore, this field of study has been highly desirable. The present study attempts to investigate the feasibility of drag reduction on a cylinder by flow injection from the rear stagnation region.

James et al. [1]\* extensively studied cross flow on circular cylinders at Reynolds number from  $1.5 \times 10^5$  to  $1.09 \times 10^7$ . They measured the pressure distribution along the cylinder surface including time-dependent and spanwise data. Furthermore, they discussed the effect of surface roughness in detail. They also measured Strouhal number by means of identifying a distinct spike in the frequency distribution of velocity fluctuation measured

---

\*The journal mode adapted for this thesis is AIAA. The numbers in brackets indicate references.

by a hot wire anemometer. Achenbach [2] measured skin friction experimentally by differentiating two adjacent pressures in a very small probe. He clarified the proportion of the drag due to skin friction to the total drag as a function of Reynolds number between  $6 \times 10^4$  and  $5 \times 10^6$ . Humphreys [3], on the other hand, utilized strain-gauges to obtain the drag and lift coefficients directly at high Reynolds numbers. Cantwell and Coles [4] conducted extensive research on the structure of the wake of a circular cylinder. "Flying-hot-wire" technique has been developed to increase the data accuracy of hot-wire anemometer by increasing the relative velocity. The instantaneous velocity vector, vorticity, mean Reynolds normal stress and mean Reynolds shearing stress were experimentally measured at Reynolds number  $1.4 \times 10^5$ .

Many numerical investigations have also been conducted [5-9]. However, computations are limited to very high Reynolds number cases due to numerical difficulties. Thoman and Szewczyk [8] simulated time-dependent viscous flow over a circular cylinder at a wide range of Reynolds number from 1 to  $3 \times 10^5$ . They employed the incompressible vorticity transport equation with the finite difference method. The hybrid mesh cell structure was used to fit the boundaries. The cell size next to the surface was chosen to 1/12 of the steady-state forward stagnation point boundary-layer thickness. Ishii et al. [9] focused their computation of a circular cylinder near the critical range of Reynolds number. A large computation was accomplished with  $481 \times 120$  grid points distributed on the C-grid. The smallest grid size next to the cylinder wall was 0.00001 of its diameter. The time-dependent full Navier-Stokes equation (compressible with the Mach number of 0.3) was solved by the improved Beam-Warming-Steger method, where no turbulent model was employed. The computation was conducted from  $Re = 1 \times 10^5$  to  $Re = 7.83 \times 10^6$ . The time step was set to 0.003. They successfully reproduced the flow pattern and "the drag crisis" in the transition Reynolds number regime; however, the computation time was about 7 to 9 hours for one case on the HITACHI S810/20 computer and it is still very expensive [10].

While considerable studies have been conducted by making a two-dimensional assumption numerically and experimentally in this area, the significance of three-dimensionality has also been reported [11, 12]. Beaudan and Moin [13] simulated cross flow past a circular cylinder and pointed out that "three-dimensional computations are

essential for predicting flow statistics of engineering interest" at Reynolds number as low as 3900. However, computational cost is still considered as an important engineering aspect even though computer technology has been developed quite rapidly.

Many theoretical, experimental and computational investigations in the field of drag reduction have conducted [14-23]. It is known that a splitter plate behind a cylinder causes the drag to be reduced. Apelt et al. [15] experimentally investigated the effect of a splitter plate, whose length was less than twice of the cylinder diameter, on the pressure distribution, drag and the vortex shedding at Reynolds number  $1 \times 10^4$  to  $5 \times 10^4$ . They pointed out three effects: (1) stabilizing the separation points, (2) making a wake narrower and (3) raising the base pressure. It was also noted that the plate had a lesser effect on the Strouhal number. Cete and Unal [17], on the other hand, numerically investigated the effect of a splitter plate.

Shrader and Duke [18] and Mo and Duke [19] examined the effect of a rear stagnation jet on the wake behind cylinder at Reynolds number from  $6 \times 10^2$  to  $2.5 \times 10^3$ . They performed experimental visualization to see the condition of the separation point on the cylinder. They also used numerical approach to confirm their experimental result, where the Navier-Stokes equations in primitive variables were solved. The drag coefficient data and pressure distribution along the surface were presented. It was found that as the jet velocity increases, the drag also increases, because the pressure on the rear side of the cylinder decreases due to favorable pressure gradient caused by the jet. However, the unsymmetrical wake flow becomes symmetrical and the cylinder is stabilized by blowing the rear stagnation jet with a velocity ratio  $u_j/u_\infty$  as low as 1.

The advantage of using the splitter plates is that no power source is required; and a significant drag reduction can be achieved by placing a relatively small plate. It can be easily mounted on an existing system with no or a little modification. However, this method is not suitable for cases where a cylinder has a non-zero angle of attack. The splitter plate has less capability to adjust its direction in the flow; the advantage of the simplicity will be lost if some mechanism is installed to adjust its direction. Moreover, it is difficult to control the amount of the effect of the plate. On the other hand, jet-blowing method is capable to change its direction as well as its strength; and, more importantly, the jet can be activated only when it is needed without any geometrical change. Furthermore,

to obtain jet or compressed air, especially on an aircraft, is relatively easy. Therefore, if the drag can be reduced without losing power (a turbine engine loses power by bleeding, for example), the drag reduction technique by means of ejecting jet from the rear stagnation region will be very useful. In other words, by using compressed air from a turbine engine and ejecting it from the rear stagnation region, it is possible to reduce the drag and/or stabilize the flow. The present study attempts to investigate the feasibility of drag reduction on a cylinder by flow injection from the rear stagnation region.

The contents of this study are presented in seven chapters. In Chap. II theoretical formulation is given, where physical set up and flow characteristics are described in detail. A derivation of the governing equations are also provided. In The numerical procedures used in the study are discussed in Chap. III. The grid systems, boundary conditions and time steps used are presented, and the numerical algorithm and scheme are discussed. Elements of the experimental study are given in Chap. IV. Extensive computer code validations are conducted in Chap. V. An extensive investigation of numerical simulation on a circular cylinder without the jet is presented prior to computing the jet cases. The results are presented in Chap. VI. Numerical results of the jet cases are discussed first, and then the results of the experiment are presented. Next, several cases are selected for comparison between the numerical results and the experimental data. Finally, conclusions of this study are presented in Chap. VII where certain recommendations for further study are also provided.



## Chapter II

### THEORETICAL FORMULATION

In this chapter, a discussion of the physical problem and information on essential governing equations are provided.

#### 2.1 Physical Problem

In this section, various aspects of the physical problem are described. To reduce computational and interpretational difficulties, the problem is considered as two-dimensional; however, three-dimensionality cannot be ignored to match the computational results with the experimental results perfectly as mentioned in Chap. I. The schematic of the physical model is illustrated in Fig. 2.1. A two-dimensional circular cylinder is placed in a uniform flow stream. A two-dimensional jet is ejected from the rear stagnation point in the down stream direction. To observe the effect of the strength of the jet, the jet velocity is varied while the area of the slit is fixed.

Reynolds number based on the cylinder diameter and the upstream velocity is initially set to 100,000. At this Reynolds number for a circular cylinder, the velocity boundary layer profile is assumed to be laminar up to the separation point. Potential theory states that the ideal velocity distribution along the surface is given by

$$u(\theta) = 2u_{\infty} \sin \theta \quad (2.1)$$

while the pressure coefficient  $C_p$  along the surface can readily be obtained by employing the Bernoulli's equation as

$$C_p = 1 - 4(\sin \theta)^2 \quad (2.2)$$

By applying the Blasius series[24], the separation point  $\theta_s$  can be computed based on the concept that the shearing stress on the wall is zero at the point of separation,

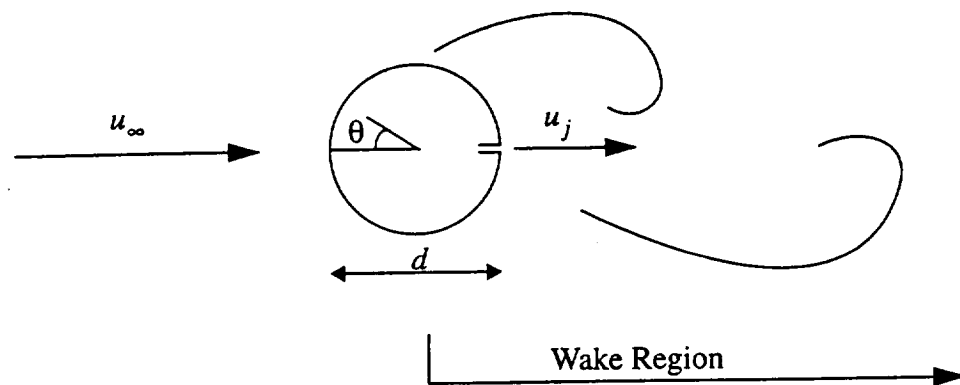


Fig. 2.1 Physical model for two-dimensional flow past a cylinder with jet.

$$\tau_{wall} = \mu \left( \frac{\partial u}{\partial y} \right)_{wall} = 0 \quad (2.3)$$

This provides the value of  $\theta_s$  as  $\theta_s = 108.8^\circ$ . The flow over the cylinder is accelerated from the front stagnation point to the downstream. After passing the minimum pressure point ( $\theta=90^\circ$ , theoretically), the flow experiences adverse an pressure gradient. This adverse pressure gradient causes the velocity profile to have an inflection point which is unstable. Finally, the velocity gradient at the wall becomes zero and the flow is no longer attached beyond that point. This point is the point of separation.

It is known that the separation point varies with the Reynolds number in real flows. The separation point (laminar separation point) is located approximately  $80^\circ$  for  $Re=5 \times 10^4 \sim 1 \times 10^5$  [1,2]. Moreover, the above discussions are based on a steady state assumption; however, the flow in this Reynolds number range (and above) is essentially unsteady. Therefore, the values mentioned heretofore and hereafter must be understood as a time averaged values unless stated otherwise. The Strouhal number, whose definition and meaning are described in the next section, is almost constant with a value of 0.2 in this Reynolds number regime [4].

As the Reynolds number increases to the critical range (or the transition range) which is about  $2 \times 10^5 \sim 5 \times 10^5$ , the boundary layer is assumed to transient to turbulent. This critical Reynolds number varies from case to case within the range roughly mentioned above [4]. This variation depends upon several factors such as the surface roughness [1], the upstream turbulent length scale [25] and so forth. In this critical regime, the flow characteristic values such as the pressure distribution along the surface, the drag coefficient, the Strouhal number, and the separation point change discontinuously from their values in the subcritical range. Moreover, it is reported by Kamiya et al. [26] that the flow shows hysteresis effects.

When the Reynolds number increases further, the boundary layer profile becomes fully turbulent, and the flow appears to be relatively steady. Moreover, due to the massive momentum exchange within the turbulent boundary layer, the flow remains attached longer than the laminar case. Thus the separation point (turbulent separation point) moves downstream to approximately  $120^\circ$  [1,2]. Most importantly, as a result, the drag

coefficient decreases dramatically. The dimple of a golf ball is a well known example of the effect. A golf ball with dimples which cause the flow to become turbulent flies farther than the one without dimples. Furthermore, the flow variables cited above change continuously with respect to the Reynolds number. This range is called the supercritical range.

Many investigations have been performed especially in the vicinity of the critical/transition Reynolds number experimentally as well as numerically [8,9,14].

In this study, the Reynolds number is varied from  $1 \times 10^5$  to  $3 \times 10^5$ .

## 2.2 Governing Equations

### 2.2.1 Conservation Equations

The time-dependent governing equations for the mass continuity, x- and y-momentum transport in two-dimensional Cartesian coordinates are given as

$$\frac{\partial \rho}{\partial t} + \frac{\partial}{\partial x}(\rho u) + \frac{\partial}{\partial y}(\rho v) = 0 \quad (2.4)$$

$$\frac{\partial}{\partial t}(\rho u) + \frac{\partial}{\partial x}(\rho u^2) + \frac{\partial}{\partial y}(\rho uv) = -\frac{\partial p}{\partial x} + \frac{\partial \tau_{xx}}{\partial x} + \frac{\partial \tau_{xy}}{\partial y} + \rho B_x \quad (2.5)$$

$$\frac{\partial}{\partial t}(\rho v) + \frac{\partial}{\partial x}(\rho uv) + \frac{\partial}{\partial y}(\rho v^2) = -\frac{\partial p}{\partial y} + \frac{\partial \tau_{xy}}{\partial x} + \frac{\partial \tau_{yy}}{\partial y} + \rho B_y \quad (2.6)$$

where  $\tau$  is shear stress and  $B$  is body force. For Newtonian fluid with, constant density and viscosity, and for the flow with no body force, Eqs. (2.4) to (2.6) can be expressed as

$$\frac{\partial u}{\partial x} + \frac{\partial v}{\partial y} = 0 \quad (2.7)$$

$$\frac{\partial}{\partial t}(\rho u) + \frac{\partial}{\partial x}(\rho u^2) + \frac{\partial}{\partial y}(\rho uv) = -\frac{\partial p}{\partial x} + \mu \left( \frac{\partial^2 u}{\partial x^2} + \frac{\partial^2 u}{\partial y^2} \right) \quad (2.8)$$

$$\frac{\partial}{\partial t}(\rho v) + \frac{\partial}{\partial x}(\rho uv) + \frac{\partial}{\partial y}(\rho v^2) = -\frac{\partial p}{\partial y} + \mu \left( \frac{\partial^2 v}{\partial x^2} + \frac{\partial^2 v}{\partial y^2} \right) \quad (2.9)$$

Equations (2.7)-(2.9) can be simplified by denoting the dependent variable as  $\phi$ . Thus the governing differential equation in general form is written as

$$\frac{\partial}{\partial t}(\rho\phi) + \nabla(\rho\vec{V}\phi) = \nabla[\Gamma_\phi(grad\phi)] + S_\phi \quad (2.10)$$

The corresponding values for  $\phi$ ,  $\Gamma_\phi$  and  $S_\phi$  are listed in Table 2.1.

### 2.2.2 Pressure, Drag and Lift Coefficient

The pressure coefficient  $C_p$  is given as

$$C_p = \frac{p - p_\infty}{(1/2)\rho u_\infty^2} \quad (2.11)$$

while the drag coefficient  $C_D$  is composed of pressure forces and friction forces, that is,

$$C_D = C_{Dp} + C_{Df} \quad (2.12)$$

Achenbach [2] measured  $C_{Dp}$  and  $C_{Df}$  in Eq. (2.12) simultaneously, and showed the contribution of the each term to the total drag coefficient  $C_D$ . According to his investigation, in the Reynolds number range of the present study, the drag due to the friction forces (the second term in Eq. (2.12)) is about 1% of the total drag coefficient. Therefore it is assumed that

$$C_D \approx C_{Dp} \quad (2.13)$$

where

$$C_{Dp} = \oint \frac{(p - p_\infty) \cos \theta}{(1/2)\rho u_\infty^2 d} dA \quad (2.14)$$

and the cyclic integral is taken along the cylinder.

The lift coefficient is defined in the same manner as the drag coefficient, that is,

$$C_L = C_{Lp} + C_{Lf} \quad (2.15)$$

Table 2.1 Conservation terms corresponding to Eq. (2.10)

Equation	$\phi$	$\Gamma_\phi$	$S_\phi$
mass	1	$\rho$	0
x-momentum	$u$	$\mu$	$\frac{\partial p}{\partial x} + S_x$
y-momentum	$v$	$\mu$	$\frac{\partial p}{\partial y} + S_y$

Neglecting the second term on the right hand side,

$$C_L \approx C_{Lp} \quad (2.16)$$

where

$$C_{Lp} = \oint \frac{(p - p_\infty)(-\sin\theta)}{(1/2)\rho u_\infty^2 d} dA \quad (2.17)$$

The integrations in Eqs. (2.14) and (2.17) are replaced by summations to use the values from discrete pressure data point, that is,

$$C_{Dp} = \sum_i \frac{(p_i - p_\infty)\cos\theta_i}{(1/2)\rho u_\infty^2 d} (\Delta A)_i \quad (2.18)$$

and

$$C_{Lp} = \sum_i \frac{(p_i - p_\infty)(-\sin\theta_i)}{(1/2)\rho u_\infty^2 d} (\Delta A)_i \quad (2.19)$$

Twenty nine sample points were used to compute  $C_{Dp}$  and  $C_{Lp}$  for the numerical results, while 90 points for the non-jet case and 35 points for the jet case were used in the experimental investigation.

### 2.2.3 Strouhal Number

Strouhal number  $St$  is expressed as a dimensionless frequency and is given as

$$St = \frac{fd}{u_\infty} \quad (2.20)$$

where  $f$  is the vortex shedding frequency. The Strouhal number is a very important parameter for flows around a bluff body which sheds vortices into the downstream. In general, this vortex shedding dominates dynamic flow properties in the flows. In particular, it is well known fact for a circular cylinder case that shed vortices form a Karman vortex street behind the cylinder with almost constant Strouhal number at a fixed Reynolds number. As mentioned in the previous section, the Strouhal number remains approximately constant at 0.2 in the range  $Re = 10^4 \sim 10^5$ .

### 2.2.4 Jet-Blowing Momentum Coefficient

To evaluate and normalize the strength of the jet, blowing-jet momentum coefficient,  $C_\mu$ , is employed as [20-23]

$$C_\mu = \frac{\rho_j w_{slit} u_j^2}{(1/2)\rho_\infty u_\infty^2 d} \quad (2.21)$$

In this study,  $\rho_j$  is the same as  $\rho_\infty$ . Therefore, the strength of the jet is normalized with respect to the cylinder diameter and the uniform velocity.



## Chapter III

### NUMERICAL PROCEDURE

In this chapter, numerical procedure is described. First, a brief comment is made about REFLAN3D which has been investigated for its feasibility as a computational source code for this study. In the next section, theoretical backgrounds of a computational fluid dynamics code (Fluent) are presented. Finally, the other numerical considerations such as grid system, boundary conditions and time steps are described.

#### 3.1 REFLAN3D

REFLAN3D (REactive FLOW ANalyzer 3-Dimensional) was originally developed for predicting three-dimensional two-phase spray flow and combustion in rocket engines [27]. The details of this computer code are described in Appendix A. Despite the fact that this code is stated to handle three-dimensional flows, there are some bugs in the code when non-axisymmetric flows are solved. In this code, uses of generalized curvilinear coordinates are not allowed. Also, the code is designed for internal flows. Because of these reasons, a commercial computational fluid dynamics code (Fluent) described below has been used for numerical investigation.

#### 3.2 Fluent

In the following sections, theoretical formulations of Fluent are described.

##### 3.2.1 Discretization Equation

The generalized governing equation is written as Eq.(2.10). Time integration of the transient term can be discretized as [28]

$$\int_t^{t+\Delta t} \frac{\partial}{\partial t}(\rho\phi) dt = (\rho\phi)^{n+1} - (\rho\phi)^n \quad (3.1)$$

where  $n$  is the time level. The time integration of the other terms in Eq. (2.10) can be obtained, in general, as

$$\int_t^{t+\Delta t} (\rho u \phi) dt = [f(\rho u \phi)^{n+1} + (1-f)(\rho u \phi)^n] \Delta t \quad (3.2)$$

where  $f$  is the factor to determine whether the scheme is an explicit or implicit in time. For  $f=0$ , the scheme becomes an explicit. Fluent assumes that  $f=1$ , which corresponds to a fully implicit scheme. Hence,

$$\int_t^{t+\Delta t} (\rho u \phi) dt = f(\rho u \phi)^{n+1} \Delta t \quad (3.2a)$$

The advantage for the implicit scheme is that it is unconditionally stable; however, it requires to solve a system of equations simultaneously [10]

Volume integration for the space derivatives can be obtained by employing the Divergence theorem as

$$\int_V \nabla(\rho \vec{V} \phi) dV = \int_A (\rho \vec{V} \phi) dA \quad (3.3)$$

where  $V$  is the volume of the control volume and  $A$  is the area of the control surface. After discretizing the integral on the control volume shown in Fig. 3.1, the space derivative terms in Eq. (2.10), for example in the x-direction, become

$$\begin{aligned} & (\rho u \phi A)_e - ((\rho u \phi A)_w + (\rho u \phi A)_n - (\rho u \phi A)_s) \\ &= \left[ \Gamma_\phi \frac{(\phi_e - \phi_p)}{\Delta x} A \right]_e - \left[ \Gamma_\phi \frac{(\phi_p - \phi_w)}{\Delta x} A \right]_w \\ &+ \left[ \Gamma_\phi \frac{(\phi_n - \phi_p)}{\Delta y} A \right]_n - \left[ \Gamma_\phi \frac{(\phi_p - \phi_s)}{\Delta y} A \right]_s + S_\phi A \end{aligned} \quad (3.4)$$

where  $S_\phi$  is the source term which can be expressed as (if there is no body force)

$$S_\phi = -(p_e - p_w) \quad (3.5)$$

For two-dimensional case,  $A$  is the control surface area in a unit depth. Combining Eqs. (3.1) to (3.4),

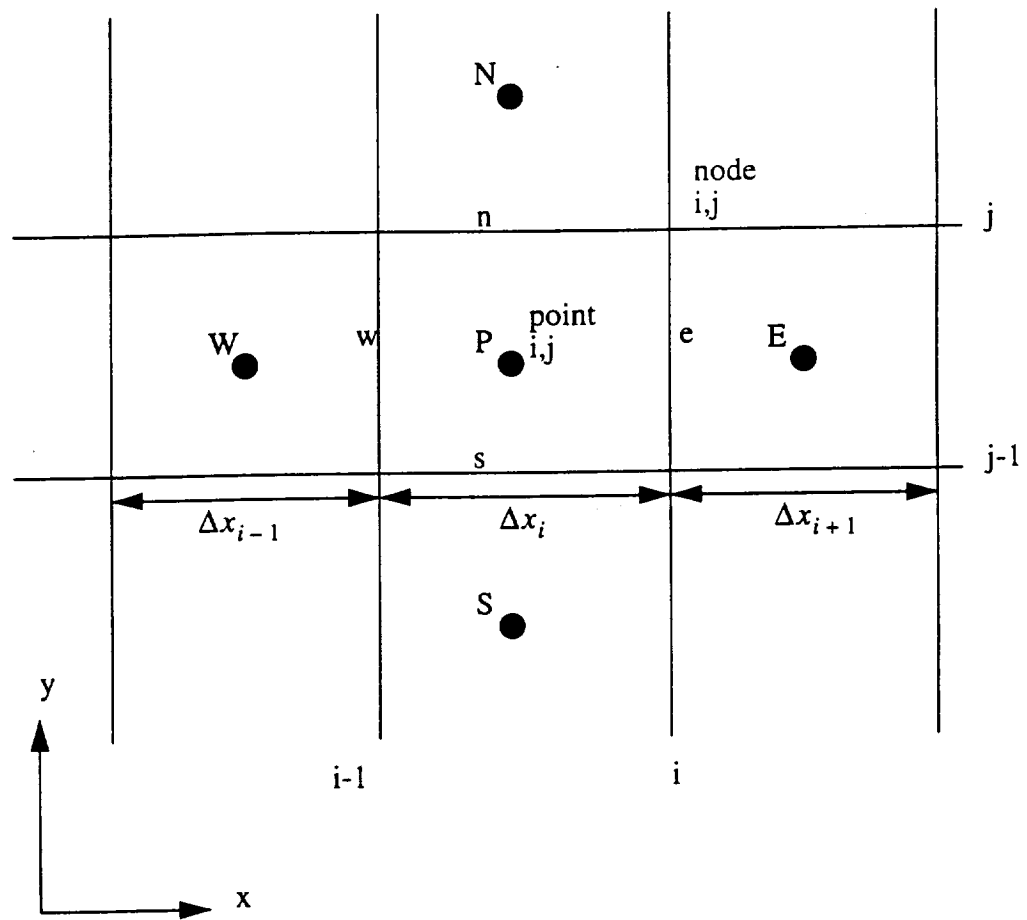


Fig. 3.1 Non-staggered control volume

$$\begin{aligned}
& \frac{(\rho\phi V)_p^{n+1} - (\rho\phi V)_p^n}{\Delta t} \\
& + (\rho u\phi)_e^{n+1} - (\rho u\phi)_w^{n+1} + (\rho u\phi A)_n^{n+1} - (\rho u\phi A)_s^{n+1} \\
& = \left[ \Gamma_\phi \frac{(\phi_e - \phi_p)}{\Delta x} A \right]_e^{n+1} - \left[ \Gamma_\phi \frac{(\phi_p - \phi_w)}{\Delta x} A \right]_w^{n+1} \\
& + \left[ \Gamma_\phi \frac{(\phi_n - \phi_p)}{\Delta y} A \right]_n^{n+1} - \left[ \Gamma_\phi \frac{(\phi_p - \phi_s)}{\Delta y} A \right]_s^{n+1} \\
& - S_\phi^{n+1} A
\end{aligned} \tag{3.6}$$

By collecting the terms in Eq. (3.6) with respect to the location, the equation can be expressed as an algebraic equation, that is,

$$a_p \phi_p = \dot{M}^{old} \phi_p^{old} + a_e \phi_e + a_w \phi_w + a_n \phi_n + a_s \phi_s + S_\phi \tag{3.7}$$

where

$$\dot{M}^{old} = (\rho V)^{old}$$

which corresponds to n-level in time in Eq. (3.7), while the other terms in the equation are evaluated at (n+1)-level in time. Finally Eq. (3.7) can be written in a shortened notation as

$$a_p \phi_p = \sum_{nb} a_{nb} \phi_{nb} + S_\phi + \dot{M}^{old} \phi_p^{old} \tag{3.8}$$

where the subscript nb refers to neighboring points.

### 3.2.2 The SIMPLE Algorithm

From Eqs. (3.5) and (3.8), the momentum equations are written as

$$x: a_p u_p = \sum_{nb} a_{nb} u_{nb} + (p_w - p_e)A + (\dot{M}^{old} \phi_p^{old})_x \tag{3.9a}$$

$$y: a_p v_p = \sum_{nb} a_{nb} v_{nb} + (p_n - p_s)A + (\dot{M}^{old} \phi_p^{old})_y \tag{3.9b}$$

In general, the velocities obtained from Eqs. (3.9) do not satisfy the continuity equation

until correct pressure values are substituted in the source terms of the equation. To overcome this problem, the continuity equation is employed to obtain the correct pressure values thus in turn the correct velocities which satisfy the continuity equation. This algorithm is called as the SIMPLE (Semi-Implicit Method for Pressure-Linked Equations) algorithm developed by Patankar and Spalding [29].

The algorithm starts with substitution of a guessed pressure field,  $p^*$ , into the momentum equations. Equations (3.9) yield the guessed values for velocities  $u_p^*$  and  $v_p^*$ . These guessed values are related as

$$u_p = u_p^* + u'_p \quad (3.10a)$$

$$v_p = v_p^* + v'_p \quad (3.10b)$$

The guessed values for pressure, at the east face for example, are related as

$$p_e = p_e^* + p'_e \quad (3.11)$$

where prime represents correction values. Substitution of Eqs. (3.10) and (3.11) into Eqs. (3.9), followed by subtraction of Eqs. (3.9) with the guessed values such as  $u^*$ ,  $v^*$  and  $p^*$  yields

$$x: a_p u'_p = \sum_{nb} a_{nb} u'_{nb} + (p'_w - p'_e)A \quad (3.12a)$$

$$y: a_p v'_p = \sum_{nb} a_{nb} v'_{nb} + (p'_n - p'_s)A \quad (3.12b)$$

From Eqs. (3.9), velocity corrections are related to the pressure corrections such that

$$x: u'_p = \frac{1}{A_p} (p'_w - p'_e)A \quad (3.13a)$$

$$y: v'_p = \frac{1}{A_p} (p'_w - p'_e)A \quad (3.13b)$$

In Eqs. (3.13), indirect or implicit influence of the pressure correction on velocity, that is,  $\sum_{nb} a_{nb} u'_{nb}$  and  $\sum_{nb} a_{nb} v'_{nb}$  are omitted for simplification; however, these terms will

vanish when convergence is achieved.

To obtain correction terms of pressure (the primed value), the discretized continuity equation is employed, that is,

$$(\rho u A)_e - (\rho u A)_w + (\rho v A)_n - (\rho v A)_s = 0 \quad (3.14)$$

In Eq. (3.14),  $u$  and  $v$  are replaced by the starred (\*) and primed (') values using Eq. (3.10). Moreover, the primed values are represented by the pressure correction terms through Eqs. (3.13). Finally, the pressure correction equation can be expressed as

$$\begin{aligned} & (\rho u^* A)_e - (\rho u^* A)_w + (\rho v^* A)_n - (\rho v^* A)_s \\ & + (\rho A)_e \frac{1}{(A_P)_e} (p'_P - p'_E) - (\rho A)_w \frac{1}{(A_P)_w} (p'_W - p'_P) \\ & + (\rho A)_n \frac{1}{(A_P)_n} (p'_P - p'_N) - (\rho A)_s \frac{1}{(A_P)_s} (p'_S - p'_P) = 0 \end{aligned} \quad (3.15)$$

Equation (3.15) is solved for the pressure correction. This correction is then used in Eqs. (3.13) to compute the velocity correction. Having the pressure as well as velocity correction values, updated pressure and velocities are obtained by solving Eqs. (3.10) and (3.11). Because of the mathematical nature of the procedures described above, iterative solution procedure is required until the calculation has achieved the convergence. Furthermore, to solve the system of the implicit equations simultaneously, the Line Gauss-Siedel method is used as a solver.

### 3.2.3 The QUICK Scheme

After the dependent variables have been computed by the procedure described in the previous section, it is necessary to compute the fluxes at the control surfaces to use them back in the (discretized) governing equations. In other words, the dependent variables must be calculated at the control surfaces since the terms in the governing equations (Eq. (3.6) or (3.8)) are evaluated at the cell surface. This can be made by using a suitable interpolation function. In this study, the QUICK scheme [30] is used among the higher order interpolation schemes. In the QUICK scheme, the east face value  $\phi_e$  in Fig. 3.1, for example, is computed as

$$\begin{aligned}\phi_e = & \lambda \left( \frac{\Delta x_{i+1}}{\Delta x_i + \Delta x_{i+1}} \phi_P + \frac{\Delta x_i}{\Delta x_i + \Delta x_{i+1}} \phi_E \right) \\ & + (1 - \lambda) \left( \frac{\Delta x_{i-1} + 2\Delta x_P}{\Delta x_{i-1} + \Delta x_i} \phi_P - \frac{\Delta x_i}{\Delta x_{i-1} + \Delta x_i} \phi_W \right)\end{aligned}\quad (3.16)$$

where  $\lambda=3/4$  and  $\Delta x_i$  is the distance between the east face and the west face.

It is known that the higher interpolation schemes can lead numerical instabilities, especially near discontinuity, while they provide higher accuracy. Thus a limiter is introduced to prevent this numerical difficulties by tuning  $\lambda$  in Eq. (3.16) such that

$$\begin{aligned}\lambda &= \frac{2 - 3\tilde{\phi}_P}{1 - 2\tilde{\phi}_P} & \text{if} & \quad \frac{5}{6} < \tilde{\phi}_P < 1 \\ \lambda &= \frac{-3\tilde{\phi}_P}{1 - 2\tilde{\phi}_P} & \text{if} & \quad -\frac{1}{2} < \tilde{\phi}_P < 0 \\ \lambda &= \frac{3}{4} & \text{otherwise}\end{aligned}\quad (3.17)$$

where

$$\tilde{\phi}_P \equiv \frac{\phi_P - \phi_W}{\phi_E - \phi_P}$$

### 3.2.4 Grid System

Several grid systems have been tested to compare the results and performance. First of all, the body-fitted rectangular grid with blockage technique was employed as shown in Figs. 3.2. This grid topology was initially used due to the historical background that Fluent, more generally the SIMPLE algorithm, was developed based on the Cartesian or cylindrical coordinate system. One hundred and forty eight (148) grid points are assigned in the x-direction while 99 points are assigned symmetrically in the y-direction. Care has been taken to keep grid sizes agreed in the x- and y-direction at  $\pm 45^\circ$  and  $\pm 135^\circ$  to eliminate unwanted grid size discontinuity. The physical domain is defined  $2.5d$  before and  $12.5d$  behind the cylinder. In the y-direction, the domain stretches to  $\pm 4.5d$ .

Second and third grid systems used are shown in Figs. 3.3 and Figs. 3.4, respectively. These grid systems are called O-grid and has a branch cut at a line from the

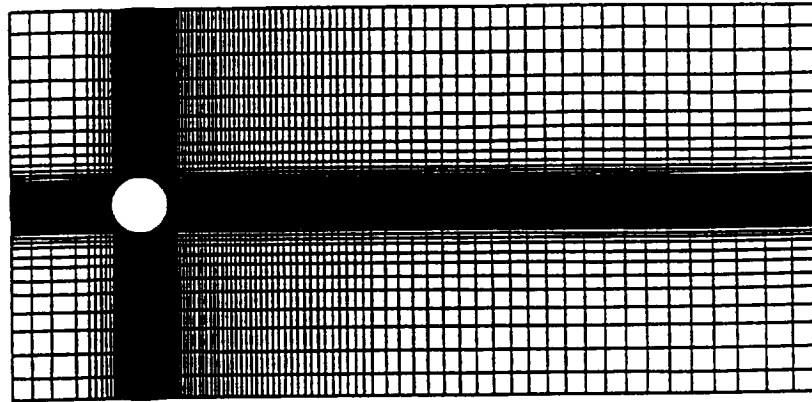


Fig. 3.2a Body fitted rectangular grid system around a circular cylinder.

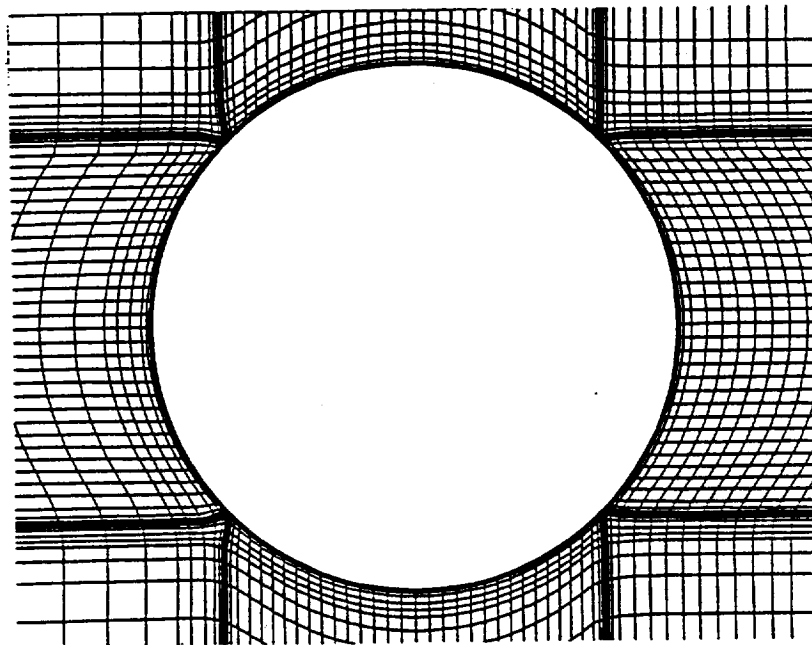


Fig. 3.2b Body fitted rectangular grid system around a circular cylinder (in the vicinity of the wall).



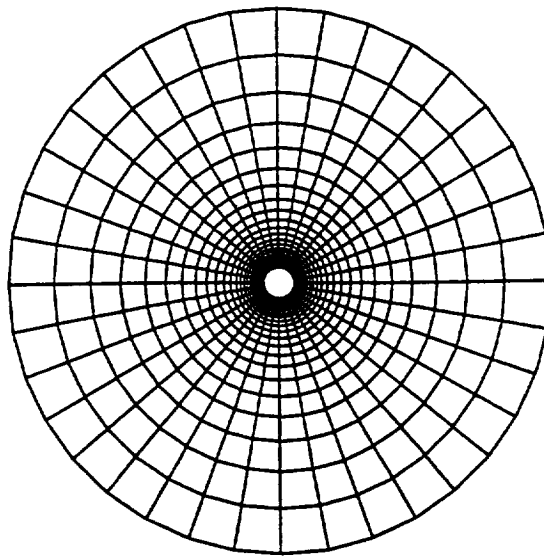


Fig. 3.3a O-type grid system around a circular cylinder.

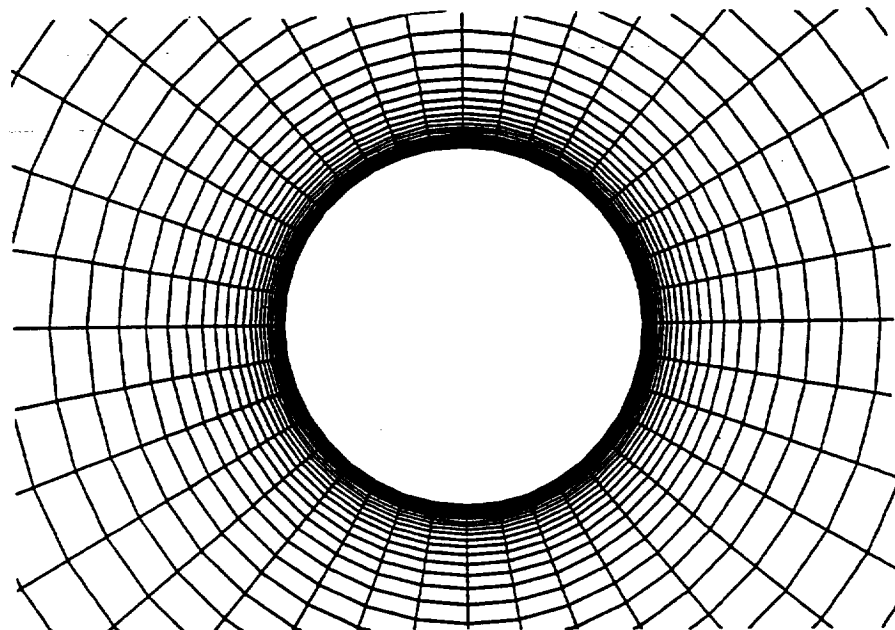


Fig. 3.3b O-type grid system around a circular cylinder  
(in the vicinity of the wall).

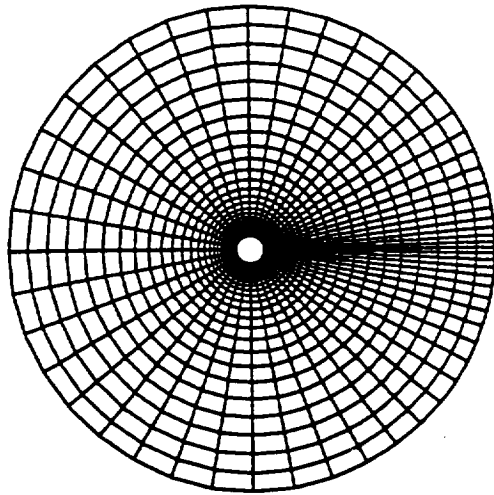


Fig. 3.4a Improved O-type grid system around a circular cylinder.

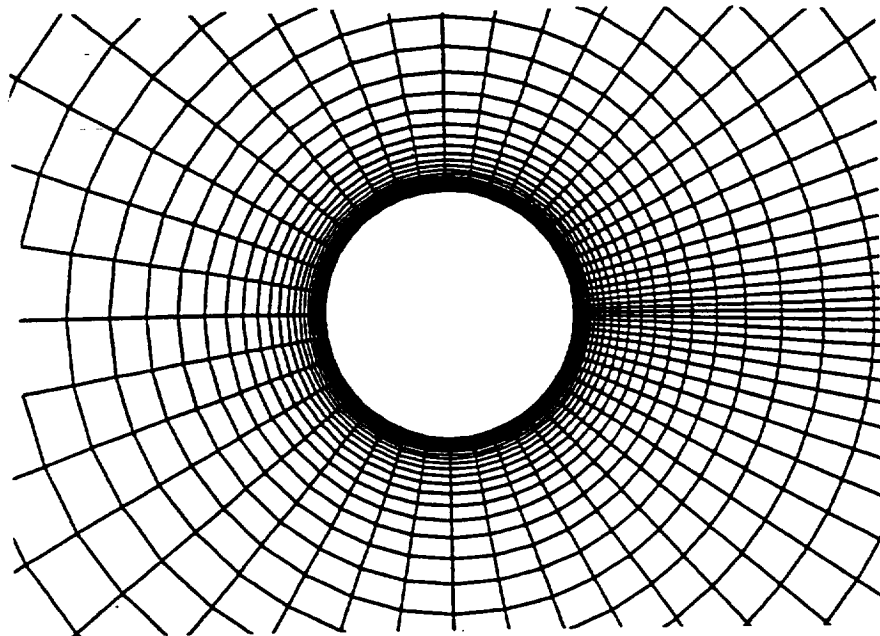


Fig. 3.4b Improved O-type grid system around a circular cylinder (in the vicinity of the wall).

front stagnation point stretching in the negative x-direction to the outer boundary. A branch cut is needed to make a physical domain simply connected. Although it is common to place a branch cut in the downstream of a body, the branch cut is located in the upstream in the present study. This is because: (1) the rear stagnation point is very important by means of having jet injection, (2) it is good practice to place a numerically difficult case, such as a branch cut, in a fluid dynamically simple region, (3) Fluent has a bug in graphical representation for a cyclic boundary (which corresponds to a branch cut). The outer boundary is located at  $8.5d$  unless mentioned away from the surface of the cylinder. For the grid system shown in Figs. 3.3, 37 grid points are evenly distributed along the circumferential direction while 51 grid points are systematically stretched in the radial direction. For the grid system shown in Figs. 3.4, there are 55 grid points in the circumferential direction keeping the same 51 grid points in the radial direction as the preceding one. From the front stagnation point to  $\theta = \pm 90^\circ$ , 20 grid points are assigned uniformly. After  $\theta = \pm 90^\circ$ , grid points are packed towards the rear stagnation point to have a good resolution for the shear flow due to the jet. The grid is sized to be  $1.368^\circ$  at the rear stagnation point. As stated in the later chapter, the third grid system has been selected as an optimized grid system with regard to balancing the resolution, the aspect ratio of the cells, computer memory storage and computational time.

To reproduce the boundary layer on the surface correctly, grid points should be clustered towards the wall. In general, about ten grid points at least are required inside the boundary layer. The boundary layer thickness over a circular cylinder based on the Blasius series can be found in Fig. 9.5. of Ref. 5. The steady-state forward stagnation point boundary-layer edge,  $y_{edge}$ , (99% of uniform velocity) is found at

$$\frac{y_{edge}}{R} \sqrt{\frac{U_\infty R}{\nu}} \approx 2.0 \quad (3.18)$$

where  $R$  is the radius of the cylinder and  $\nu$  is the kinematic viscosity. The left hand side of Eq. (3.18) is the normalized boundary layer thickness. The value in the right hand side of Eq. (3.18) is set equal to 0.1 for the first grid point,  $y_1$ , away from the wall, that is,

$$\frac{y_1}{R} \sqrt{\frac{U_\infty R}{\nu}} = 0.1 \quad (3.19)$$

Based on the above formula,  $y_1$  is set to 0.00022 of the cylinder diameter. This corresponds to about 5% of the steady-state forward stagnation point boundary-layer thickness. The value of 0.1 in the right hand side of Eq. (3.19) is maintained for different Reynold number cases during the investigation of the Reynolds number effect described in Chap. V to obtain a equal comparison. The grid size is increased at the outer boundary to  $0.7d$  for the first grid system and  $0.68d$  for the second and third grid systems.

### 3.2.5 Boundary Conditions

The boundary conditions used are shown in Figs. 3.5 and 3.6. No-slip condition is imposed on the cylinder for all the grid system. Velocities are fixed to  $u = u_\infty$  and  $v = 0$  except for the downstream outer boundary for the first grid system as illustrated in Fig. 3.5. Neuman conditions are employed at the downstream outer boundary where the gradient of the dependent variables in the normal direction is fixed to zero. For the second and the third grid systems, fixed velocity condition is used up to  $\pm 90^\circ$  and fixed pressure condition with fixed flow angle is imposed for the rest of the outer boundary as shown in Fig. 3.6. The flow angle is fixed to be parallel to the x-axis. The  $u$  velocity between  $90^\circ < \theta < 270^\circ$  is determined so that the continuity equation is satisfied. When the jet blowing cases are performed, fixed velocities are given at the jet slot.

### 3.2.6 Time Step

Computational time step should carefully be chosen so that the physical phenomena can be reproduced correctly. The larger time step gives faster computational progress; however, the time step is restricted by the CFL condition [10]. The CFL condition is written as

$$\frac{u \Delta t}{\Delta x} \leq 1.0 \quad (3.18)$$

Since implicit scheme is unconditionally stable, the time step can theoretically be taken as any number in such a scheme. However, care must be taken if time-accurate computation is performed. Because of the lack of availability for checking the CFL

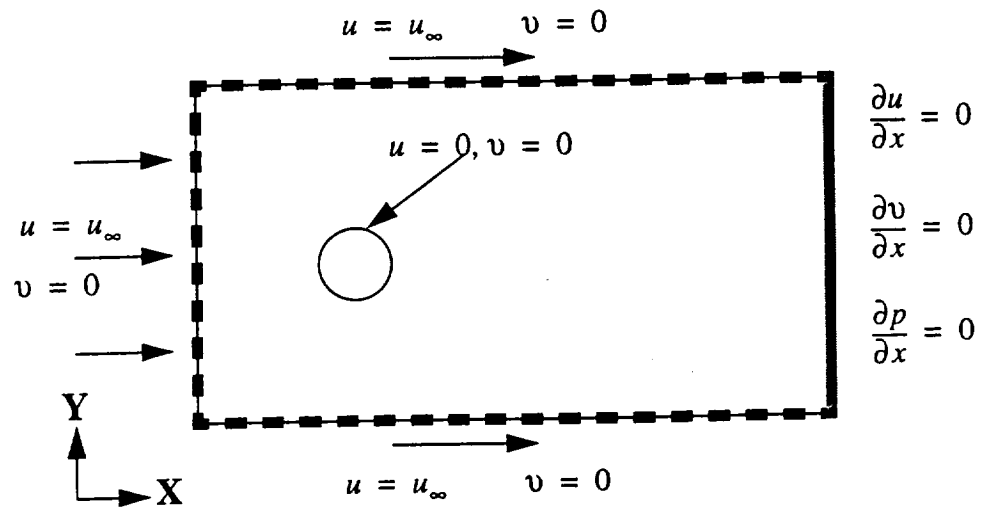


Fig. 3.5 Boundary conditions for the body fitted rectangular grid system.

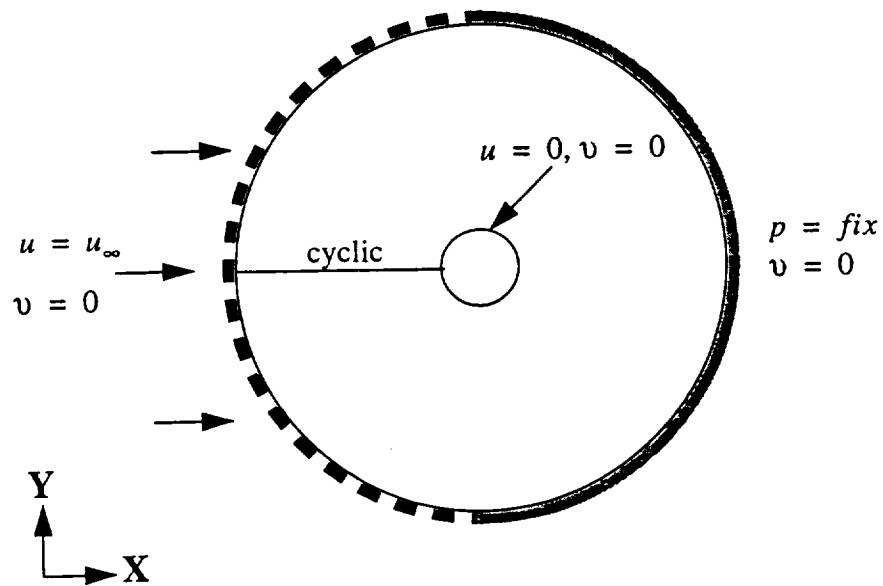


Fig. 3.6 Boundary conditions for the O-type grid systems.

condition in Fluent, several time steps have been tested to see the effect of the time step on the calculation. For the rectangular grid system,  $t=0.0078$  was used, while  $t=0.005$  was used for the O-grid systems.

### 3.2.7 Residual

To obtain how much the calculation is close to the convergence, the residual is monitored and used to judge if the convergence is achieved. In Fluent, the residual is computed, based on Eq. (3.7), as

$$Res_{u,v} = \sum_{nodesP} \left| [\dot{M}^{old} \phi_p^{old} + a_e \phi_e + a_w \phi_w + a_n \phi_n + a_s \phi_s + S_\phi - a_p \phi_p] \right| \quad (3.19)$$

where  $nodesP$  represents all the nodal points in computational domain. This residual is normalized by using the left hand side of Eq. (3.7) such that

$$\overline{Res}_{u,v} = \frac{\sum_{nodesP} \left| \dot{M}^{old} \phi_p^{old} + a_e \phi_e + a_w \phi_w + a_n \phi_n + a_s \phi_s + S_\phi - a_p \phi_p \right|}{\sum_{nodesP} |a_p \phi_p|} \quad (3.20)$$

Eq. (3.20) is applied  $u$  and  $v$  velocities. The residual for pressure is computed from the imbalance in the continuity equation (Eq. (3.14)) such that

$$Res_p = \sum_{nodesP} |(\rho u A)_e - (\rho u A)_w + (\rho v A)_n - (\rho v A)_s| \quad (3.21)$$

Normalization of the residual for pressure is defined in the code as

$$\overline{Res}_p = \frac{Res_p}{Res_p^{iter2}} \quad (3.22)$$

where  $Res_p^{iter2}$  is the pressure residual at the second iteration. In the present study, the criterion of the residual to judge the achievement of the convergence was

$$\overline{Res}_u + \overline{Res}_v + \overline{Res}_p \leq 1 \times 10^{-3} \quad (3.23)$$

For the unsteady calculations, Eq. (3.23) was used to judge the convergence at each time level. After the Eq. (3.23) is satisfied, the calculation was marched to the next time step. For the steady calculation, Eqs. (3.19), (3.20) and (3.22) were used to determine if a solution is periodical after the transitional oscillation.

## Chapter IV

### EXPERIMENTAL ARRANGEMENT

In this chapter, experimental setups and methods used in this study are described.

#### 4.1 Test Facility

The wind tunnel tests were conducted in the 3 by 4 foot low speed wind tunnel at Old Dominion University. This wind tunnel is a close circuit, closed test section, fan driven wind tunnel [31]. The fan is driven by the 125 H.P. induction motor with a solid-state variable frequency controller. Figure 4.1 shows the schematic of the wind tunnel. The usable velocity range is from 12 m/s to 60 m/s. To obtain the appropriate Reynolds number, the velocity was varied from 13m/s to 40m/s. The turbulence intensity level is about 0.2% throughout the velocity range. The test section velocity is obtained by the contraction pressure drop. This pressure difference was preliminary calibrated by a pitot-static tube mounted in the test section.

#### 4.2 Test Models

Two circular cylinders were used. A model "A" is a 3"-diameter and 4'-long circular cylinder without jet slot and is made of steel. The aspect ratio of the model is 16.0. This model has 18 pressure holes along the circumferential direction at the center in the spanwise direction, starting from the front stagnation point with 20° increment. The smaller increment (5°) of the pressure data point were collected by rotating the cylinder. The model "A" was mounted horizontally. This model is shown in Fig. 4.2.

A model "B" is a 4.5"-diameter and 3'-long circular cylinder with jet slot and is made of PVC. The aspect ratio of the model is 8.0. A 1/16"-width and 12"-long jet slot was made along the rear stagnation line. The jet was supplied by compressed air through a pressure regulator. Jet velocity was measured by a small pitot tube placed directly behind the jet slot. After the pressure regulator was carefully calibrated by means of the pitot tube, the jet velocity was obtained by the pressure regulator reading. The jet velocity was



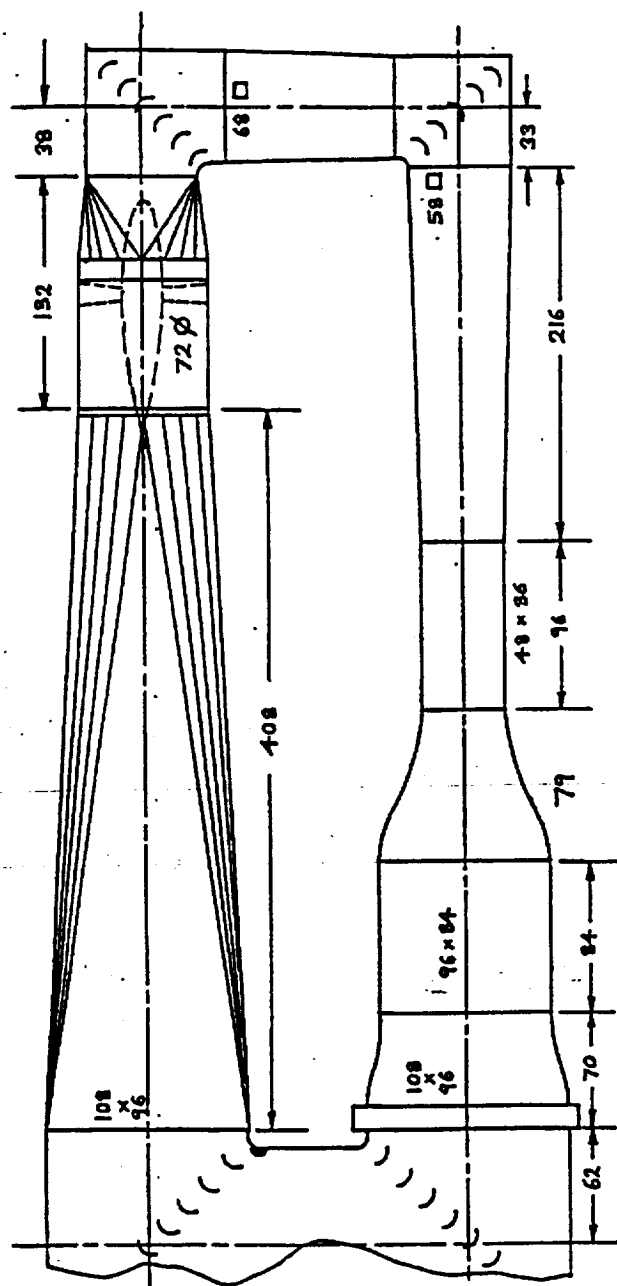


Fig. 4.1 Schematic of Old Dominion University three by four foot low speed wind tunnel.  
(dimensions in inches and not to scale)

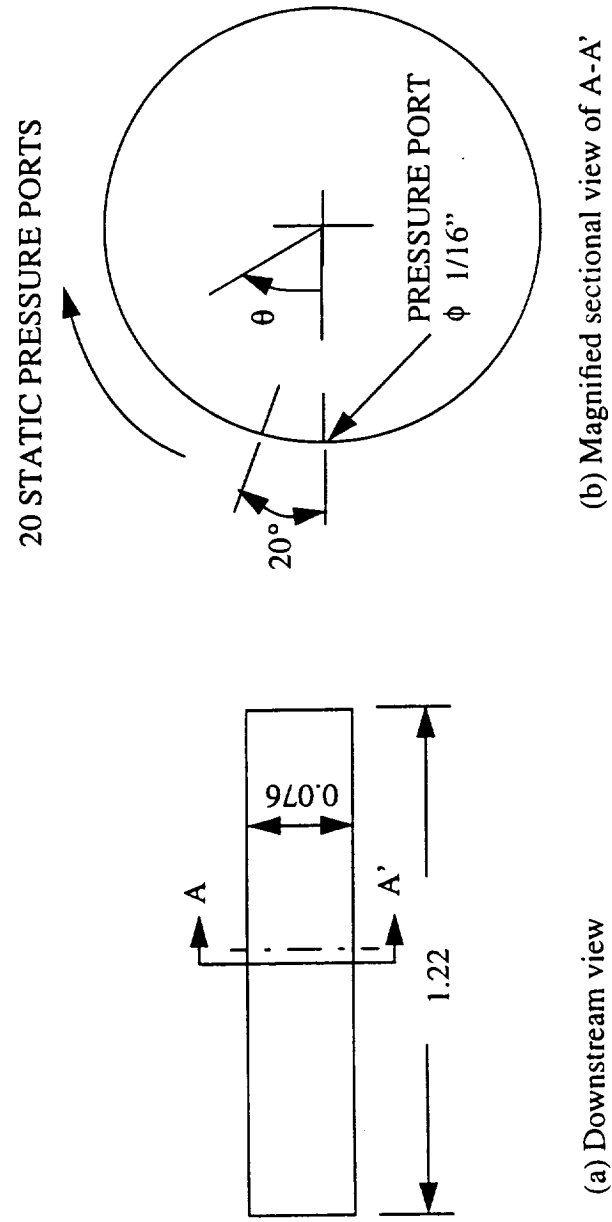


Fig. 4.2 Wind tunnel test model "A"

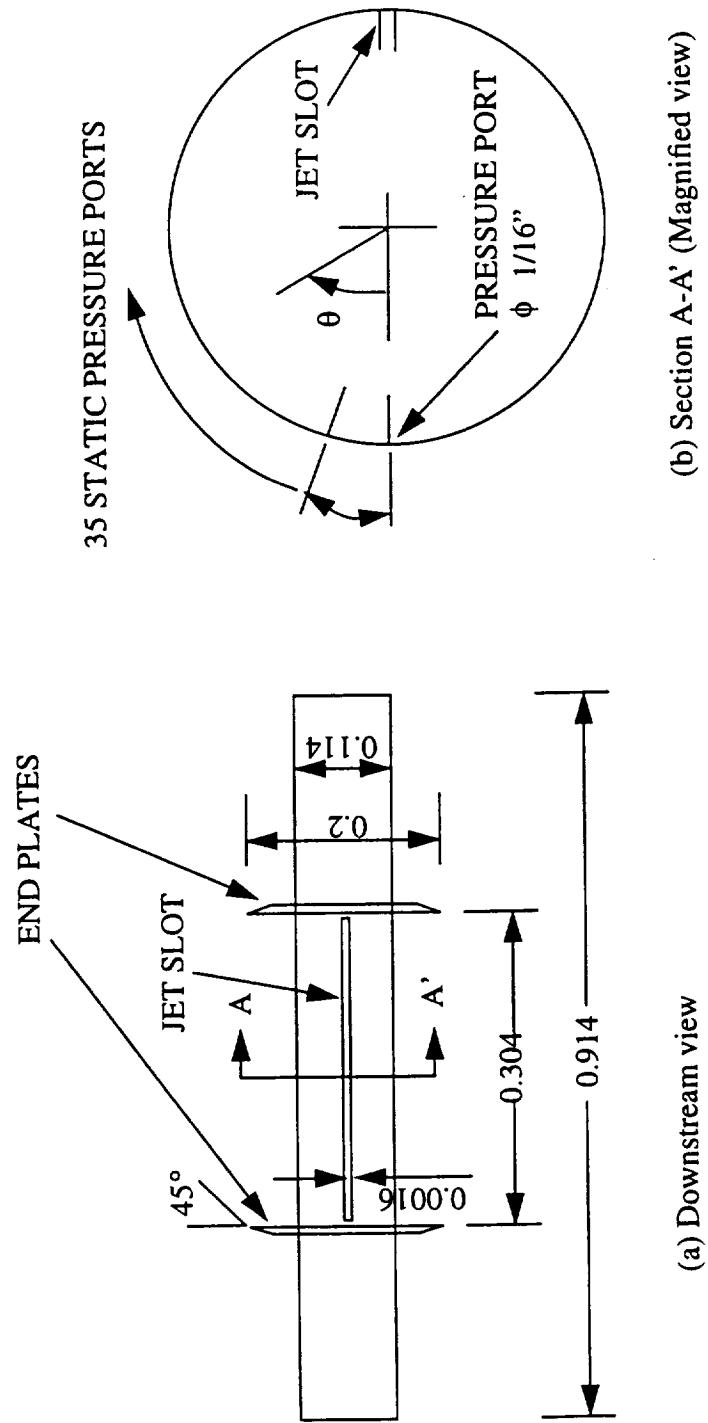


Fig. 4.3 Wind tunnel test model "B".

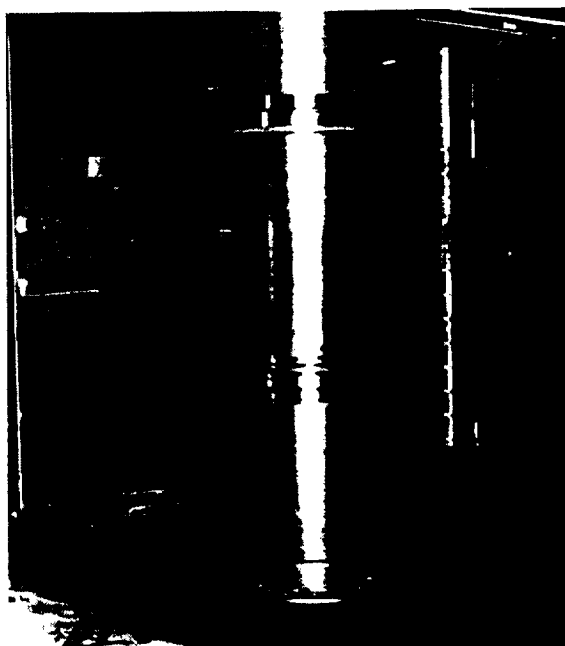


Fig. 4.4 Photograph of the model "B" in the Old Dominion University low-speed wind tunnel (flow from left to right).

varied from 11m/s to 28m/s. The corresponding volume flow rates were from  $0.005323m^3/s$  to  $0.01355m^3/s$ . Moreover, these correspond  $0.0175m^3/s$  and  $0.0300m^3/s$  per unit length of the slot, respectively. Two end plates whose outer diameters are 8" were placed at the ends of the slot to make the jet blow two-dimensionally. This end plate diameter was selected so that it is large enough to make the jet blow two-dimensionally while it is small enough not to produce very thick boundary layer on the plates which may disturb two-dimensionality of the cylinder. This model has 35 pressure holes with  $10^\circ$  increment along the circumferential direction except for the rear stagnation. The model "B" was mounted vertically. This model is illustrated in Fig. 4.3. Figure 4.4 depicts the set up of this model in the tunnel.

The pressure ports were used to estimate the sectional drag as well as to obtain the pressure distribution. The both models were painted in black for flow visualization purpose. To reduce adverse effects due to model surface roughness as much as possible, the models were polished before and after painting by the #600 silicon carbide water-proof sand paper. Much effort was paid to make the model surface as smooth as possible; however, the surface roughness for the models is not available at this time.

### 4.3 Static Pressure Measurement

The static pressure tubes from the model were connected to a Pressure Systems Incorporated (PSI) 9010 module to transfer pressure data to voltage values. The PSI 9010 module was set to take 32 sequential samples and obtain average for the each port before moving to the next port. This process takes approximately 3.2 sec. After completing one set of scans for all the 35 pressure ports, the PSI 9010 module was programmed to repeat this sampling procedure 30 times. Incidentally, the estimated characteristic time ( $d/u_\infty$ ) is about  $8.8 \times 10^{-3}$  sec. Moreover, the calculated vortex shedding interval is about 0.044 sec., assuming the Strouhal number of 0.2. Therefore, it is noted that the pressure data sampling time is very large in comparison to the known flow events. The reproducibility of the data was very good.

The static accuracy of the PSI module is  $0.015 \text{ in } H_2O$  [32]. Applying the Kline / McClintock equation, the uncertainty of the pressure coefficient,  $\delta C_p$ , is expressed as

$$\delta C_p = \sqrt{\left(\frac{\partial C_p}{\partial p}\right)^2 [\delta(p - p_\infty)]^2 + \left(\frac{\partial C_p}{\partial q}\right)^2 (\delta q)^2} \quad (4.1)$$

where

$$\frac{\partial C_p}{\partial p} = \frac{1}{q}, \quad \frac{\partial C_p}{\partial q} = \frac{-1}{q^2}(p - p_\infty)$$

$$\delta q = 2\sigma_q$$

and  $\delta(p - p_\infty)$  is the static accuracy of the PSI module. In Eq. (4.1),  $\sigma_q$  is the standard deviation of the dynamic pressure and was calculated every time pressure data was taken. Throughout the test,  $\sigma_q$  was less than 1.2% and  $\delta C_p$  was about 1%.

#### 4.4 Smoke Wire Visualization

For smoke wire visualization, the 4.5"-diameter cylinder, the model "A", was used. A 0.015"-diameter stainless steel wire was placed at 5" upstream of the cylinder center. The wire was, therefore, located at 2.75" upstream from the surface of the cylinder. The wire was tensioned horizontally to see a cross flow around the cylinder. A delay and duration of the currency to generate the smoke were adjusted manually so that the smoke passes the cylinder in a proper timing. Commercial "baby oil" was used as smoke oil after several oils and their mixture were tested. A camera was placed at 10" downstream from the rear stagnation point aiming downward. The camera set up is illustrated in Fig. 4.5.

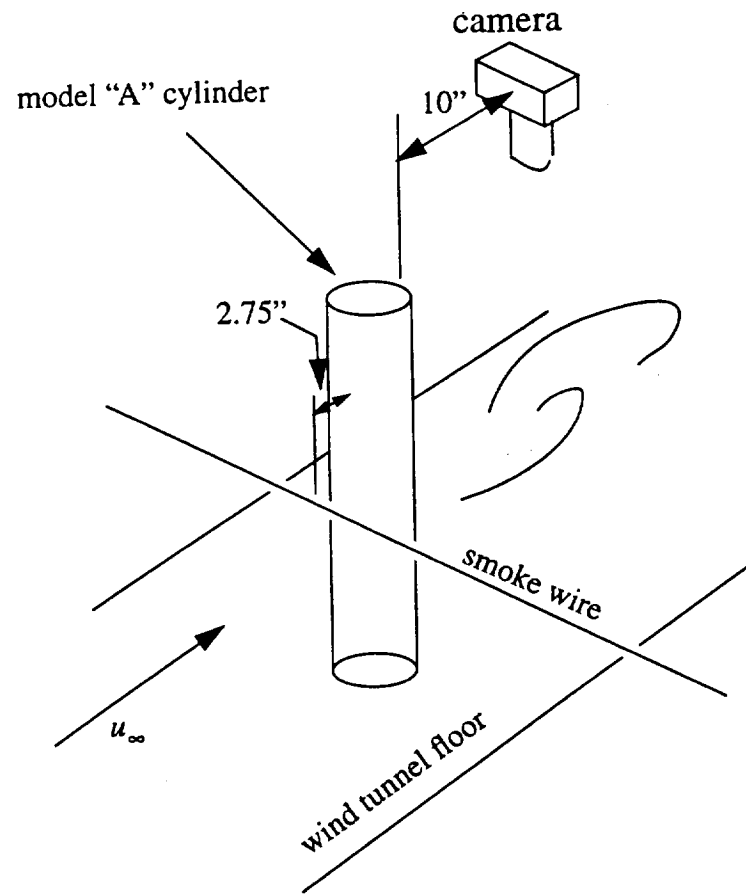


Fig. 4.5 Camera set up for smoke wire flow visualization.

## Chapter V

### COMPUTER CODE INVESTIGATION

In this chapter, the validity of the commercial computational fluid dynamics code (Fluent) is investigated for the present study. A cross flow over a two-dimensional circular cylinder at Reynolds number  $1 \times 10^5$  was used as a “bench mark” test unless otherwise mentioned. The results are compared with the data from the literature to determine the validity. First, the three grid systems described in Sec. 3.2.4 are compared with regard to accuracy as well as suitability for the present problem. After the grid system has been selected, computational results are examined for various conditions. To confirm the validity of the grid chosen, the flow at different Reynolds numbers were calculated. Since it is always desirable to reduce computational time as well as memory storage, validity of the steady state assumption and grid dependency are also investigated.

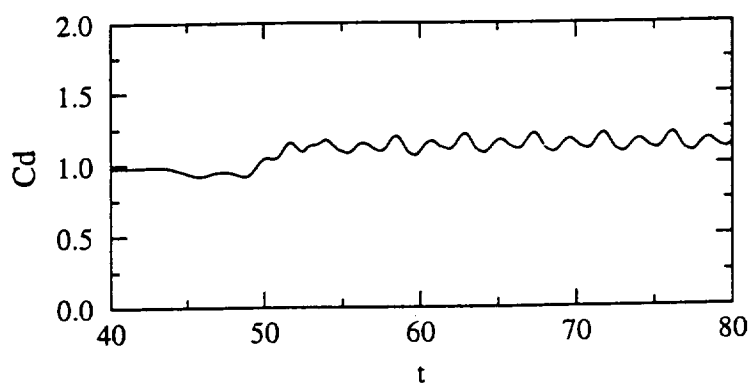
#### 5.1 Grid Topology Study

Due to the historical background with the code explained in Sec. 3.2.4, a rectangular body fitted grid as illustrated in Fig. 3.2 was initially used. Figures 5.1 and 5.2 show the comparison among the grid systems in the time histories of the drag and lift coefficients, respectively. The horizontal axis represents the dimensionless time normalized by the uniform velocity and the cylinder diameter, that is,

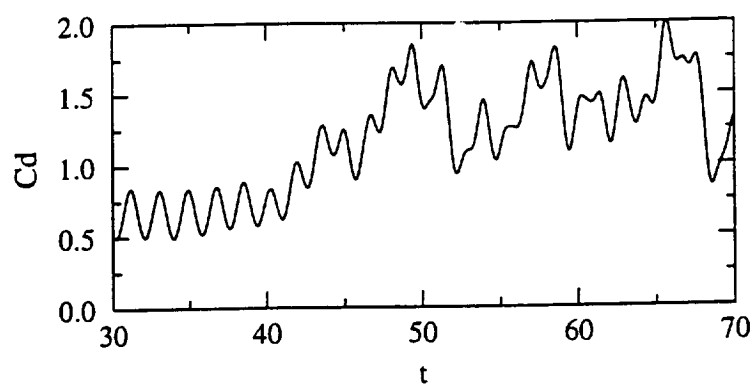
$$t = \frac{u_{\infty} t^*}{d} \quad (5.1)$$

where  $t^*$  is time with dimension. The time period shown starts right before the flow is considered to reach the periodic mode based on the lift coefficient fluctuation. Because of the objective of this study, namely to investigate the feasibility of drag reduction, special attention has been paid on the drag coefficient and on the pressure values for validating the code. Because of the essential difference between the rectangular grid and the O-grid, the

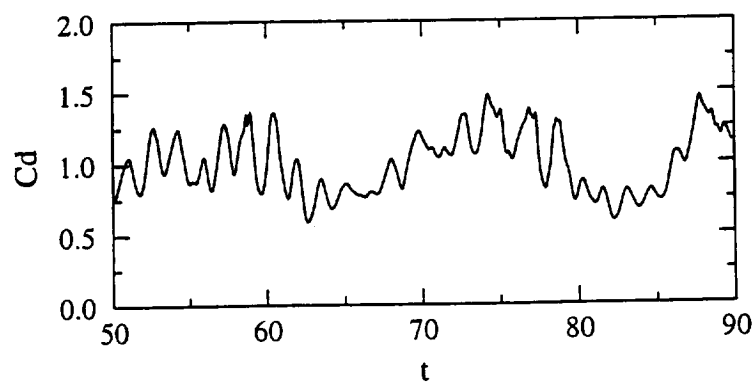




(a) Rectangular body fitted grid

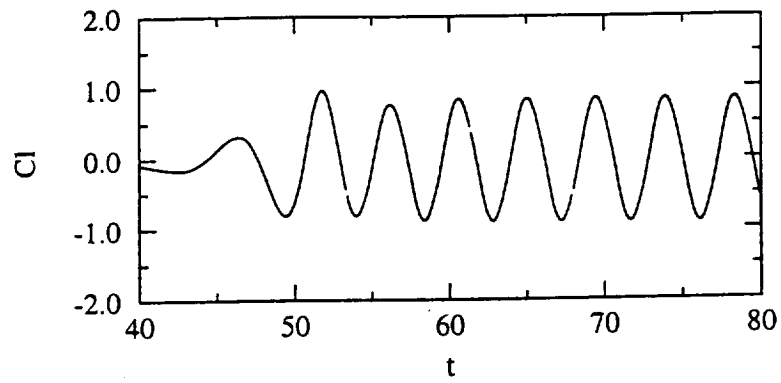


(b) O-grid.

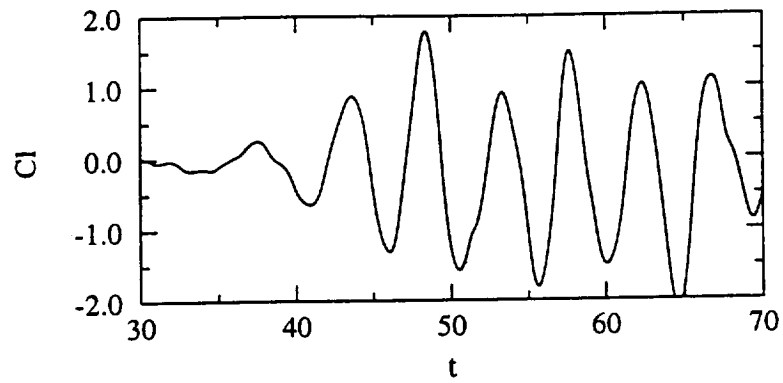


(c) Improved O-grid

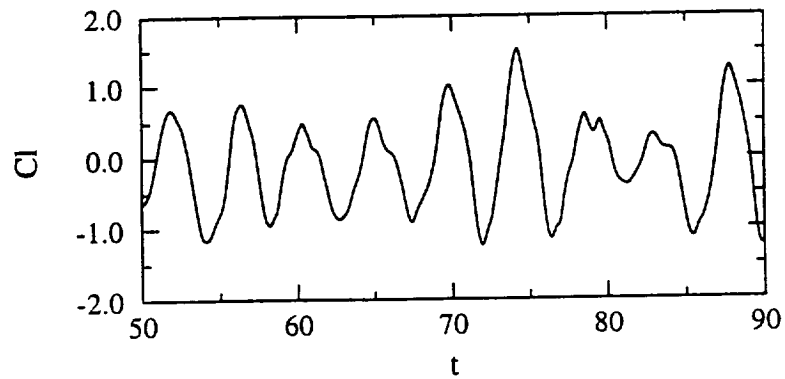
Fig. 5.1 Time history of the drag coefficient for different grid systems.



(a) Rectangular body fitted grid



(b) O-grid.



(c) Improved O-grid

Fig. 5.2 Time history of the lift coefficient for different grid systems.

characteristic of the drag coefficient fluctuation is different while the lift coefficient fluctuation is seen to be similar. However, the magnitude of the lift coefficient is dependent on the type of grid used. The fluctuation of the lift for the rectangular grid has more systematic periodicity than the O-grids. The starting time when the periodic characteristic appears from the impulsive start also depends on the grid.

The time averaged drag coefficients and the estimated Strouhal numbers for each grid are listed in Table 5.1. It is a common practice to compute the Strouhal number from the lift coefficient fluctuation for numerical experiment [8, 17]. Thus the Strouhal numbers are estimated based on the time of one cycle of the lift fluctuation. Incidentally, the horizontal axis in Figs. 5.1 and 5.2 or  $t$  in Eq. (5.1) corresponds to the reciprocal of the Strouhal number. For computing the time-averaged drag coefficient, the drag coefficient is averaged over five cycles of the fluctuation. Also shown in Table 5.1 are the drag coefficient and the Strouhal number at Reynolds number  $1 \times 10^5$  from other studies. The value 1.2 for the drag coefficient measured by Wieselsberger [33] is widely accepted and commonly used as a "bench mark" value. Furthermore, the drag coefficients from many different experimental measurements are reported in the range of 1.1–1.4 [4]. The Strouhal number in this Reynolds number depends less on both Reynolds number and experimental conditions. The Strouhal number has a value of around 0.2 [4]. All the grid systems tested have provided a good agreement with the commonly accepted value with 15% of error for the drag and 10% for the Strouhal number.

The time-averaged pressure distribution along the cylinder surface is shown in Fig. 5.3. The pressure distribution based on the potential theory is also plotted in the figure. The horizontal axis is the angle  $\theta$  from the forward stagnation point along the surface. Despite the fact that there is no significant difference in the drag coefficient and the Strouhal number among the grid systems, there are differences in the pressure distribution. First of all, the minimum pressure value of the rectangular grid is much smaller than that of the O-grids. The pressure profile of the rectangular grid has a similar characteristic to the theoretical one up to  $\pm 130^\circ$ . The pressure in the leeward of the cylinder has also different values depending upon the grid system and these are quite different from the theory due to the separation. The locations of the minimum pressure point are almost the same, which are approximately  $\theta = \pm 80^\circ$ . Applying the Bernoulli's equation, the

Table 5.1 Comparison of the time-averaged drag coefficient and Strouhal number for different grid systems ( $Re = 1 \times 10^5$ )

	Rectangular Grid	O-Grid	Improved O-Grid	Numerical, C-Grid	Experiment
$C_D$	1.14	1.42	1.00	1.16 [9]	1.2 [33]
$St$	0.22	0.21	0.22	0.22 [9]	0.2 [4]

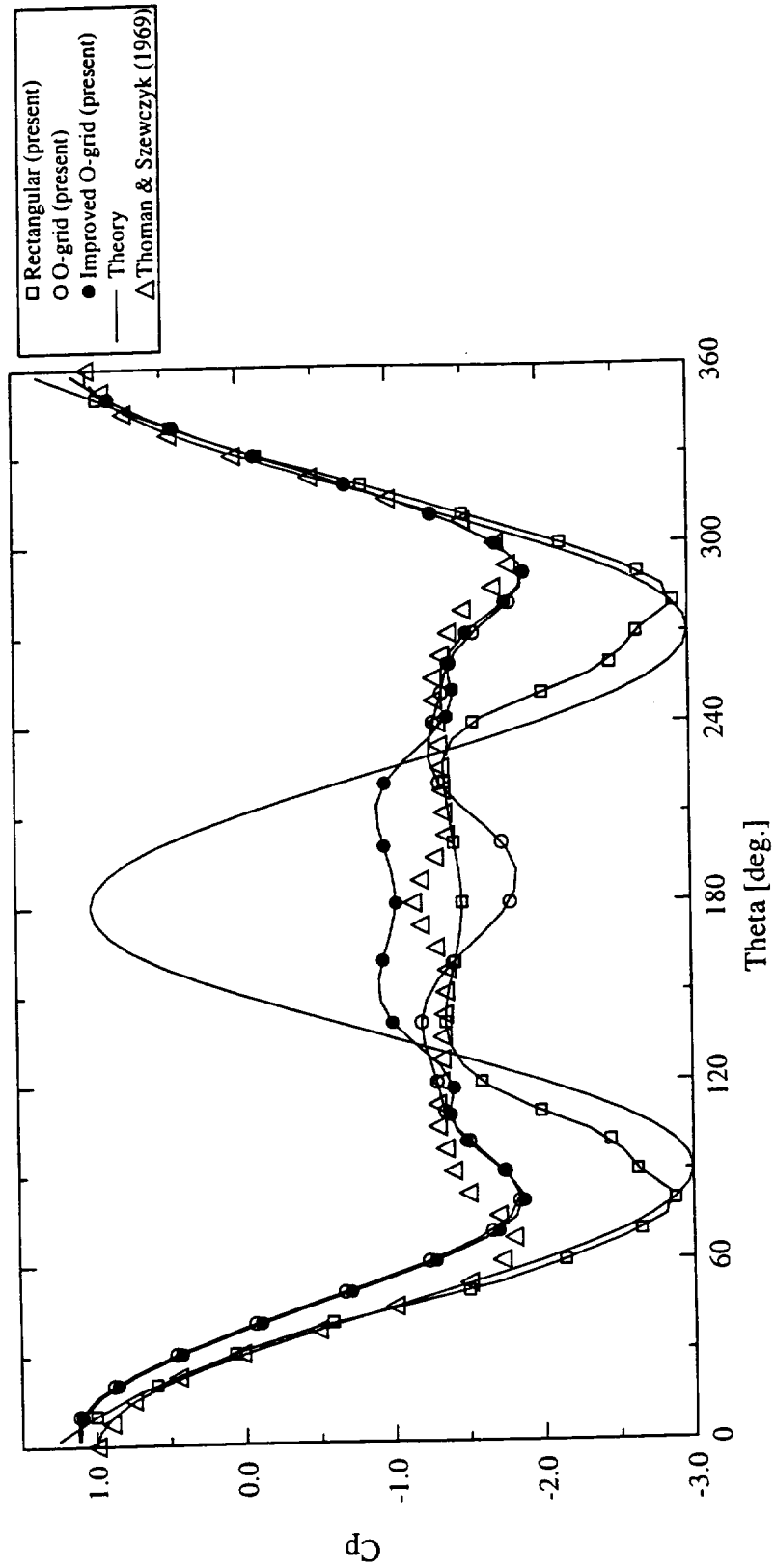


Fig. 5.3 Comparison of pressure distributions along a circular cylinder at  $Re = 1 \times 10^5$  for different grid systems.

pressure coefficient at the front stagnation must have a value of 1.0 ideally. All grids reproduce this nature very well.

In general, the pressure decreases until about  $80^\circ$  due to velocity acceleration. After passing the minimum pressure point, the flow experiences adverse pressure gradient and is separated. Because of the separation, the pressure is not resumed to 1.0 at the rear stagnation point as stated by the theory. The numerical results also reproduce this characteristic. Consulting the results from other investigations [1, 2, 8, 9], the pressure distribution of the O-grids are considered as better result than that of the rectangular grid. The results obtained by Thoman and Szewczyk [8] are also plotted in Fig. 5.3 as an example. Up to  $\pm 120^\circ$ , the pressures for the O-grid cases are in excellent agreement with their results. From  $\theta \approx 150^\circ$  to  $\theta \approx 210^\circ$ , there can be seen a difference between the O-grid and their results; however, the improved O-grid case shows a good agreement at the rear stagnation point ( $\theta = 180^\circ$ ) with the results by Thoman and Szewczyk.

There is no significant difference in the drag and the Strouhal number among the grid systems tested. However, the rectangular grid system shows unrealistic pressure distributions. On the other hand, O-grid systems show good agreement with a widely accepted values for the drag coefficient, the Strouhal number and the pressure distribution profile. It should be also noted that the rectangular grid has  $149 \times 99$  grid points while the O-grid and improved O-grid have only  $37 \times 51$  and  $55 \times 51$  grid points, respectively to generate the same grid concentration near the wall. The number of grid cannot be simply compared because the area of the physical domain is different and the grid stretch function is not identical. However, the rectangular grid system requires more unnecessary grid points far away from the cylinder to reduce the grid aspect ratio. For all grid systems, the grid aspect ratio is carefully adjusted especially behind the cylinder where the direction of flow is not expected to be parallel to the cell faces. This problem makes the rectangular grid system very inefficient and expensive to apply to the present study. Finally, but most importantly, the grid lines do not intersect with the cylinder surface orthogonally. This generates another term in the discretized governing equation due to the geometrical transformation and the term reduces computational accuracy [34]. On the other hand, the O-grid systems are very efficient in terms of usage of limited number of grid points, that is, large number of grid points can be packed only in the vicinity of the wall where small

cell size is needed for a steep gradient of the variables. The improved O-grid system is made based on the second grid system by increasing grid point behind the cylinder where highly two-dimensional flow is expected. Moreover, the grid points behind the cylinder are packed towards the rear stagnation point at which jet will be injected therefore steep gradient is expected due to jet shear. Based on these reasonings, the improved O-grid system shown in Figs. 3.4 has been selected for the present study.

## 5.2 Reynolds Number Effect

To confirm the validity of the grid system chosen in the previous section as well as the computer code itself, computations were performed at a different Reynolds number. The Reynolds number of  $1 \times 10^3$  was chosen to accomplish this purpose. At this Reynolds number, the flow is also expected to be laminar up to the separation point. The drag coefficient and the Strouhal number are approximately 1.0 [33] and 0.21 [35], respectively.

The time history of the drag and the lift coefficients are illustrated in Figs. 5.4 and 5.5, respectively. These results have a similar pattern (in terms of the behavior in time) as demonstrated by Rogers and Kwak [6] at the  $Re = 2 \times 10^2$ . It is noted that the drag coefficient fluctuations are more systematically oscillating than the  $Re = 1 \times 10^5$  case. This is not only due to the stability of the numerical method but also because of the physical nature. As the Reynolds number is decreased, the diffusion term in the governing equations becomes more effective. And the diffusion term “stabilize” the computation. The same discussion can be made for real flow: as Reynolds number is decreased, flow, in general, becomes less perturbed by high frequency fluctuations.

The time-averaged drag coefficient and the Strouhal number estimated following the same manner as for the  $Re = 1 \times 10^5$  case are listed in Table 5.2. The calculated drag coefficient is slightly higher than the Wieselsberger’s experimental value, while the Strouhal number has a good agreement with the experimental data [4]. The time-averaged pressure distributions are illustrated in Fig. 5.6. The distributions at  $Re = 1 \times 10^5$  are also shown again here for comparison. The pressure distributions for the  $Re = 1 \times 10^3$  case are similar to the  $Re = 1 \times 10^5$  case up to the minimum pressure points. The lower Reynolds number case has lower pressure values around the base portion of the cylinder. This results in a higher drag coefficient than the higher Reynolds number case.

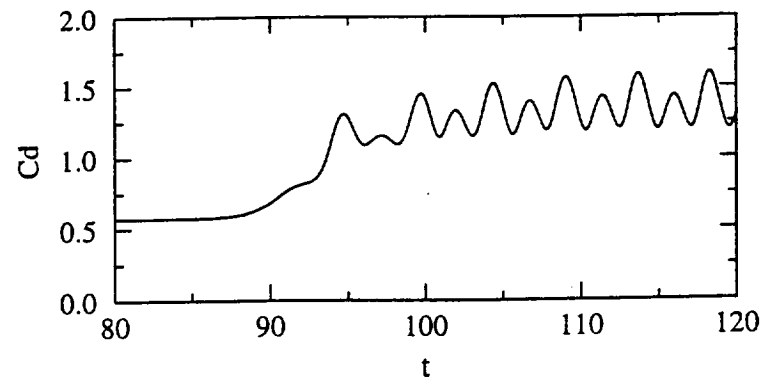


Fig. 5.4 Time history of the drag coefficient at  $Re = 1 \times 10^3$ .

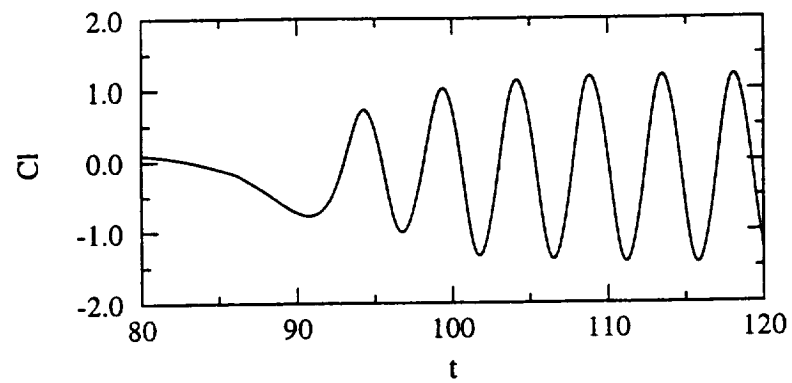


Fig. 5.5 Time history of the lift coefficient at  $Re = 1 \times 10^3$ .



Table 5.2 The time-averaged drag coefficient and Strouhal number at  $Re = 1 \times 10^3$

	Present study	Experiment
$C_D$	1.36	1.0 [32]
$St$	0.22	0.2 [34]

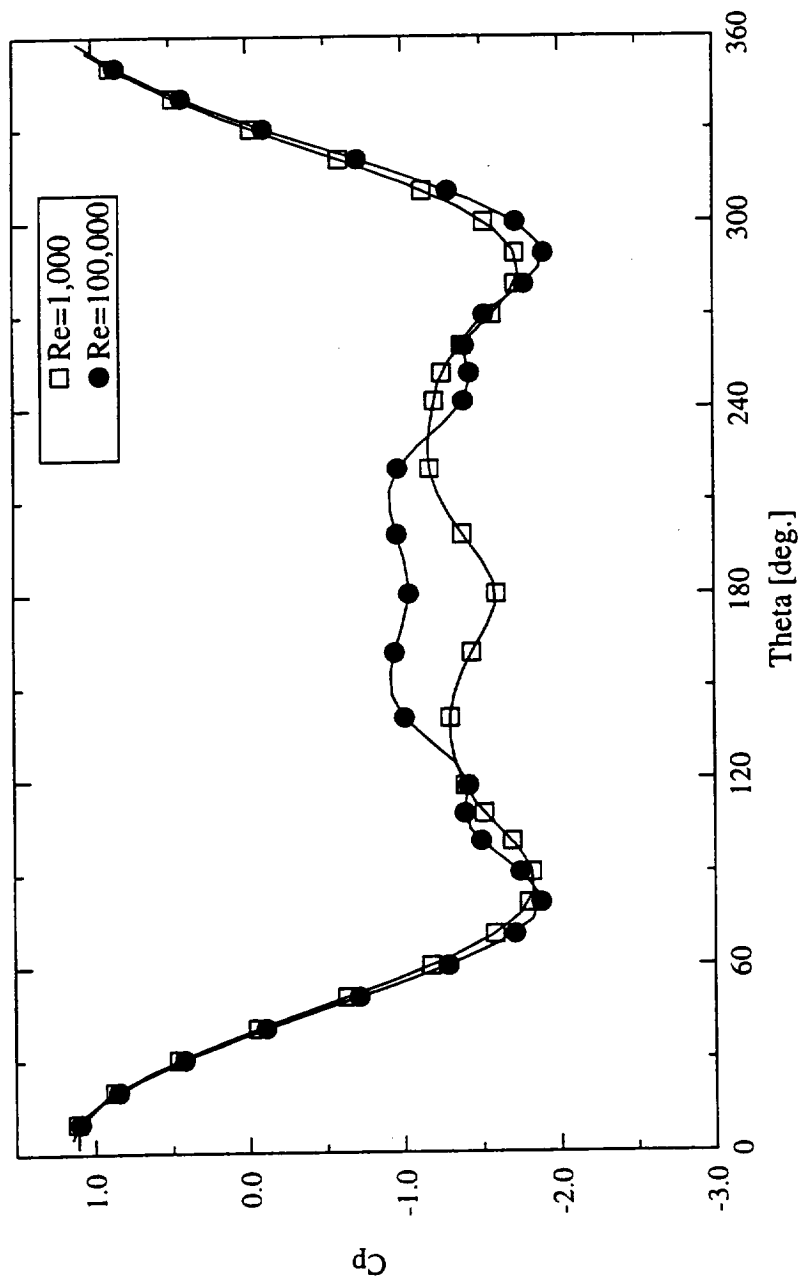


Fig. 5.6 Comparison of pressure distributions along a circular cylinder at  $Re = 1 \times 10^3$  and  $Re = 1 \times 10^5$ .

### 5.3 Steady and Unsteady Computations

It is always desirable to reduce the computational time. To reduce the computational time using steady state solution as an initial condition for the time dependent problem was attempted. A few thousands of iterations are performed under the steady state assumption, which takes approximately two to three hours. After that the steady state calculation was initiated. It was expected that starting unsteady calculation with a “better” initial condition compared to the impulsive start can reduce the computational time. However, it was found that there are little difference in computational time with the “better” initial condition: after an unsteady calculation is initiated the same amount of computational time was required to achieve the periodic fluctuating mode. Thus no advantage was found to use a “better” initial condition.

On the other hand, employing the steady flow assumption can reduce the calculation time by one tenth in comparison to the unsteady flow case. Moreover, it is expected that when the jet injected cases are performed, an extremely small time step is required to overcome the violation of the local CFL condition. The use of a very small time step is a serious problem not only because of increasing the computational time but also because of the “machine error” due to a large difference in the order of magnitude of the dependent variables from the time step. Thus, employing the steady state assumption is highly desirable. However, care must be taken in using the steady flow assumption because the flow around a circular cylinder in the Reynolds number range investigated is essentially unsteady. Therefore investigations were conducted to examine the relevance of the use of the steady flow assumption in the following sections. To confirm the results of comparison between the steady and the unsteady cases, investigations have been performed at two different Reynolds numbers, namely  $Re = 1 \times 10^5$  and  $Re = 1 \times 10^3$ .

#### 5.3.1 Drag Coefficient, Lift Coefficient and Residual History

Figures 5.7 show the drag and the lift coefficients plotted versus the number of iteration for the  $Re = 1 \times 10^5$  case. The corresponding residual history of the pressure,  $u$ - and  $v$ -velocity components are presented in Fig. 5.8. The systematic oscillation of the drag as well as the lift coefficients can be seen after the initial oscillation. Almost dynamically-steady oscillation is achieved beyond approximately 2500 iterations. The residual history reinforces the fact that the periodic oscillation is not due to the transitional

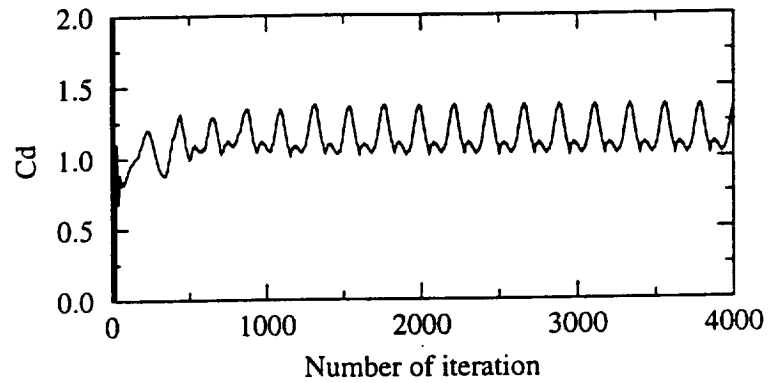


Fig. 5.7a The drag coefficient history with number of iteration for  $Re = 1 \times 10^5$  case.

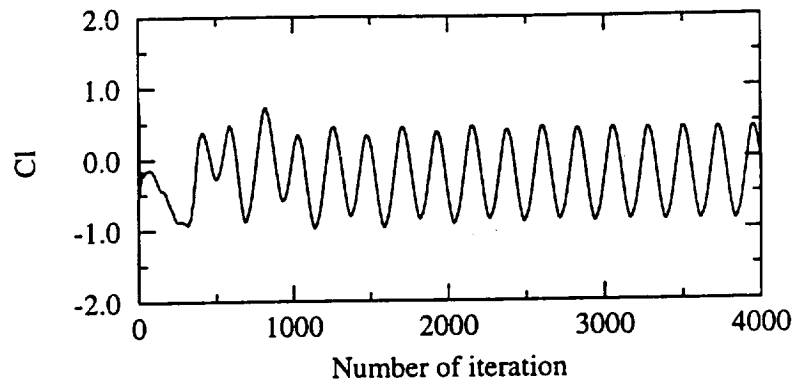


Fig. 5.7b The lift coefficient history with number of iteration for  $Re = 1 \times 10^5$  case.

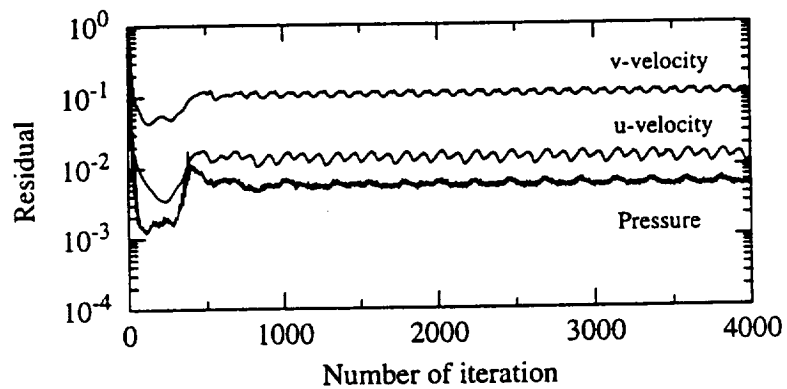


Fig. 5.8 Residual history with number of iteration for  $Re = 1 \times 10^5$  case.

error which can be seen at less than 1000 of iteration in Fig. 5.8. The similar results for the  $Re = 1 \times 10^3$  case are illustrated in Figs. 5.9 and 5.10. The averaged drag coefficients are summarized in Table 5.3 and compared with the values from the unsteady calculation.

### 5.3.2 Pressure Distributions

The pressure distributions along the cylinder surface are compared next. Once the residual history shows that the periodic oscillation mode has begun, the average pressure distributions are obtained by taking an average over five cycles of the period based on the lift coefficient oscillation. For the  $Re = 1 \times 10^5$  case, averaging was performed beyond 2154 iteration point in Figs. 5.8 and 5.9 while a value of 1002 in Figs. 5.9 and 5.10 was chosen for the  $Re = 1 \times 10^3$  case. Figure 5.11 shows the comparison between the steady state and unsteady state calculations for the  $Re = 1 \times 10^5$  case. The steady state calculation has a reasonable agreement with the unsteady calculation. Figure 5.12 depicts the results for the  $Re = 1 \times 10^3$  case. At this Reynolds number, a larger difference is seen between the steady and unsteady calculations.

### 5.3.3 Streamlines

To compare the trend in the pattern of the flow field between the unsteady and steady cases, the stream lines are plotted at the maximum, middle and minimum lift coefficient points after the periodic oscillation mode is established. The middle point was taken on the way from the maximum to the minimum point. The streamlines for the  $Re = 1 \times 10^5$  case are shown in Figs. 5.13 for the unsteady computation and in Figs. 5.14 for the steady calculation. The separation bubbles are captured at about  $\theta = \pm 120^\circ$  in Figs. 5.13b and c. It can be seen that a larger eddy is produced at the base portion of the cylinder and transported in the downstream direction in Figs. 5.13. The pattern shown in Fig. 5.13b is in good agreement with the result obtained by Ishii et al. [9]. The similar patterns are seen for the steady case in Figs. 5.14. The results for  $Re = 1 \times 10^3$  cases are shown in Figs. 5.15 and 5.16, respectively. The patterns of the streamlines for the lower Reynolds number case near the cylinder are different from the higher Reynolds number case. It is noted that the vortex behind the cylinder for the unsteady case is located closer to the cylinder than the steady case.

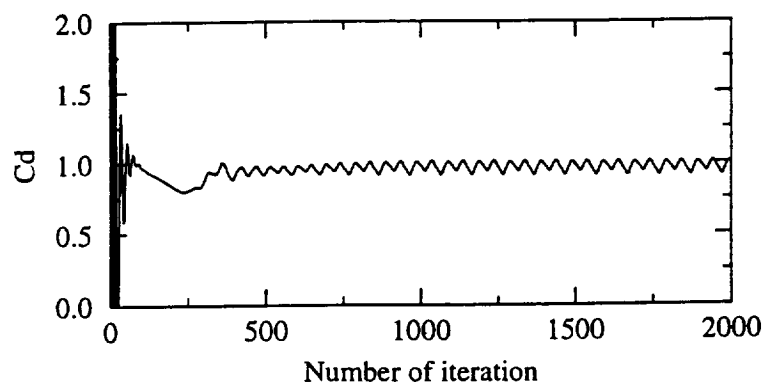


Fig. 5.9a The drag coefficient history with number of iteration for  $Re = 1 \times 10^3$  case.

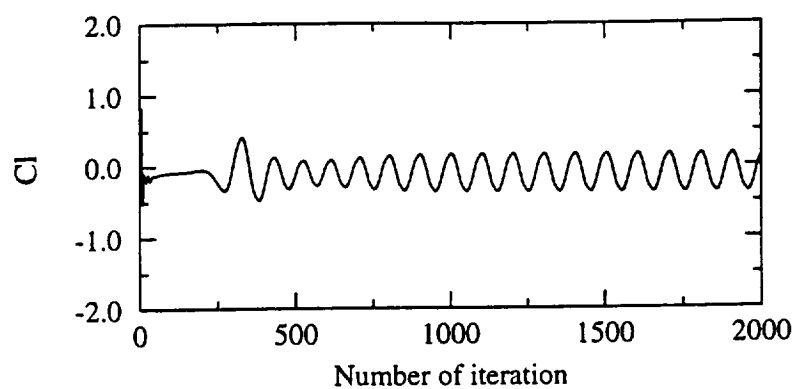


Fig. 5.9b The lift coefficient history with number of iteration for  $Re = 1 \times 10^3$  case.

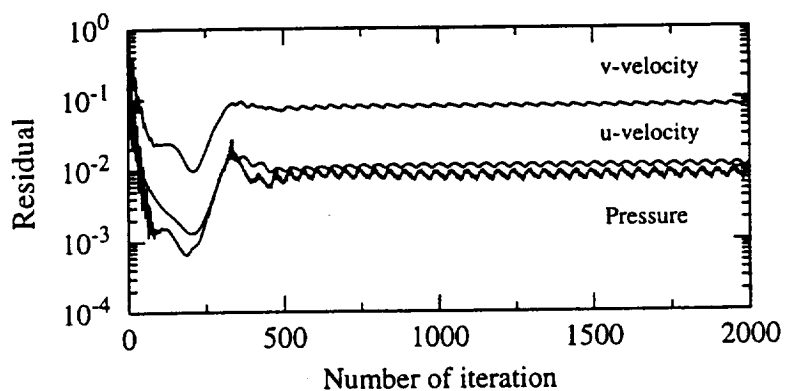


Fig. 5.10 Residual history with number of iteration for  $Re = 1 \times 10^3$  case.

Table 5.3 Comparison of the drag coefficient for steady and unsteady calculations.

$C_D$	Steady calculation	Unsteady calculation
$Re = 1 \times 10^5$	1.15	1.00
$Re = 1 \times 10^3$	0.970	1.36

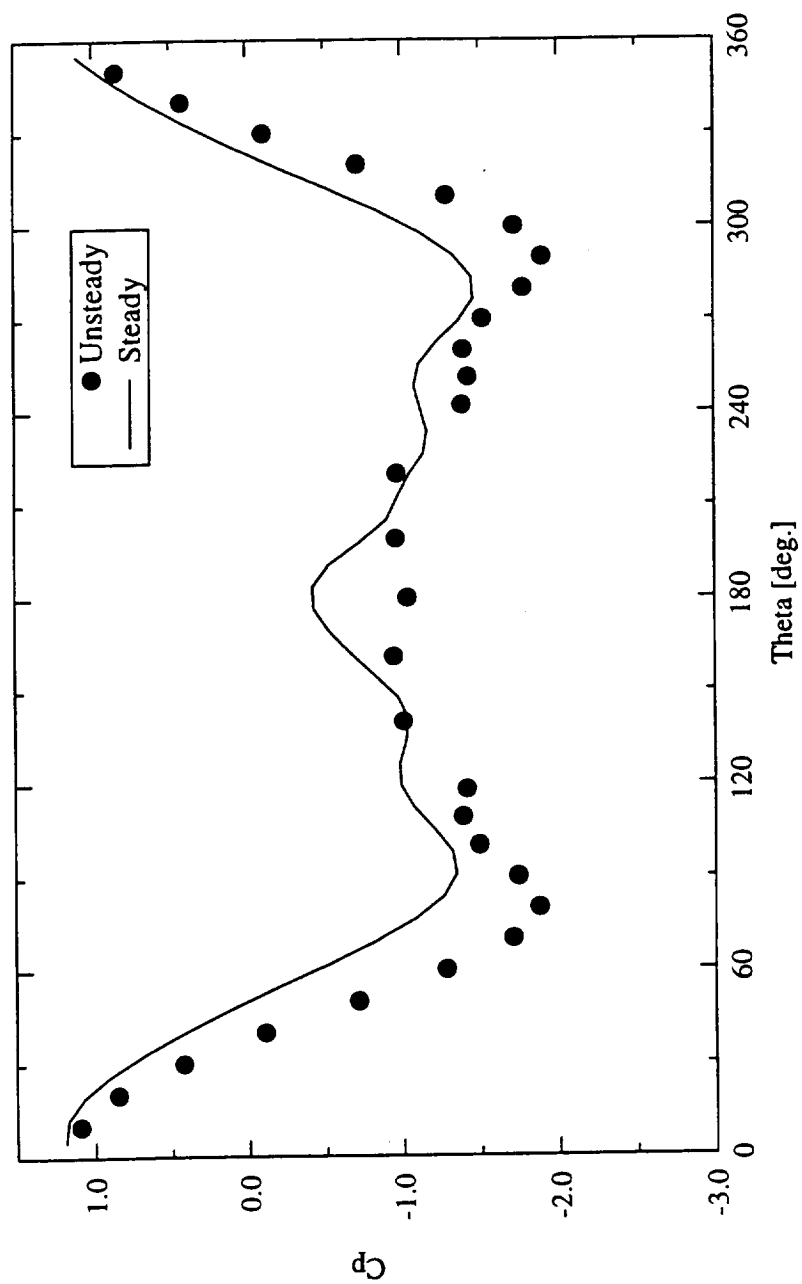


Fig. 5.11 Comparison of pressure distributions along a cylinder at  $Re = 1 \times 10^5$  obtained from steady and unsteady calculations.



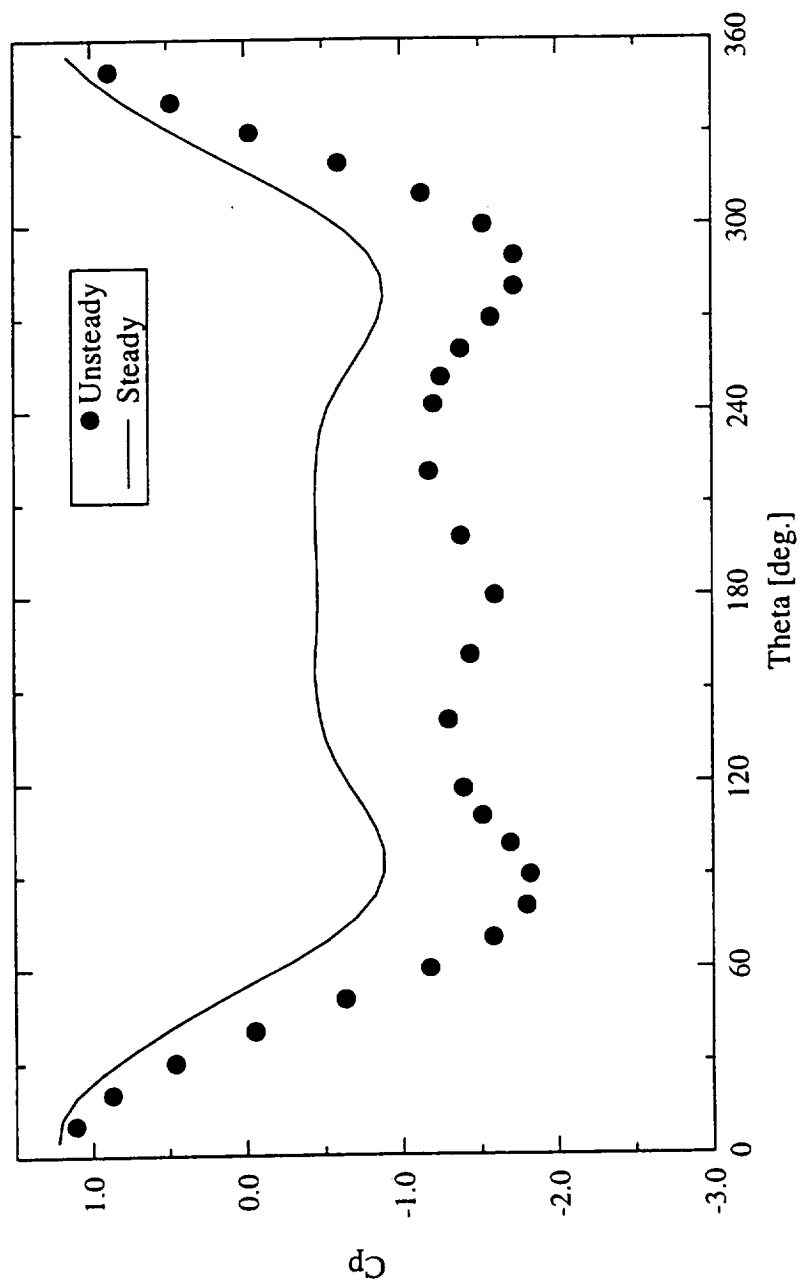
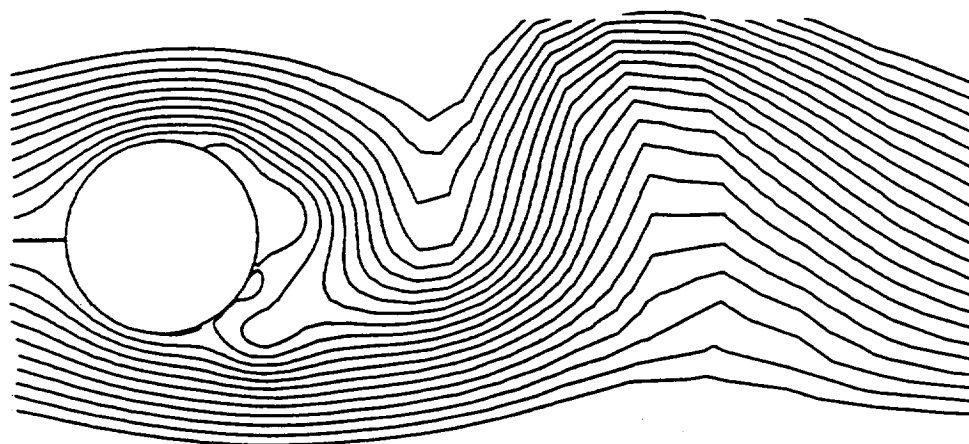
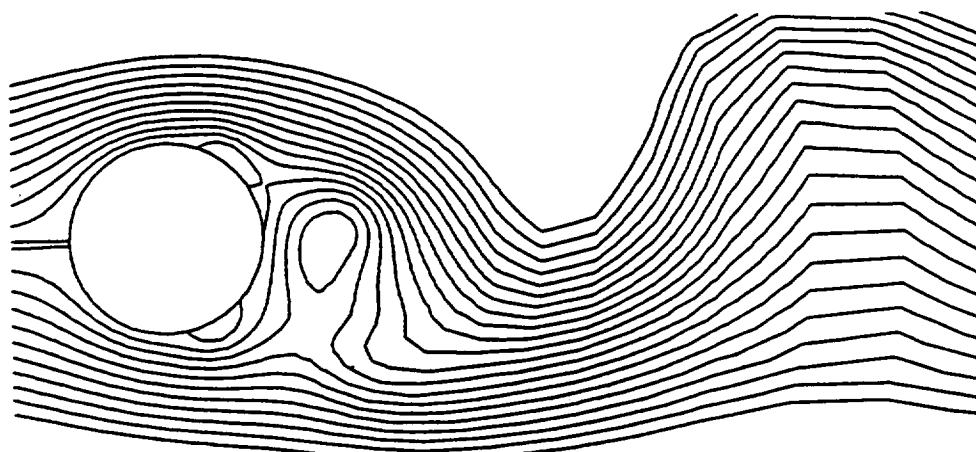


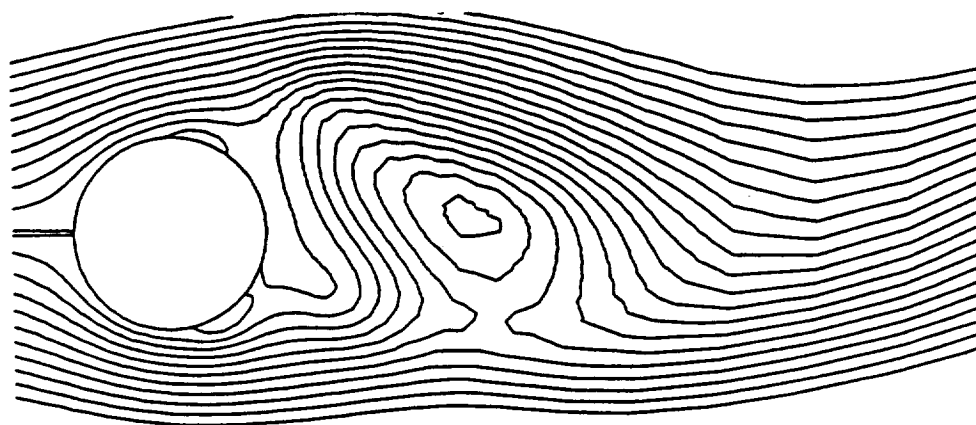
Fig. 5.12 Comparison of pressure distributions along a cylinder at  $Re = 1 \times 10^3$  obtained from steady and unsteady calculations.



(a) At the maximum  $C_L$  point

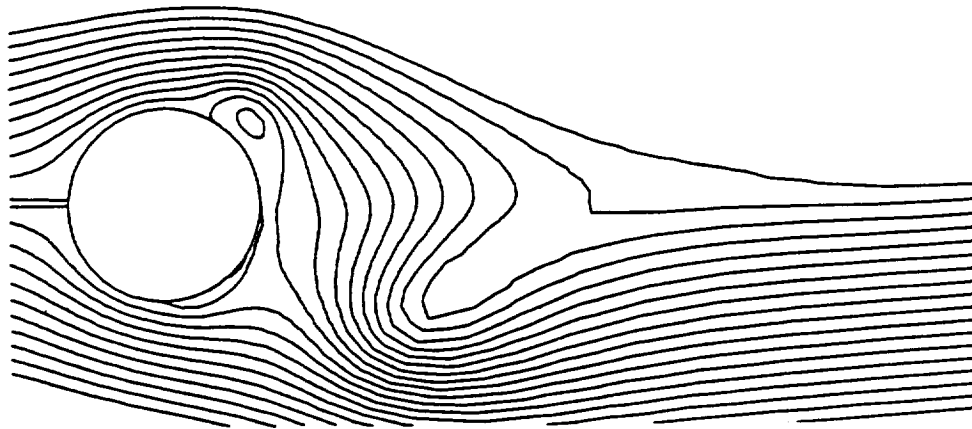


(b) At the middle  $C_L$  point

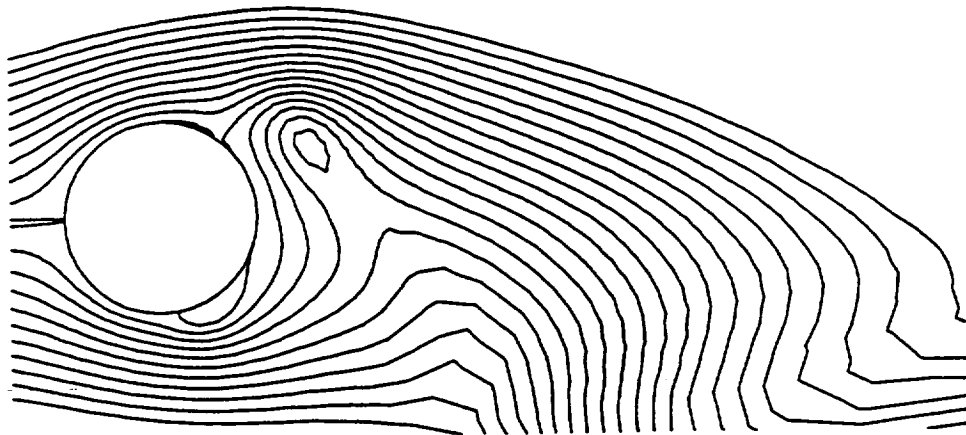


(c) At the minimum  $C_L$  point

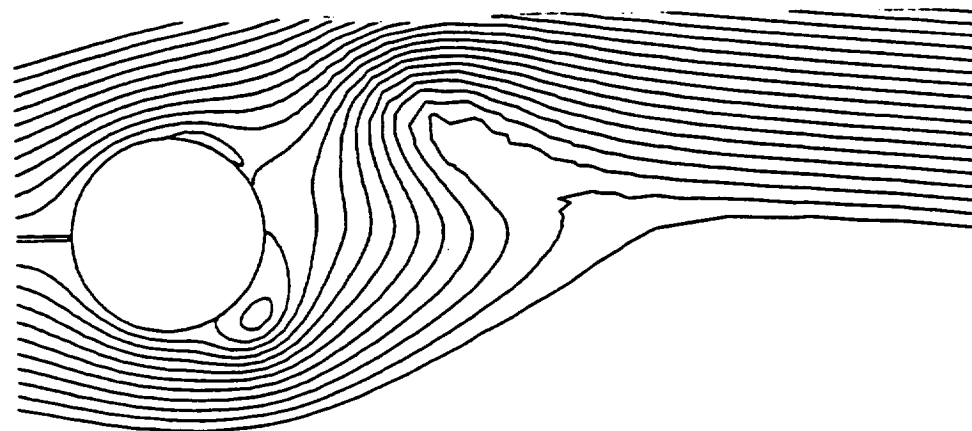
Fig. 5.13 Streamlines from the unsteady computation at  $Re = 1 \times 10^5$ .



(a) At the maximum  $C_L$  point

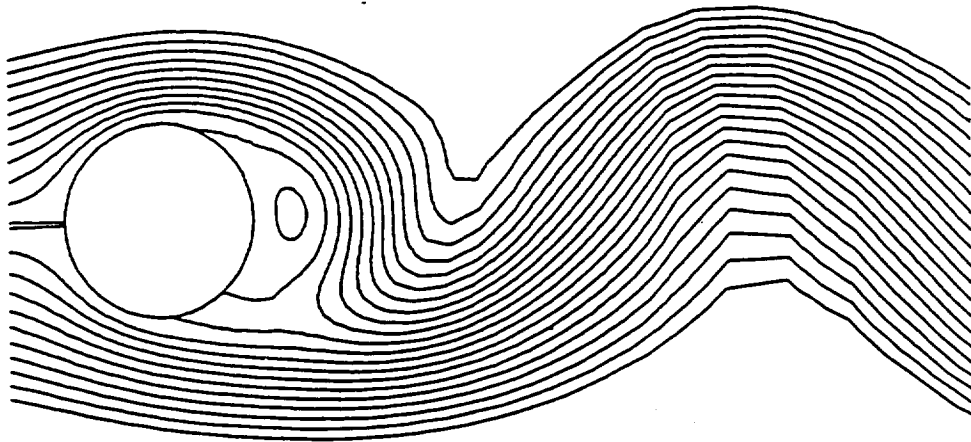


(b) At the middle  $C_L$  point

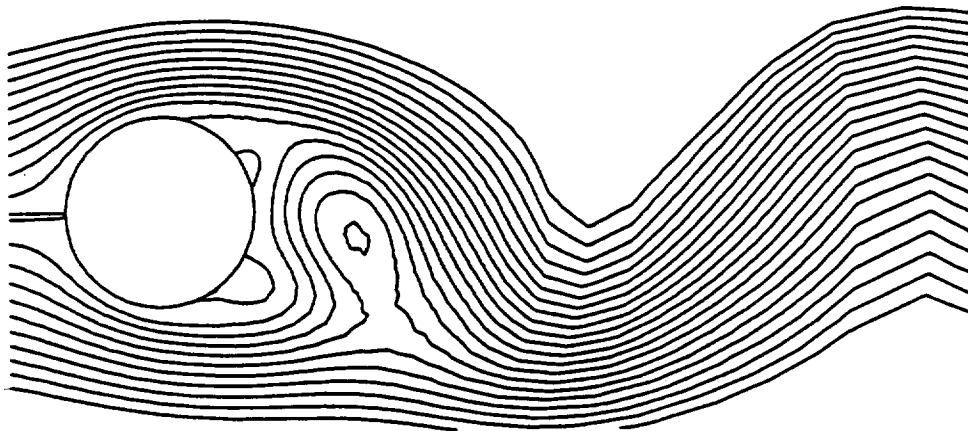


(c) At the minimum  $C_L$  point

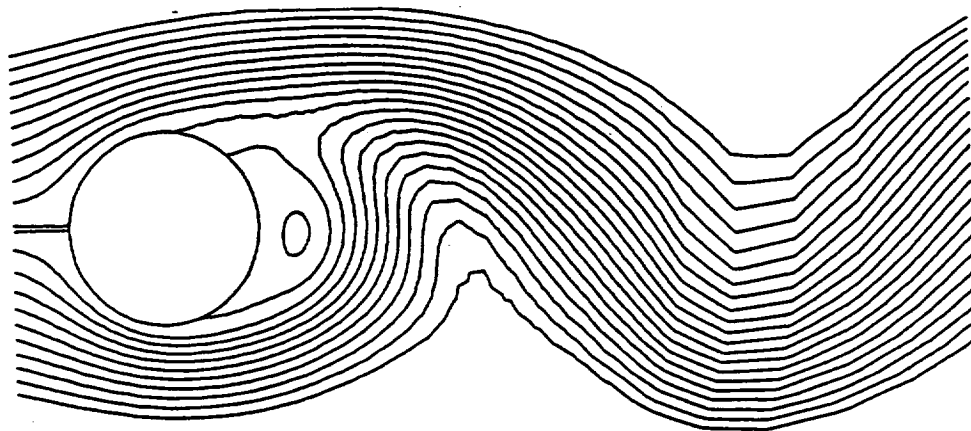
Fig. 5.14 Streamlines from the steady computation at  $Re = 1 \times 10^5$ .



(a) At the maximum  $C_L$  point

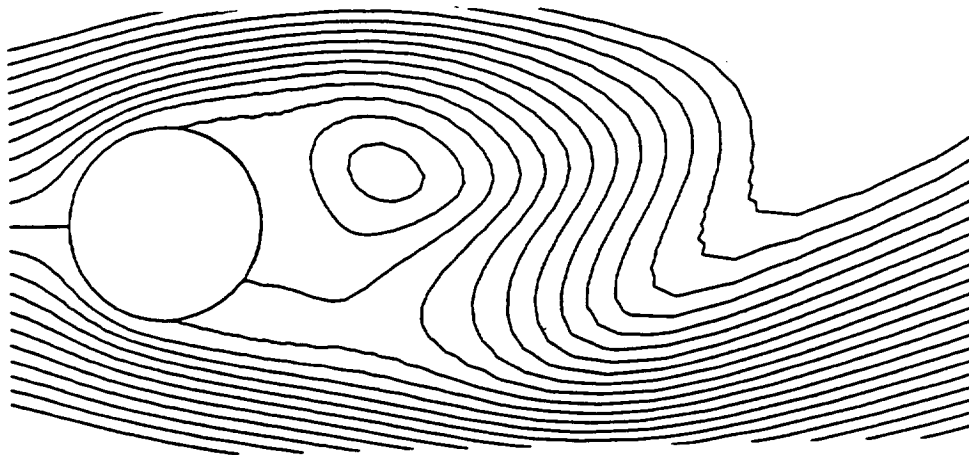


(b) At the middle  $C_L$  point

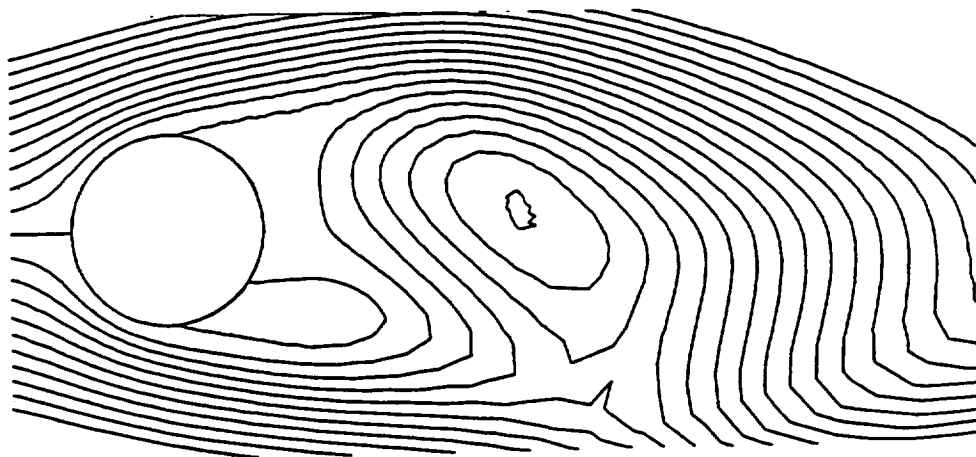


(c) At the minimum  $C_L$  point

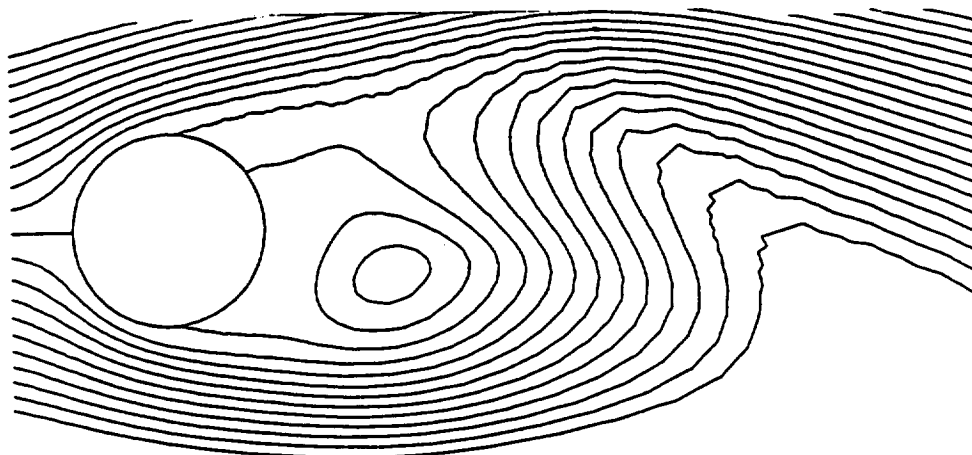
Fig. 5.15 Streamlines from the unsteady computation at  $Re = 1 \times 10^3$ .



(a) At the maximum  $C_L$  point



(b) At the middle  $C_L$  point



(c) At the minimum  $C_L$  point

Fig. 5.16 Streamlines from the steady computation at  $Re = 1 \times 10^3$ .

### 5.3.4 Velocity Vectors

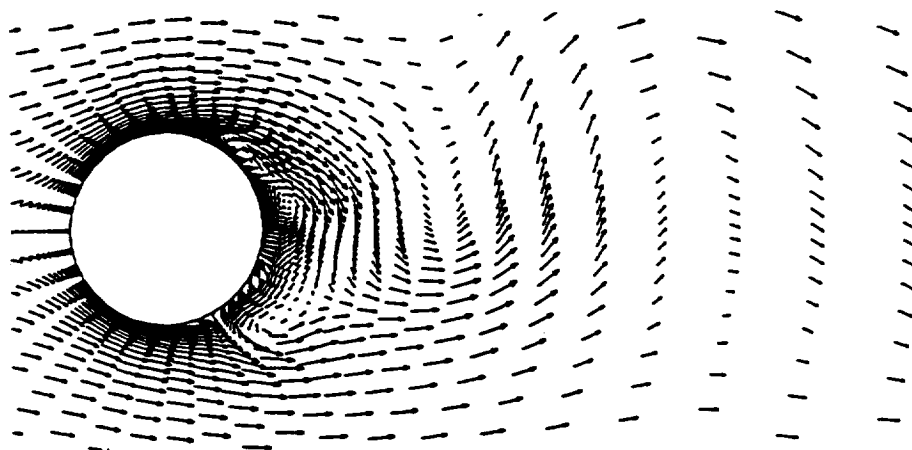
The corresponding velocity vectors to the streamlines are also compared between the unsteady and steady calculations. The patterns for the  $Re = 1 \times 10^5$  cases are depicted in Figs. 17 for the unsteady cases and in Figs. 18 for the steady cases. The vortices corresponding to the streamlines can be seen for both the unsteady and steady cases. These results demonstrate the expected velocity vector distributions. For the  $Re = 1 \times 10^3$  cases, the patterns are illustrated in Figs. 19 for the unsteady cases and in Figs. 20 for the steady cases. The characteristics of the streamlines are also seen in the velocity vector plots.

### 5.4 Grid Size Dependency

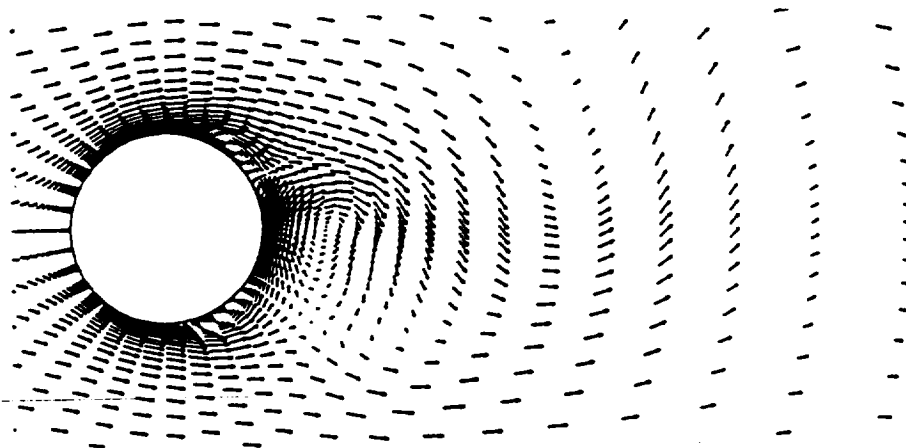
Investigations were conducted to study the effect of the size of the cells. The smallest cell size near the wall was carefully selected to be small enough to represent the boundary-layer profile correctly based on the theoretical assumption. However, it is important to investigate the effect of the cell size, especially in the wake region behind the cylinder where massive separated flow is expected. Departing from the original grid size 55x51, two grid sizes were tested namely 29x26 and 110x102 grids. Figure 5.21 shows the comparison of the pressure distributions for the three different grid sizes. It is noted that the impact of the grid size on the pressure distribution is not significant. The average drag coefficient for each grid size is summarized in Table 5.4. The drag coefficient for the 55x51 grid case is very close to that for the 110x102 grid case while the one for the 29x26 grid cases shows a lower value.

### 5.5 Effect of the Area of Physical Domain

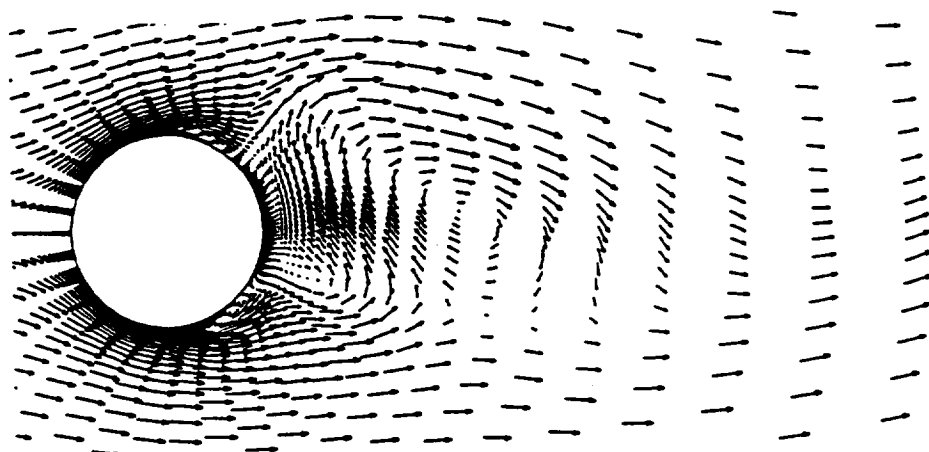
The effect of the location of the outer boundary was also studied. To construct the corresponding grid to the different computational area, the cells were removed or added keeping the cell sizes near the cylinder constant. The location of the outer boundary was selected at the five, nine and eighteen times of the cylinder diameter. Figure 5.22 shows the comparison of the pressure distributions for the three different computational areas. The profiles of the pressure distributions show little difference for the different computational areas. The average drag coefficients for each computational area case are summarized in Table 5.5. Table 5.4 also shows that there is no significant discrepancy for different computational areas.



(a) At the maximum  $C_L$  point

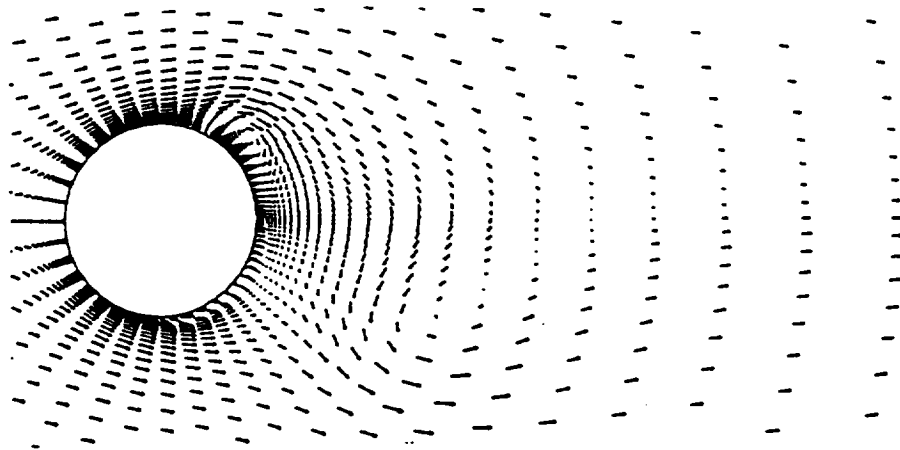


(b) At the middle  $C_L$  point

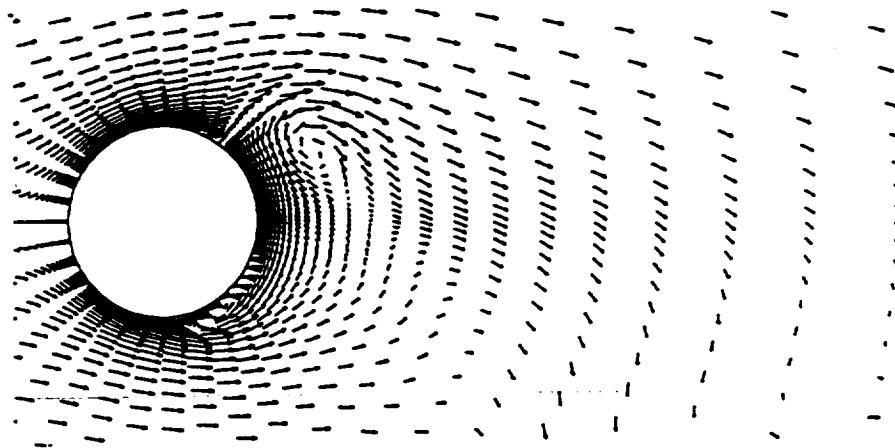


(c) At the minimum  $C_L$  point

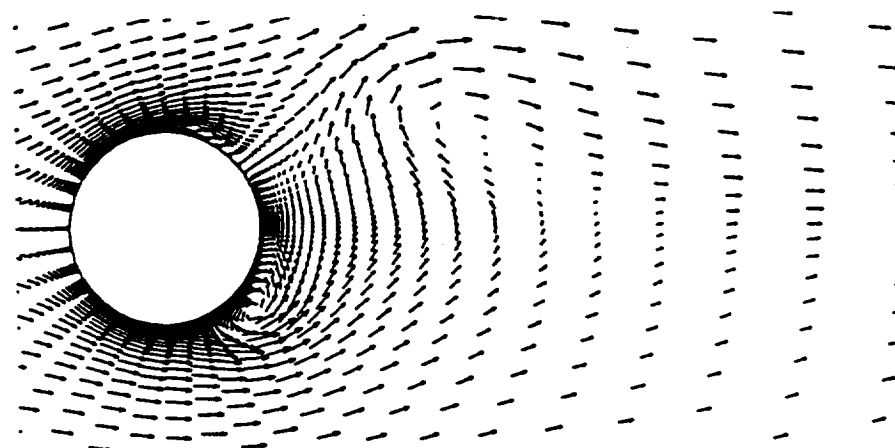
Fig. 5.17 Velocity vectors from the unsteady computation at  $Re = 1 \times 10^5$ .



(a) At the maximum  $C_L$  point



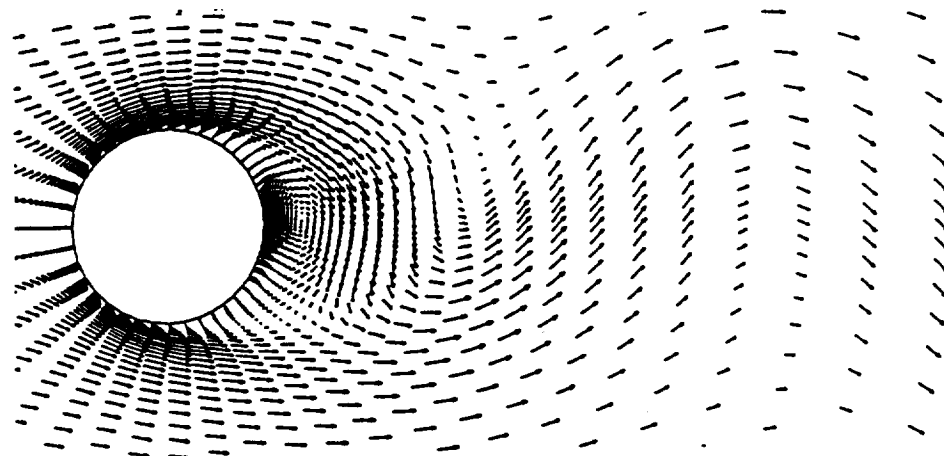
(b) At the middle  $C_L$  point



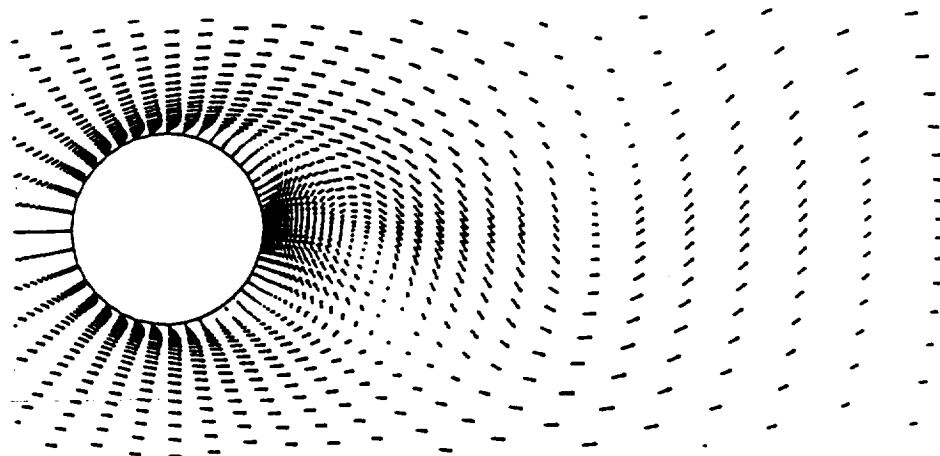
(c) At the minimum  $C_L$  point

Fig. 5.18 Velocity vectors from the steady computation at  $Re = 1 \times 10^5$ .

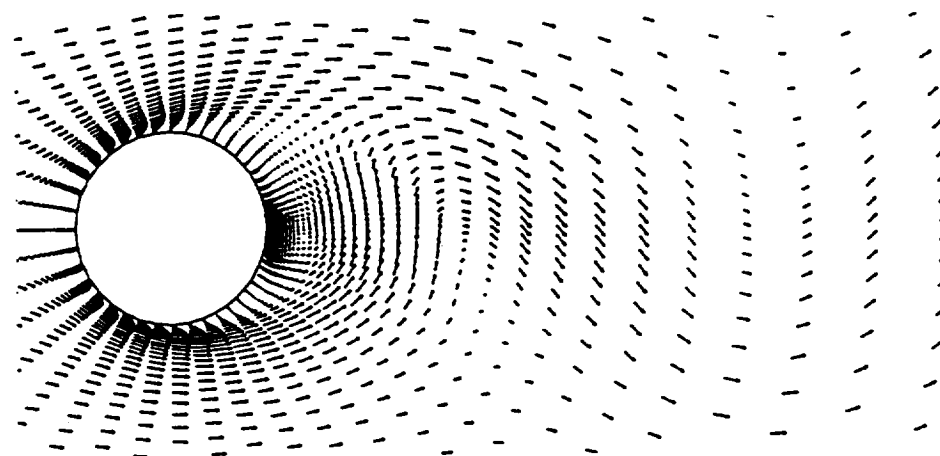




(a) At the maximum  $C_L$  point

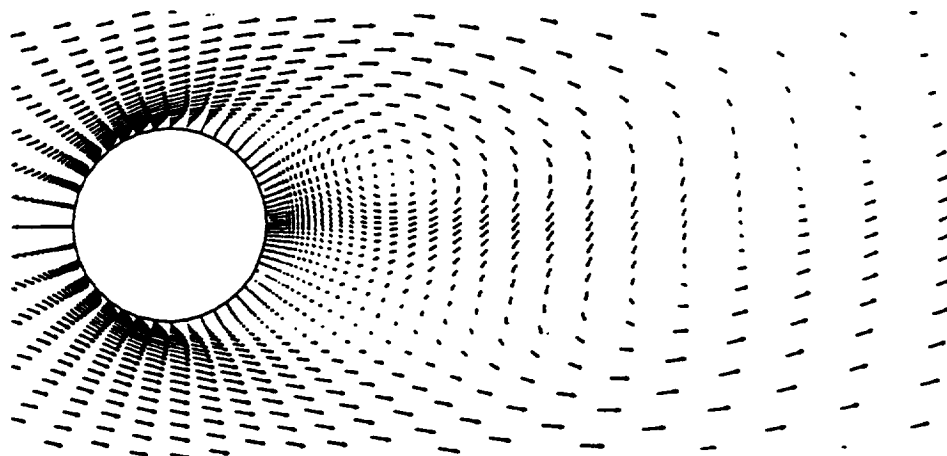


(b) At the middle  $C_L$  point

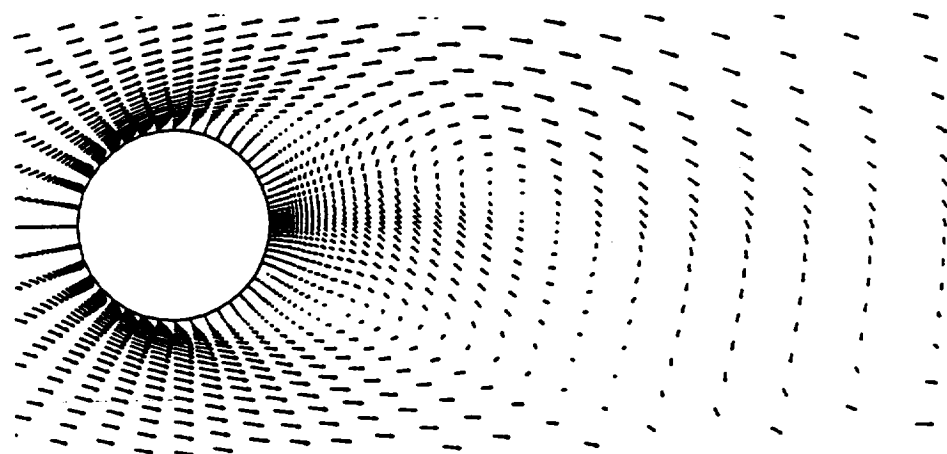


(c) At the minimum  $C_L$  point

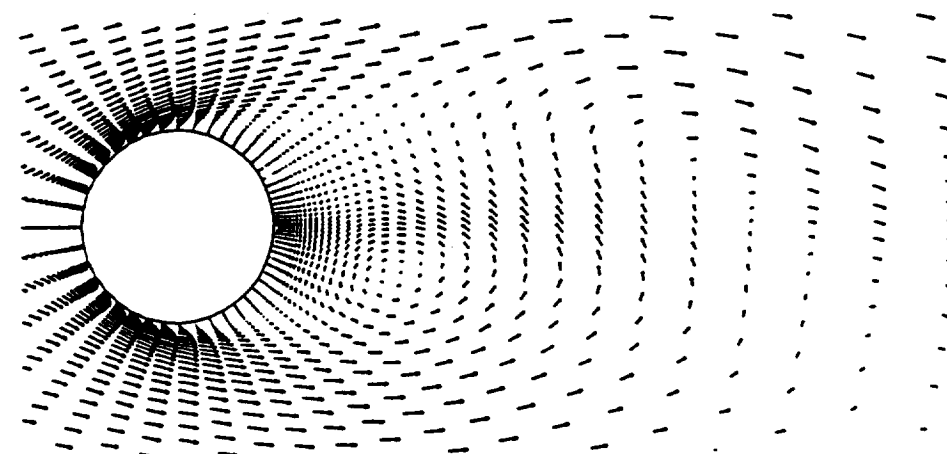
Fig. 5.19 Velocity vectors from the unsteady computation at  $Re = 1 \times 10^3$ .



(a) At the maximum  $C_L$  point



(b) At the middle  $C_L$  point



(c) At the minimum  $C_L$  point

Fig. 5.20 Velocity vectors from the steady computation at  $Re = 1 \times 10^3$ .

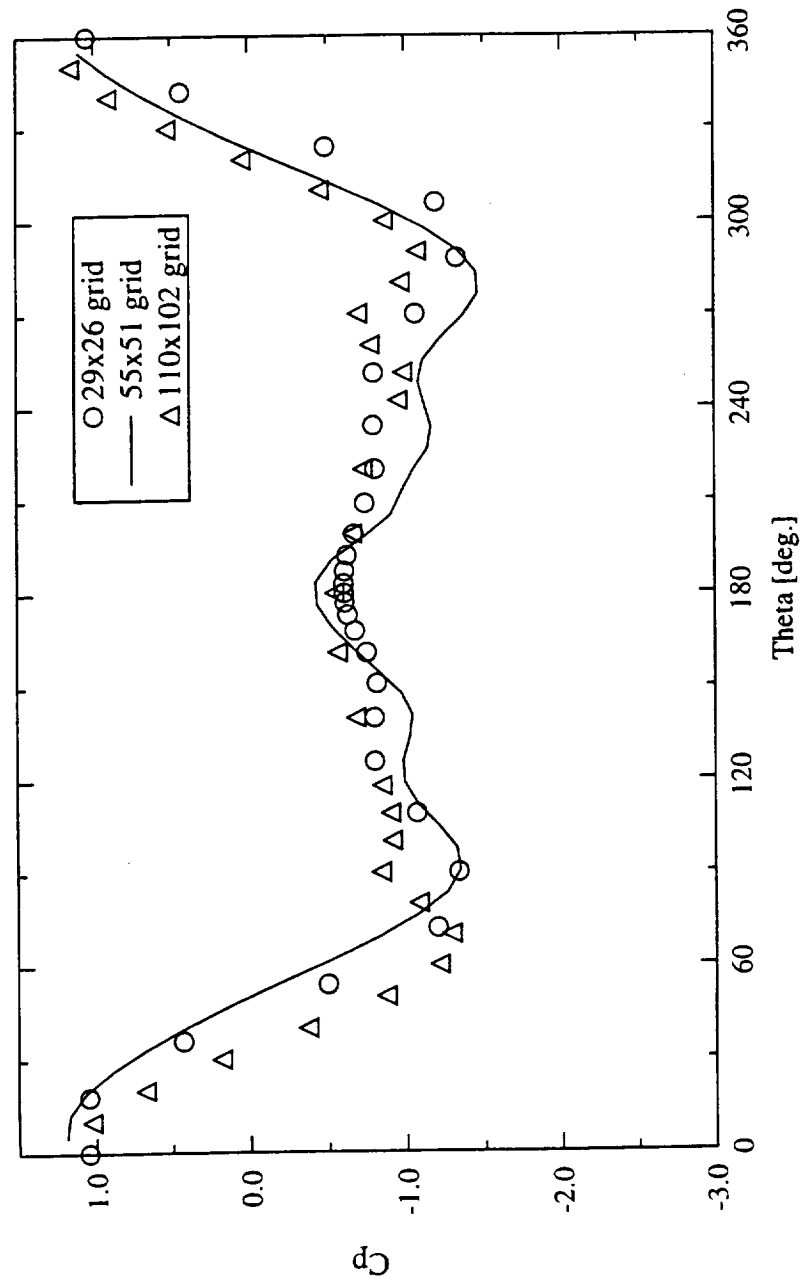


Fig. 5.21 Comparison of pressure distributions along a cylinder at  $Re = 1 \times 10^5$  for different size of grids.

Table 5.4 Comparison of the drag coefficient for the different grid sizes

Grid size	29x26 grid	55x51 grid	110x102 grid
$C_D$	0.830	1.15	1.12

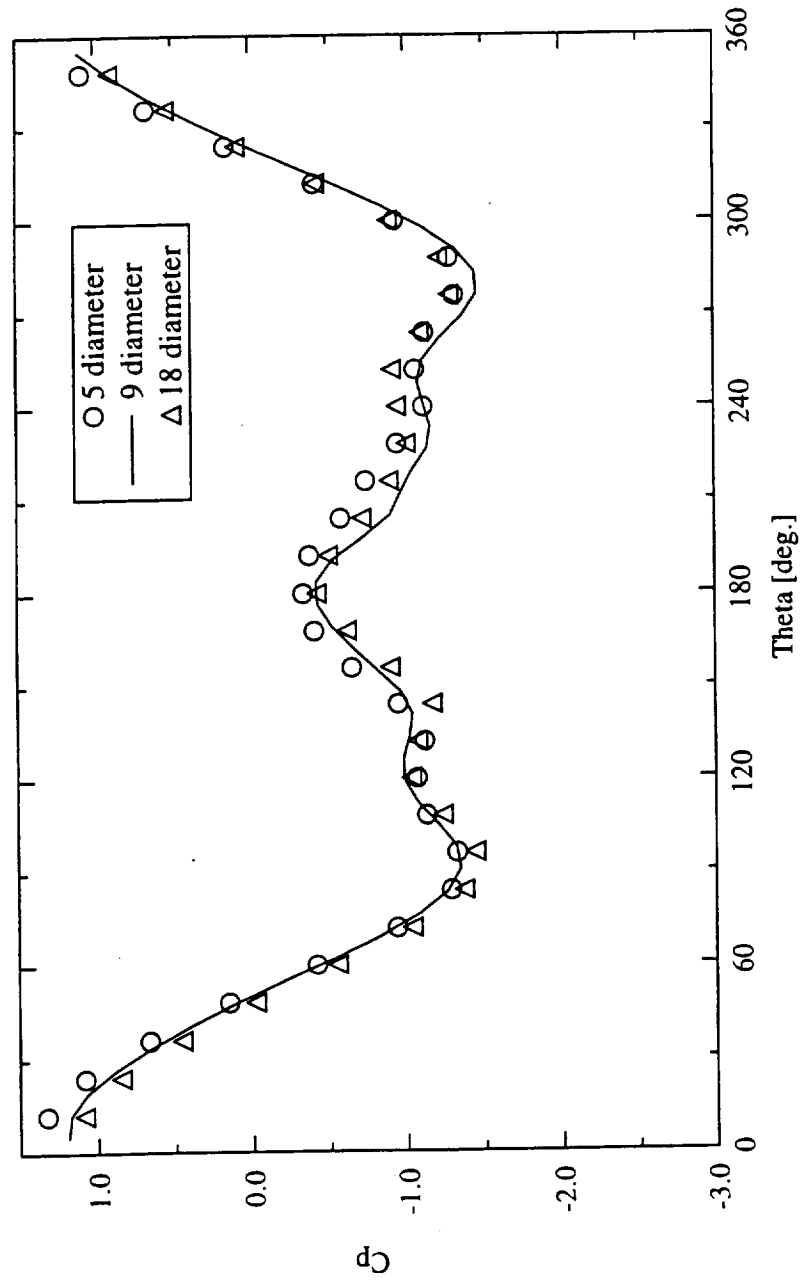


Fig. 5.22 Comparison of pressure distributions along a cylinder at  $Re = 1 \times 10^5$  for different size of computational areas.

Table 5.5 Comparison of the drag coefficient for the different size of computational areas.

Outer boundary	5 diameter	9 diameter	18 diameter
$C_D$	1.15	1.15	1.11

## Chapter VI

### RESULTS AND DISCUSSION

In this chapter, the validated computational fluid dynamics code is applied to obtain the results for the cylinder with jet blown from the tail. The results from the experimental investigation are also presented. Finally, comparisons for the selected cases from the numerical and experimental results are presented.

#### 6.1 Numerical Results

Based on the detailed validation of the computer code using the cylinder geometry, the results and discussion with jet cases are presented in the following sections.

##### 6.1.1 Pressure Distribution

The pressure distributions along the cylinder for the various jet momentum coefficients are shown in Fig. 6.1. The effect of the jet appears between  $\theta = \pm 70^\circ$ . From the front stagnation point to the minimum pressure point, there is no significant change due to injection of the jet. It is seen that there is little effect of the jet on the pressure distribution for the  $C_\mu = 0.0005$  case. As the amount of the jet ejected increases (the  $C_\mu = 0.0041$  case), the pressure coefficient  $C_p$  increases in the range of  $70^\circ \leq \theta \leq 290^\circ$  while the profile of the distribution in the range is remained. It is also seen that the effect of the jet on the pressure distribution does not limited to the local area near the jet but spreads into a broad range of the surface of the cylinder. When the jet-blowing momentum coefficient is increased further (the  $C_\mu = 0.053$  case and larger), the increased pressure in the  $70^\circ \leq \theta \leq 290^\circ$  region disappears and the pressure distribution has almost the same profile as the no jet and  $C_\mu = 0.0005$  cases.

##### 6.1.2 Drag Coefficient and Separation point

Figure 6.2 illustrates the effect of the jet on the drag coefficient as a function of the jet-blowing momentum coefficient. The  $C_\mu = 0.0$  case represents non-jet case. When the jet-blowing momentum coefficient is lower than 0.0005, there is no change in the drag

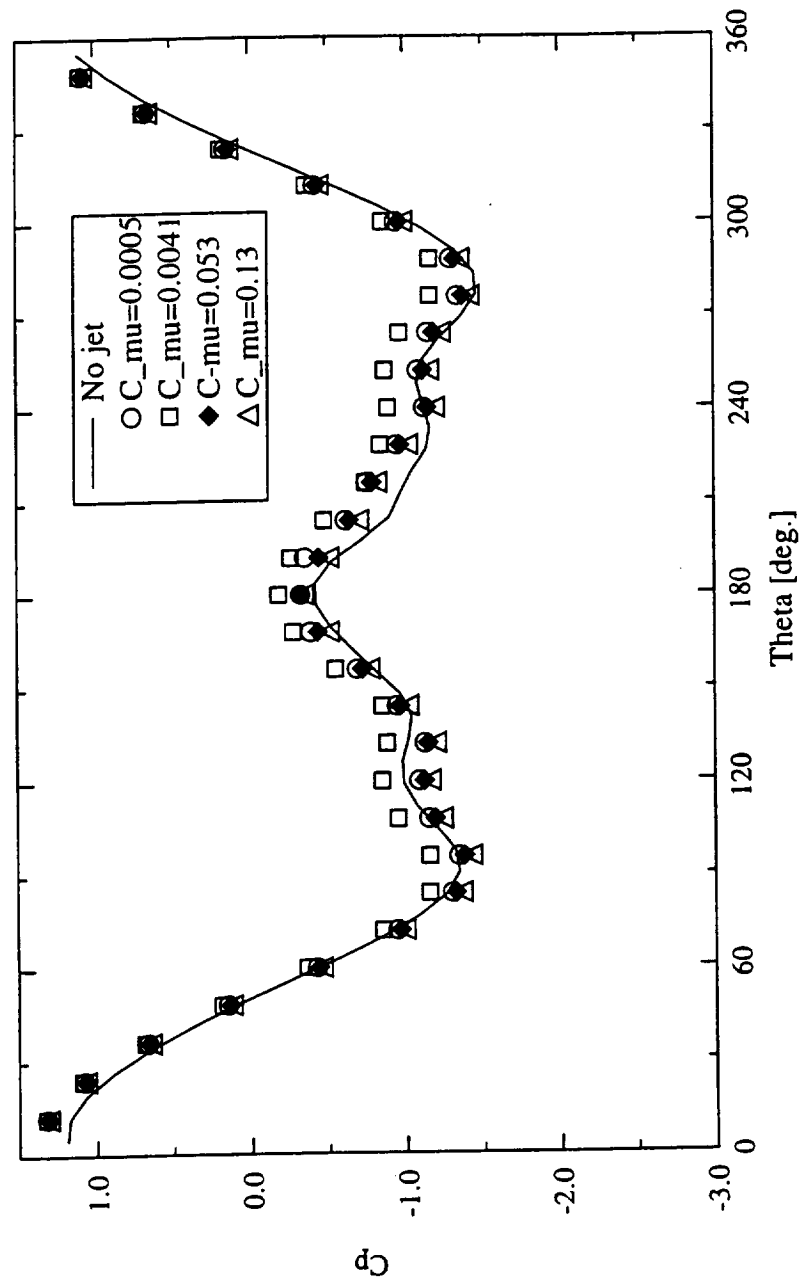


Fig. 6.1 Variations of pressure distribution with jet-blowing momentum coefficient  $C_{\mu}$ .



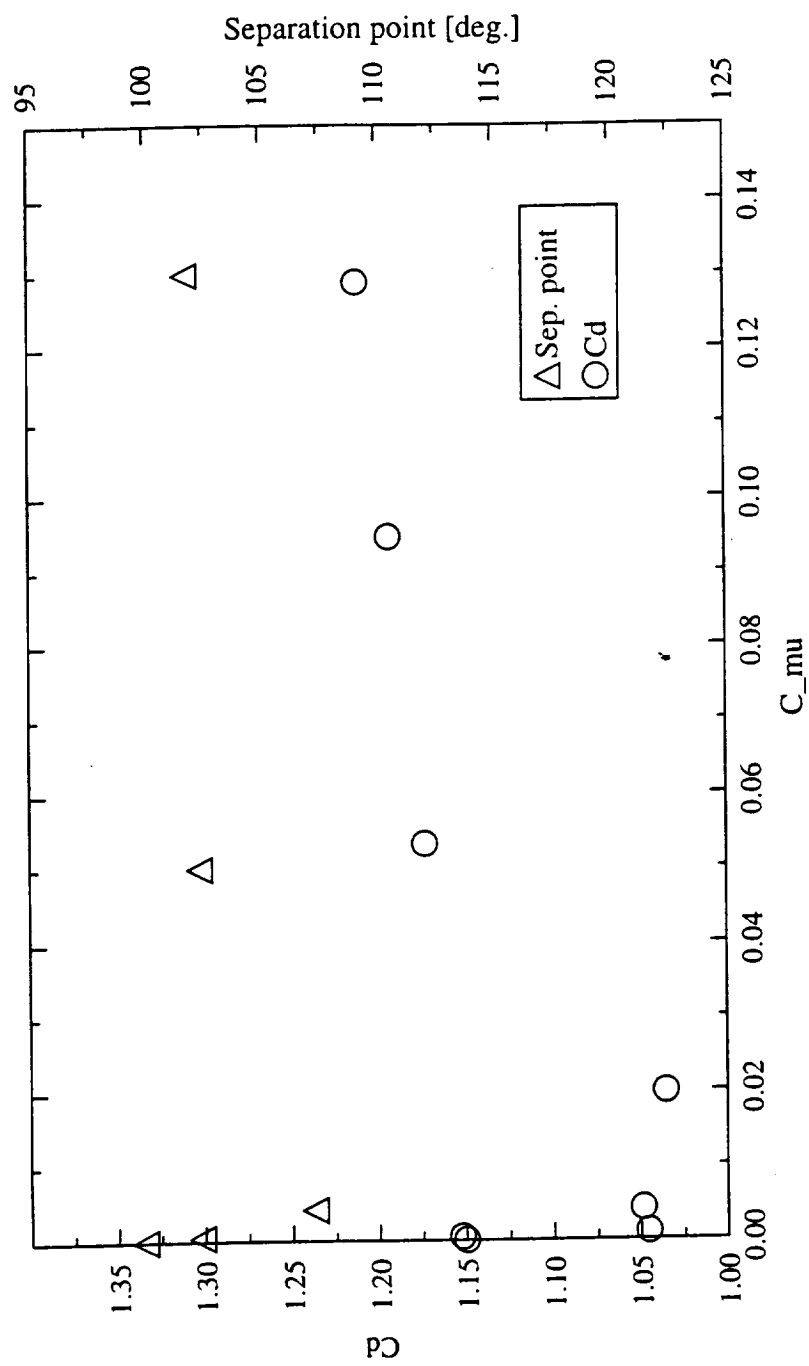


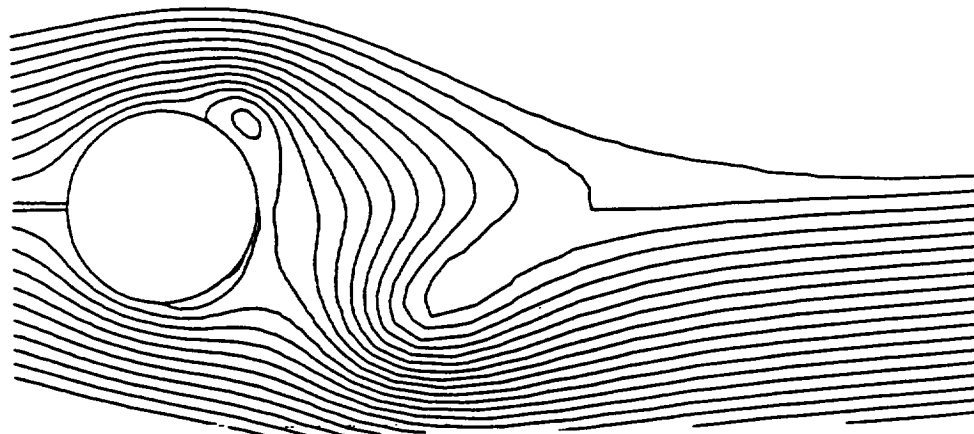
Fig. 6.2 Variation of the drag coefficient and the separation point with the jet-blowing momentum coefficient  $C_{\mu}$ .

coefficient. This is consistent with the result of the pressure distribution. The drag is decreased by the jet with the  $C_\mu$  between 0.001 and 0.02. However, as  $C_\mu$  is increased further, the drag coefficient has almost the same or even slightly higher value than the no-jet case. Although it cannot be possible to compare the results directly, this tendency is similar to the results numerically obtained by Mo and Duke [19]. They showed that as the jet-velocity-to-uniform-velocity ratio,  $u_j/u_\infty$ , increases the drag also increases. They conducted their computation in the region of  $u_j/u_\infty > 1.0$ . The point of  $C_\mu = 0.053$  corresponds to  $u_j/u_\infty = 0.72$ . They explained that the drag is increased by the rear stagnation jet because the jet contributes to the flow behind the cylinder to be accelerated which results in decreasing the static pressure in the region. However, the pressure decrease in that region (in the present study) is not clearly seen and that explanation can not be applied.

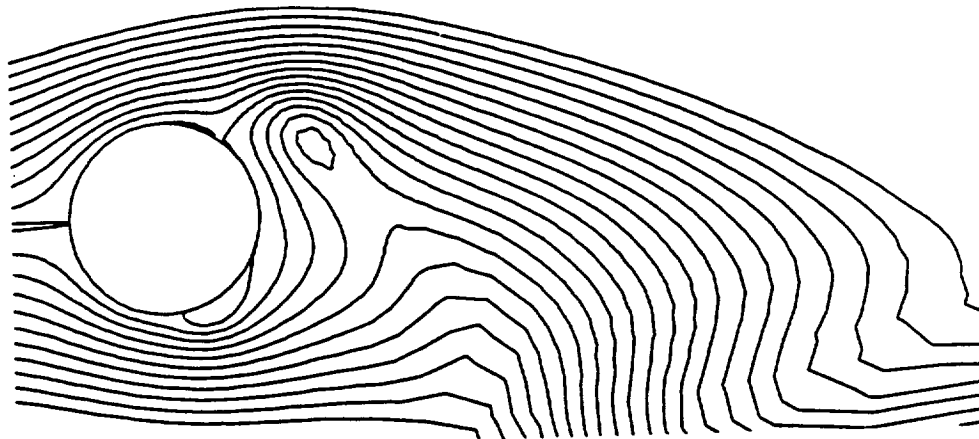
Also plotted in Fig. 6.2 are the variation of the separation point with  $C_\mu$ . The scale for the separation point is given on the right hand side of the figure. It is clearly seen that the variation of the separation point corresponds to that of the drag coefficient. When there is little effect of the jet on the drag, the separation point does not move much from the non-jet case value ( $\theta \approx 100^\circ$ ). However, when the drag is reduced by the jet, the separation point shifts towards the downstream. On the contrary, if the  $C_\mu$  increases and the drag is increased again, the separation points are also moved to the upstream and are located at almost the same position as the non-jet case. It is noted that the separation point for the  $C_\mu \geq 0.05$  cases remains slightly to the downstream of the non-jet case position, in contrast to the drag which has a tendency to go beyond the non-jet case.

### 6.1.3 Streamlines

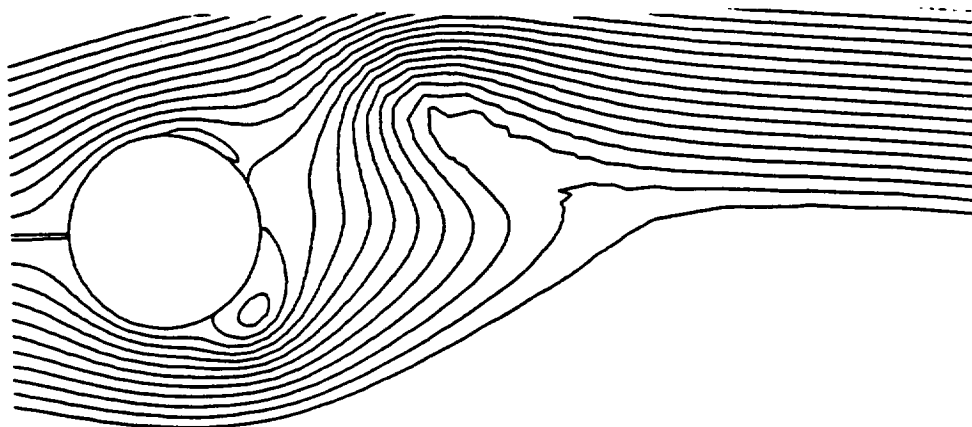
The stream functions are obtained to observe the effect of the jet in the flow field and to understand the mechanism of the drag reduction by the jet. The streamlines at the maximum, middle and minimum lift coefficient points are compared for the different  $C_\mu$  cases. The  $C_\mu = 0.0, 0.0005, 0.004, 0.05$  and  $0.13$  cases are selected to compare the streamlines. The streamlines for the no-jet case which is identical to Figs. 5.14 is presented here again for comparison. The result are depicted in Figs. 6.3 - 6.6. No significant changes are seen for the  $C_\mu = 0.0005$  case from the no-jet case in the streamline pattern. The flow field becomes more symmetric for the  $C_\mu = 0.004$  case as shown in Figs.



(a) At the maximum  $C_L$  point

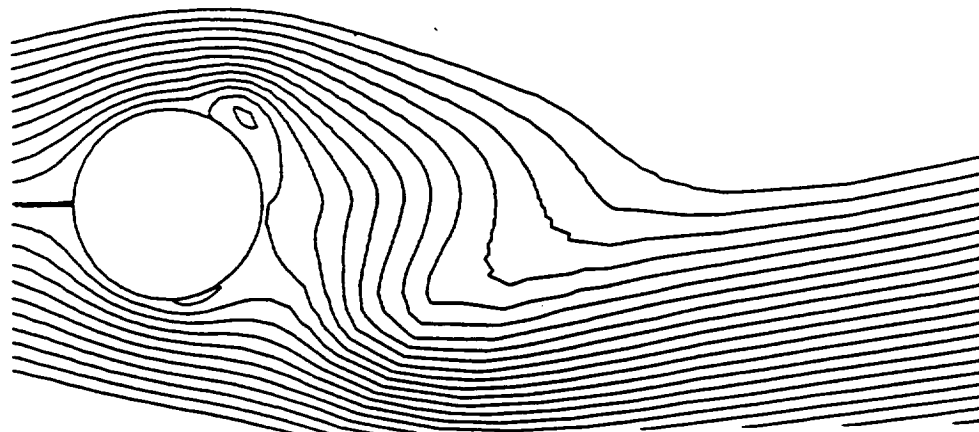


(b) At the middle  $C_L$  point

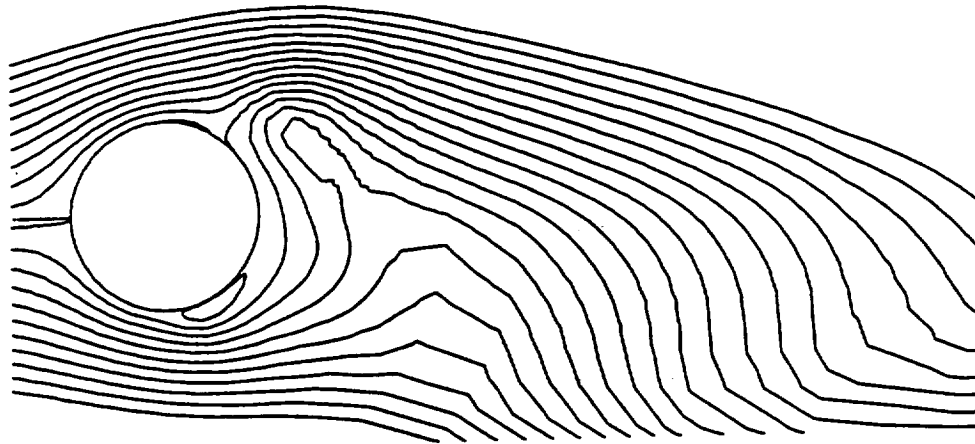


(c) At the minimum  $C_L$  point

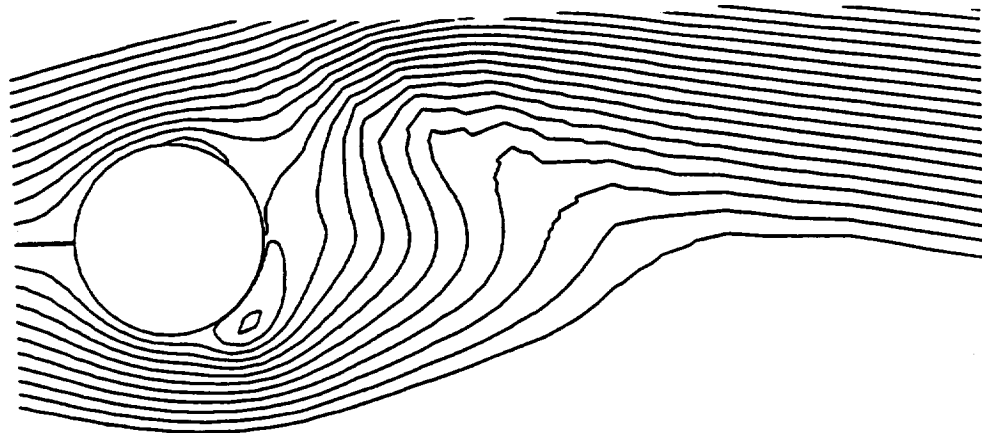
Fig. 6.3 Streamlines for the no-jet case.



(a) At the maximum  $C_L$  point

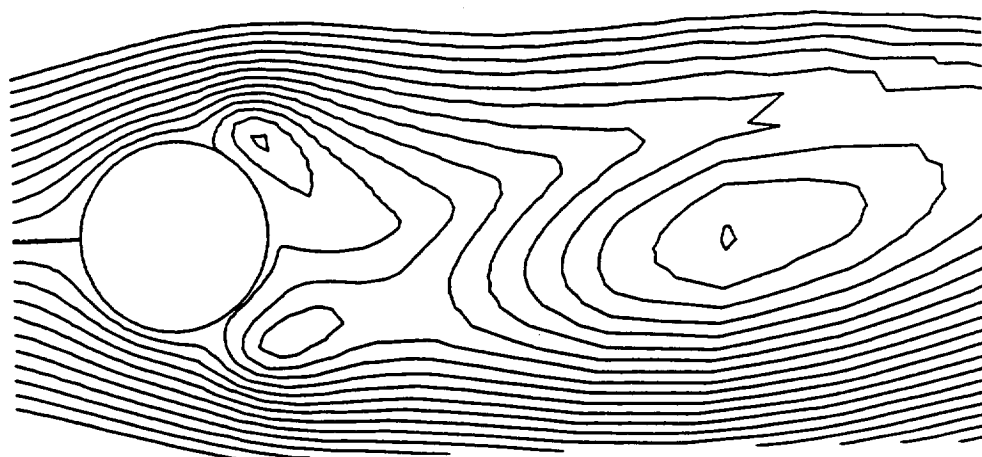


(b) At the middle  $C_L$  point

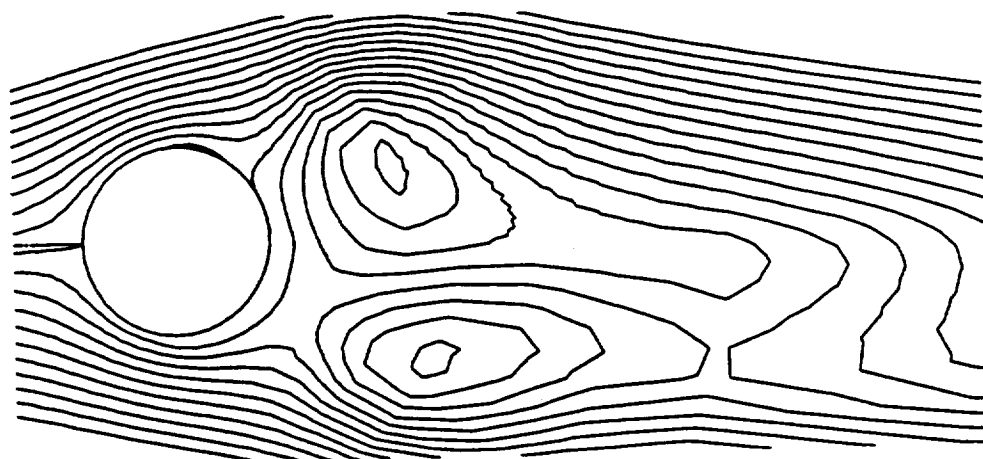


(c) At the minimum  $C_L$  point

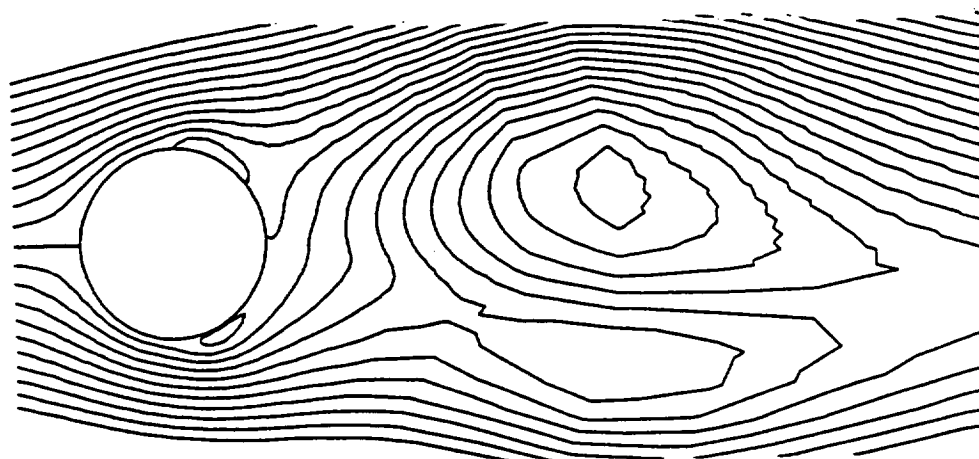
Fig. 6.4 Streamlines for the  $C_\mu=0.0005$  case.



(a) At the maximum  $C_L$  point

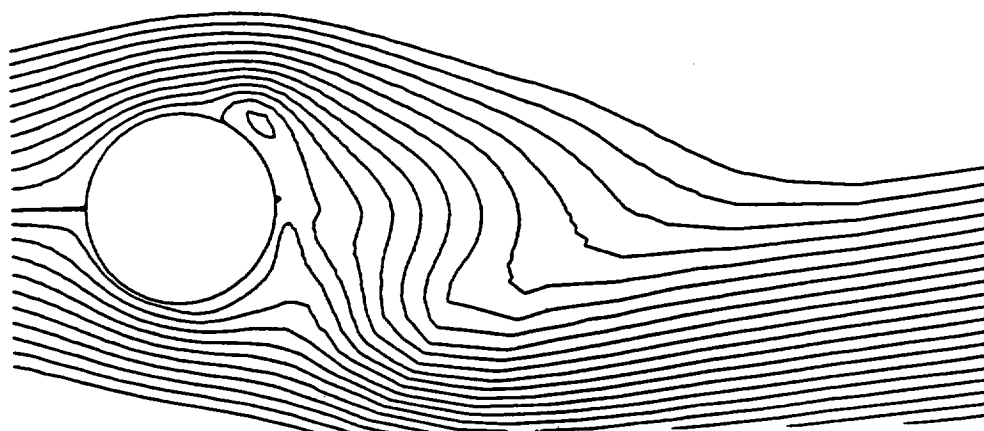


(b) At the middle  $C_L$  point

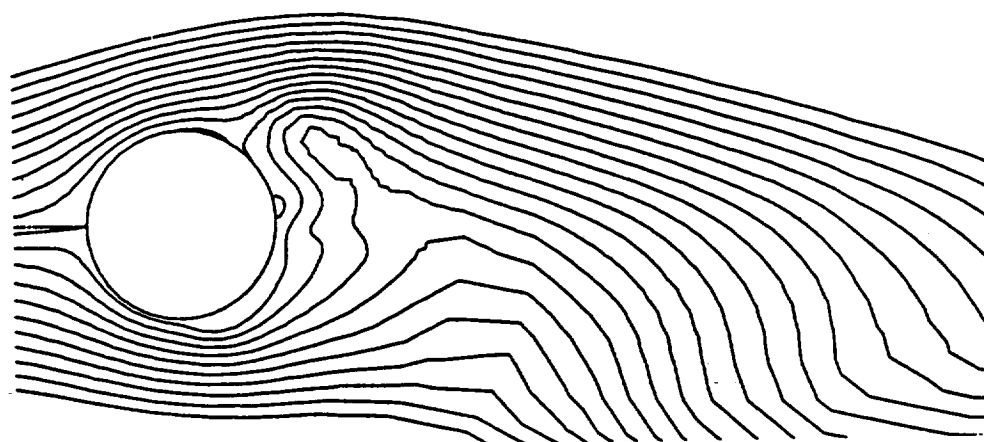


(c) At the minimum  $C_L$  point

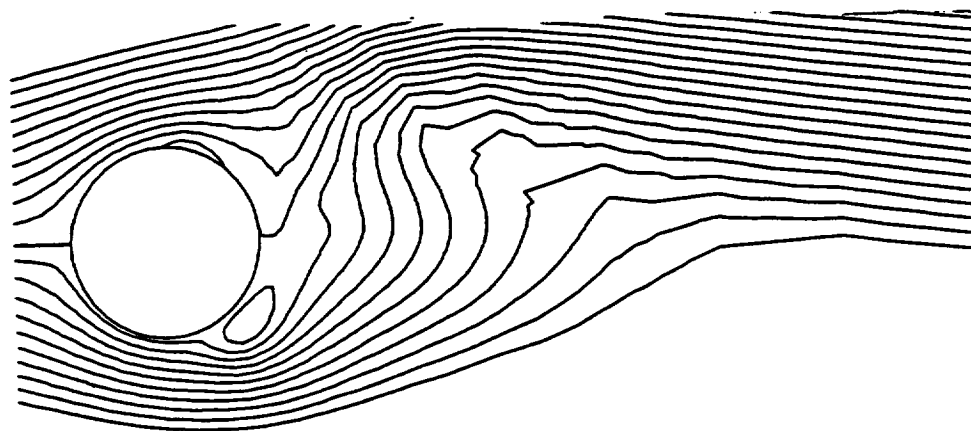
Fig. 6.5 Streamlines for the  $C_\mu=0.004$  case.



(a) At the maximum  $C_L$  point



(b) At the middle  $C_L$  point



(c) At the minimum  $C_L$  point

Fig. 6.6 Streamlines for the  $C_\mu=0.05$  case.

6.5. As  $C_\mu$  increases to 0.02, the flow field becomes asymmetric again and the pattern of the streamlines is similar to the non-jet case. It is noted that when  $C_\mu=0.004$ , the drag is reduced by the jet as shown in Fig. 6.2. Therefore, it is found that when the drag is reduced by the jet, there is also change in the streamline pattern.

#### 6.1.4 Velocity Vectors

The velocity vectors are presented in Figs. 6.7 - 6.10. It is noted that two counter rotating vortices appear for the  $C_\mu=0.004$  case which correspond to the symmetric streamlines pattern as shown in Figs 6.5. The distributions of the velocity vectors show consistency with the results obtained from the streamlines. These results are provided here for purely comparative purposes.

### 6.2 Experimental Results

#### 6.2.1 Static Pressure Measurement

Figure 6.11 shows pressure distributions along the 3"-diameter cylinder. There is no significant change with respect to the Reynolds number in the range investigated. These data are in very good agreement with the other measurements[2]. The data near  $270^\circ$  should not be taken as true results due to the mechanical failure of the system.

Figures 6.12 show the effect of the jet momentum on the pressure distribution for several Reynolds numbers, namely  $Re=1\times 10^5$ ,  $1.5\times 10^5$ ,  $1.8\times 10^5$ ,  $2.2\times 10^5$ ,  $2.5\times 10^5$  and  $3\times 10^5$ . It is seen that the effect of the jet mainly appears from  $\theta = 60^\circ$  to  $\theta = 300^\circ$ . These two points are roughly correspond to the minimum  $C_p$  point. The jet does not have significant influence in the front part of the cylinder. As the Reynolds number increased, less effect by the jet can be seen on the pressure distribution. For  $Re=2.5\times 10^5$  and  $3\times 10^5$  cases, there are no significant changes due to the jet in the pressure distribution.

Figure 6.13 shows the variation of the drag coefficient as a function of the Reynolds number for the non-jet cases. It is seen that the transition occurs at about  $Re=2\times 10^5 \sim 3\times 10^5$  where the slope of the curve changes. This is in good agreement with the results of James et al. [1] and Achenbach [2]. It is noted that there is no significant change due to the end plates. However, the transition occurs slightly earlier for the 4"-diameter cylinder with end plates case than without the end plate case. Figure 5.14 illustrates the effect of the jet on the drag coefficient for several Reynolds numbers tested. The values for  $C_\mu=0.0$  correspond to the non-jet case. In general, as jet-blowing

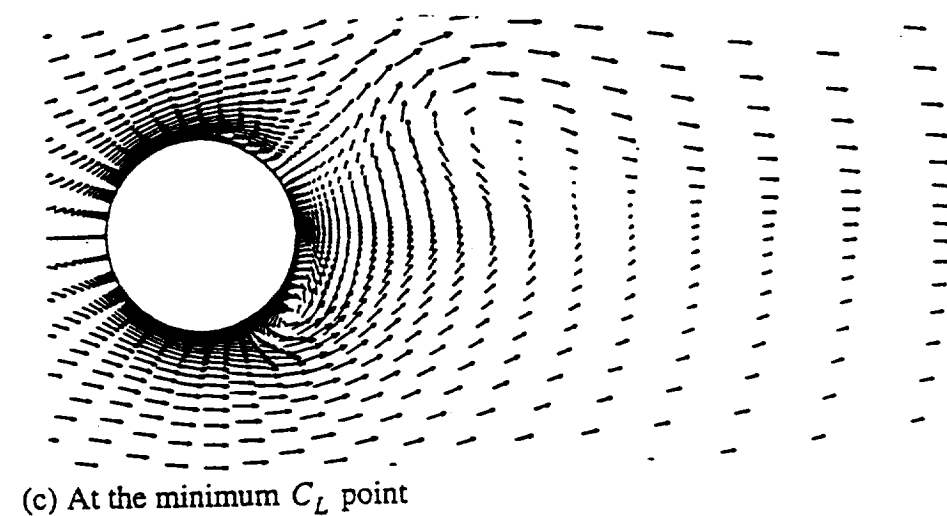
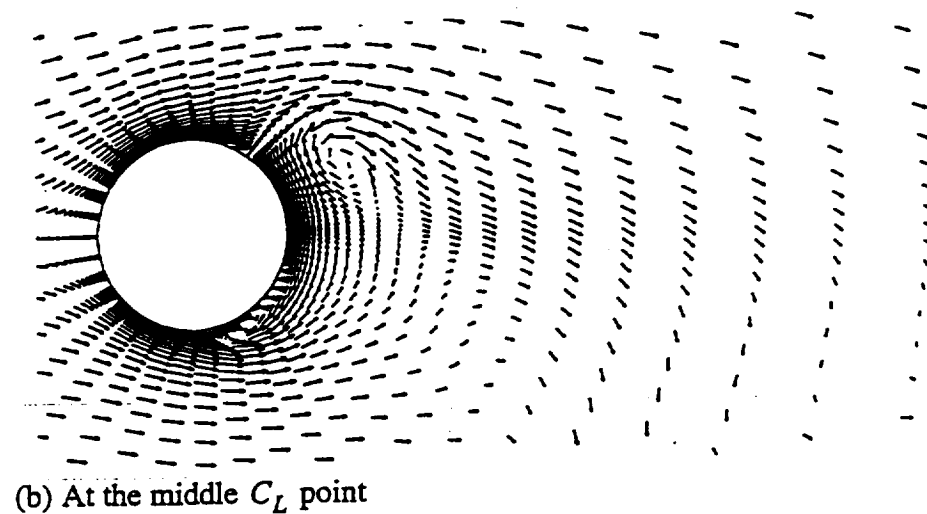
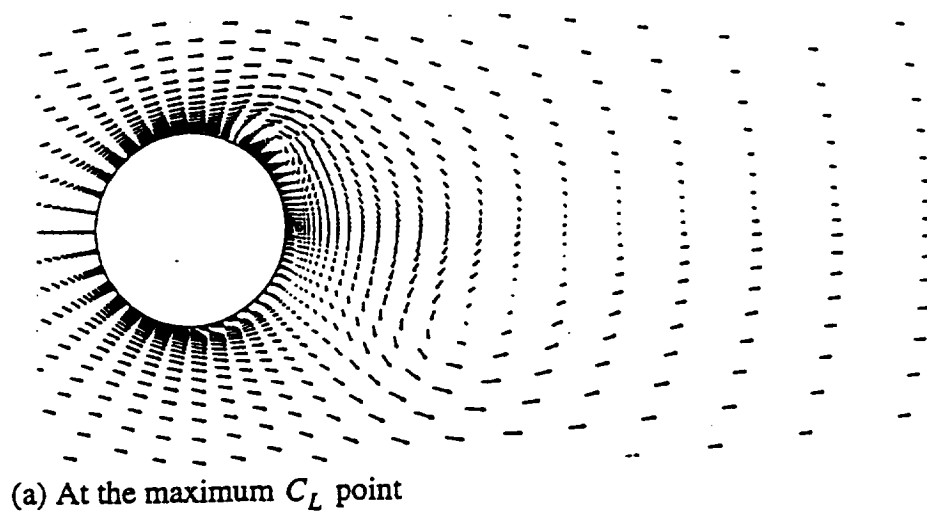
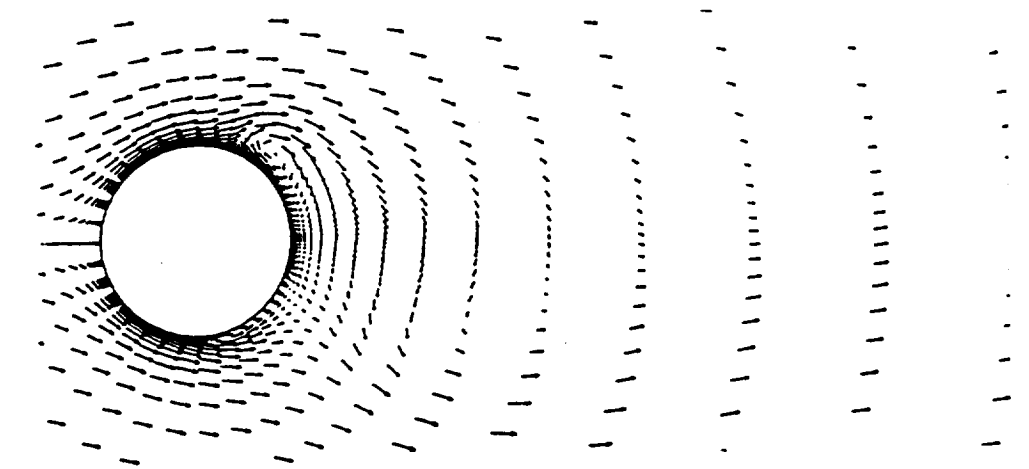
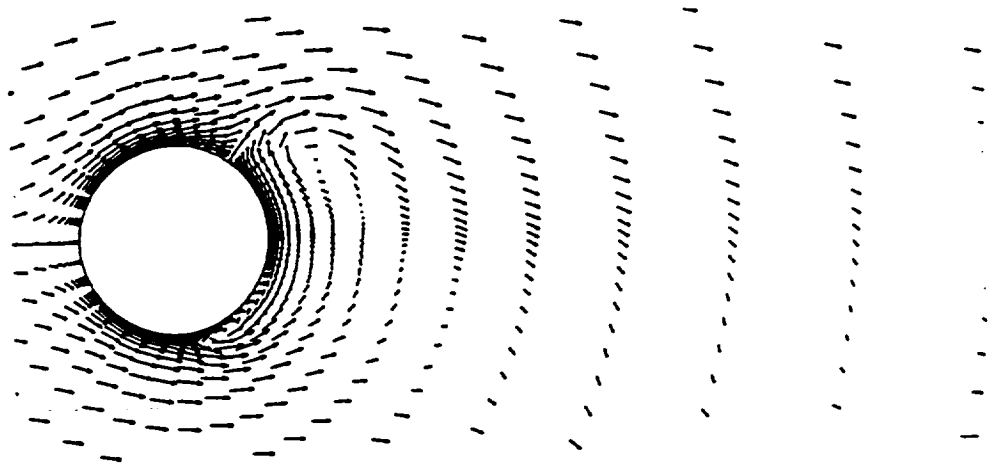


Fig. 6.7 Velocity vectors for no-jet case.

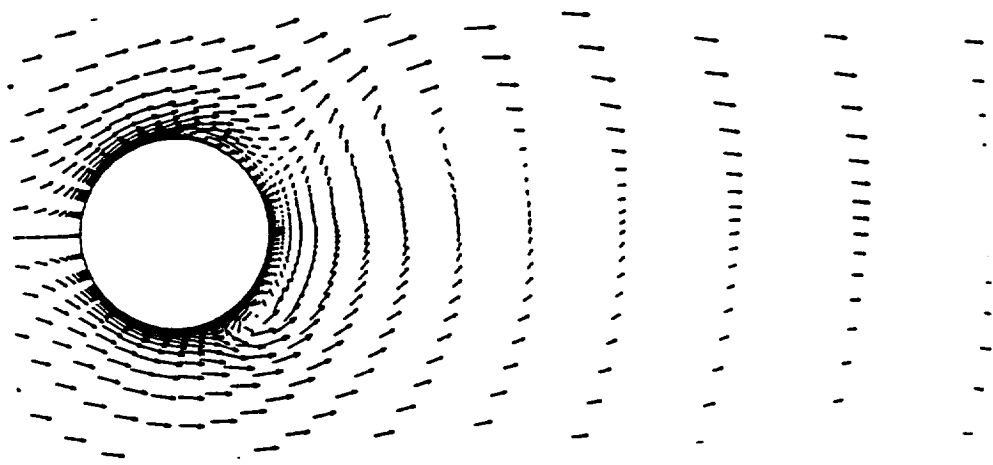




(a) At the maximum  $C_L$  point

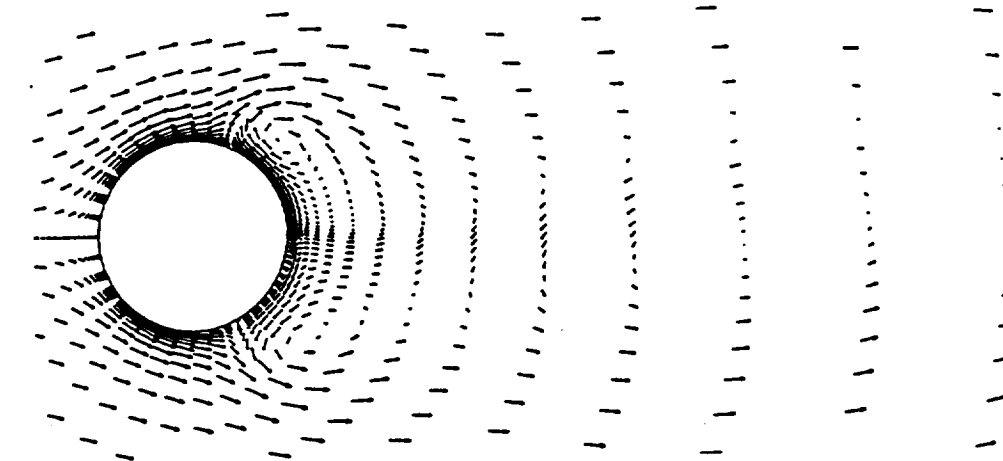


(b) At the middle  $C_L$  point

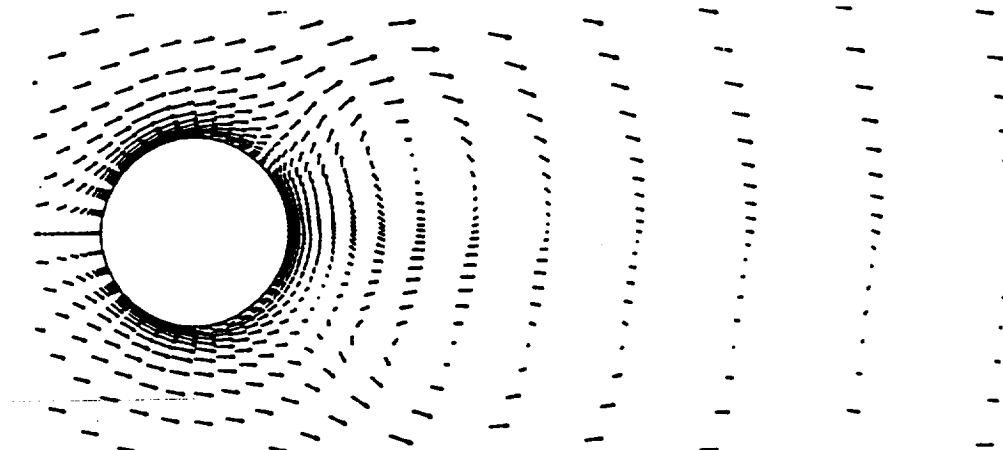


(c) At the minimum  $C_L$  point

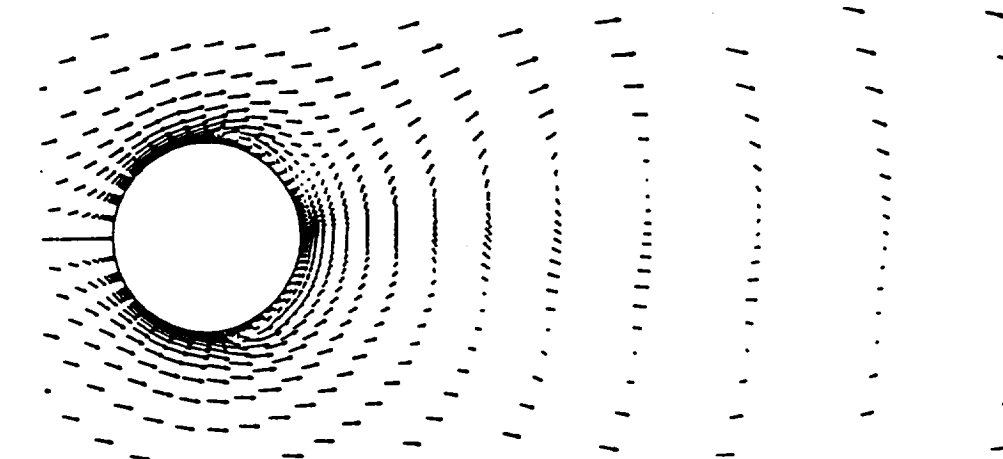
Fig. 6.8 Velocity vectors for the  $C_\mu=0.0005$  case.



(a) At the maximum  $C_L$  point



(b) At the middle  $C_L$  point



(c) At the minimum  $C_L$  point

Fig. 6.9 Velocity vector for the  $C_\mu = 0.004$  case.

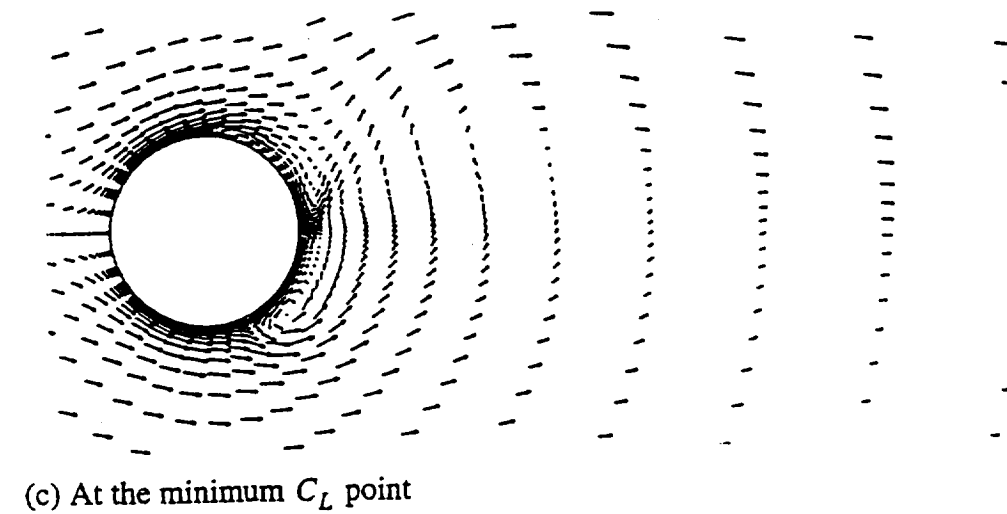
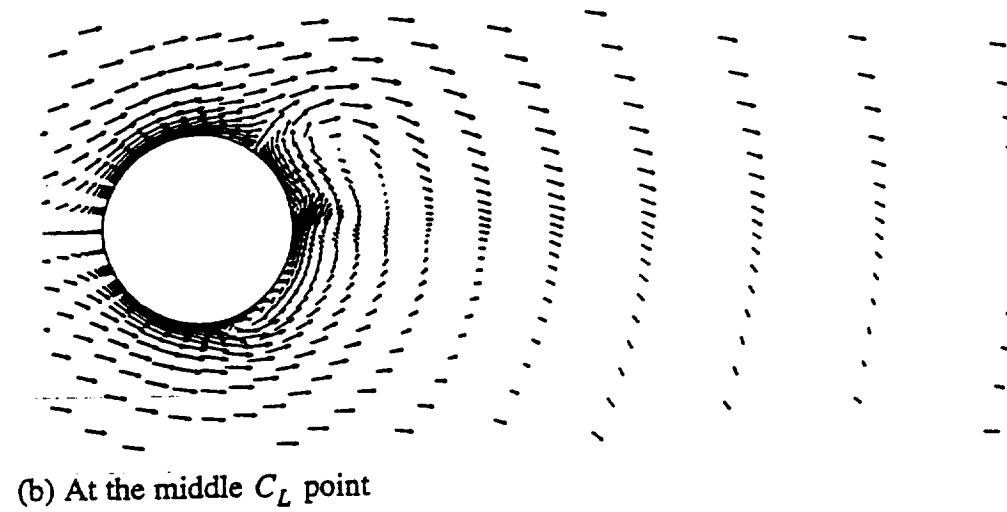
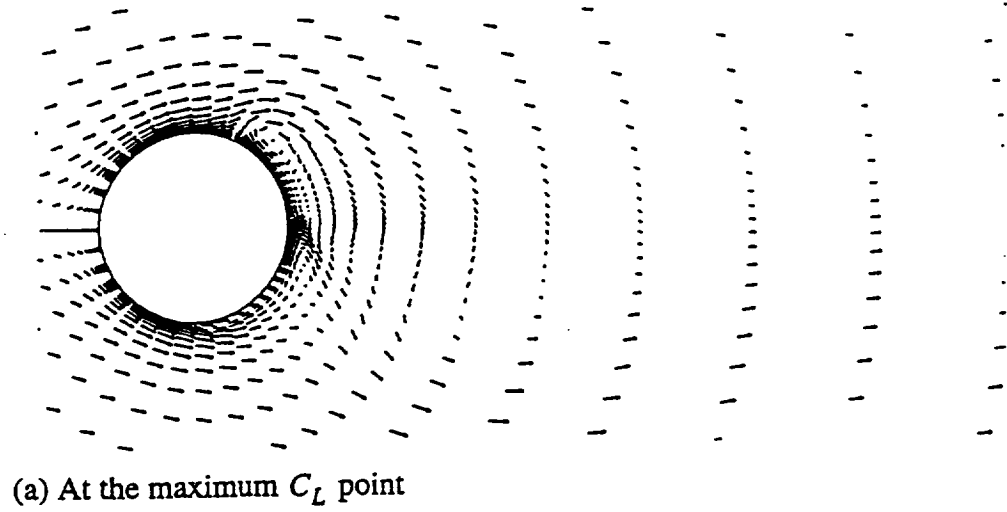


Fig. 6.10 Velocity vector for the  $C_\mu = 0.05$  case.

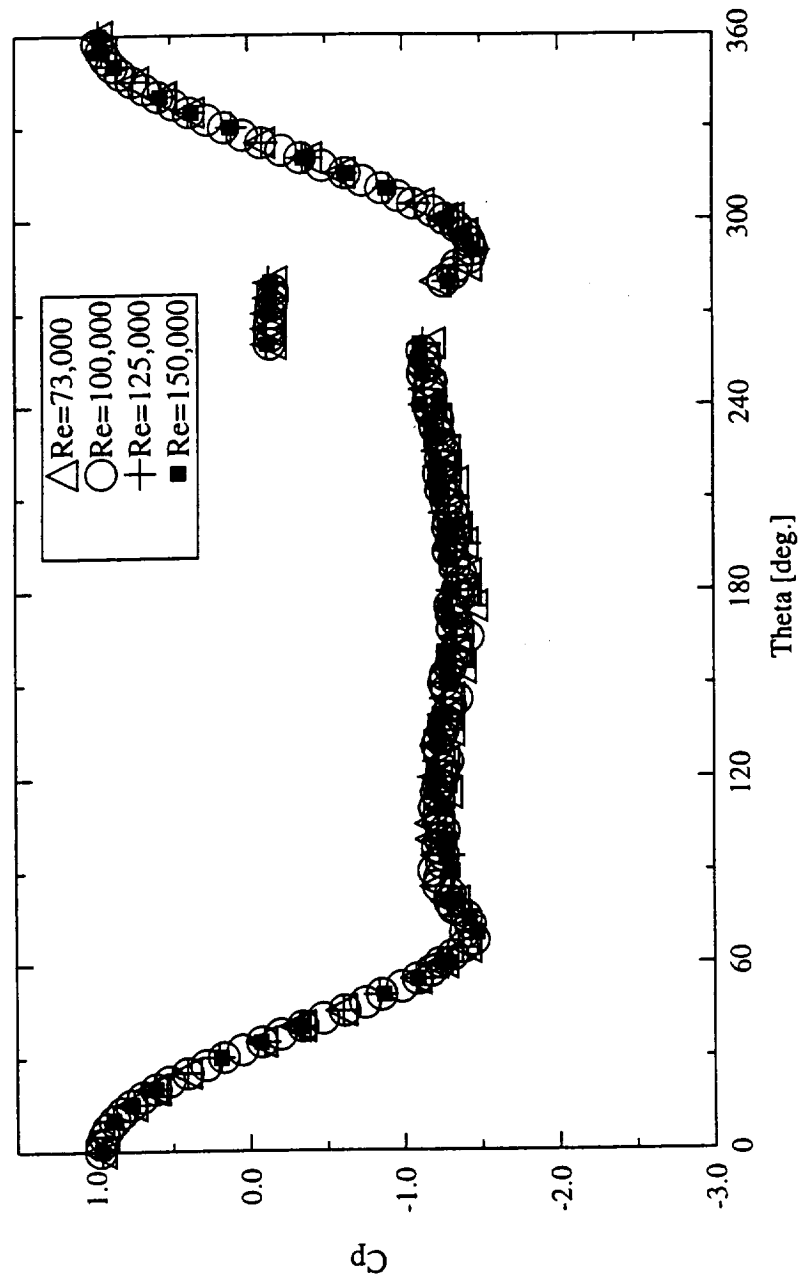
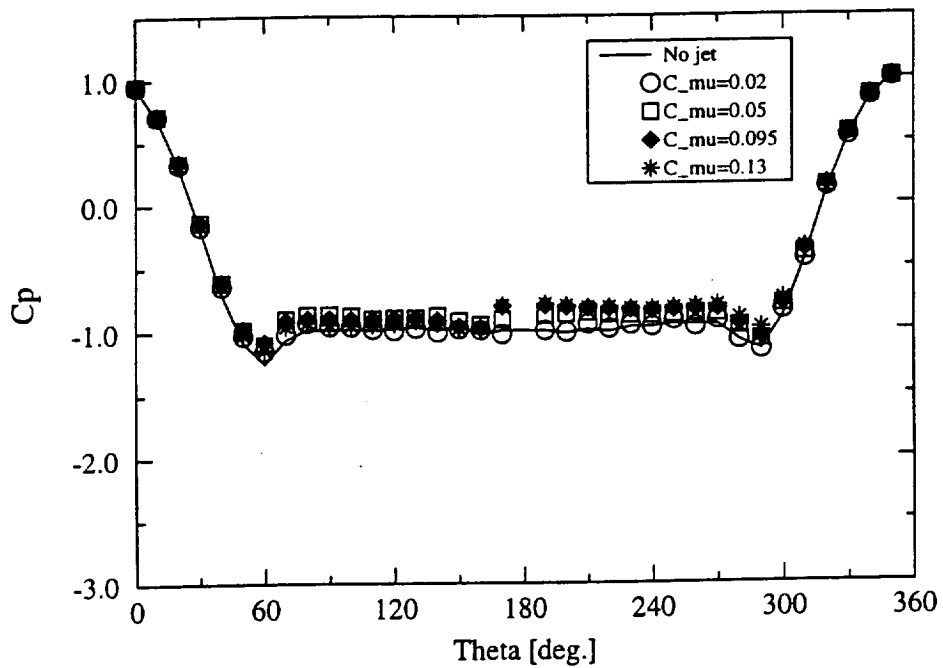
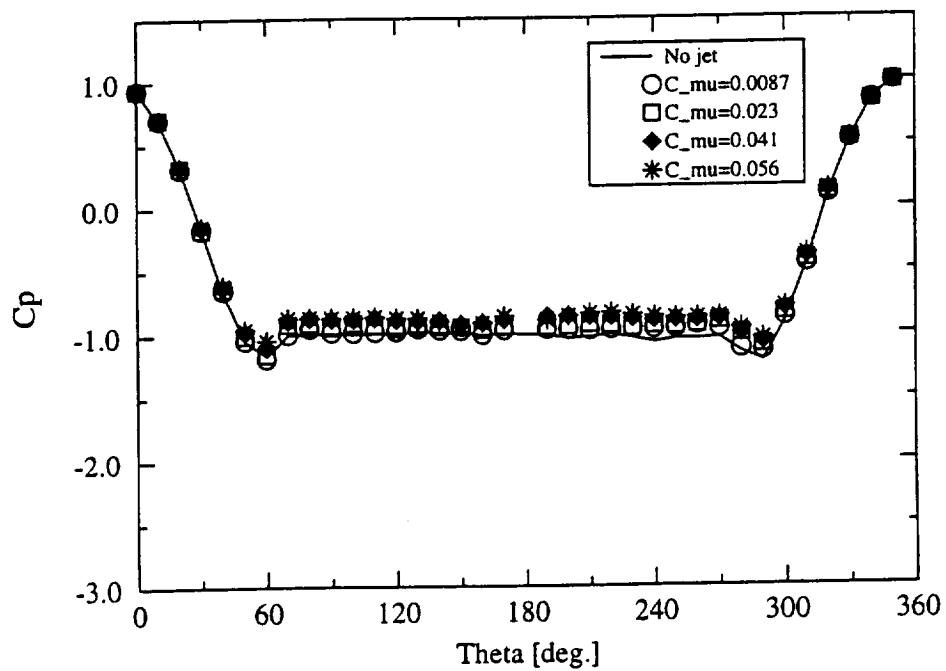


Fig. 6.11 Pressure distributions along 3"-diameter cylinder (model "A").

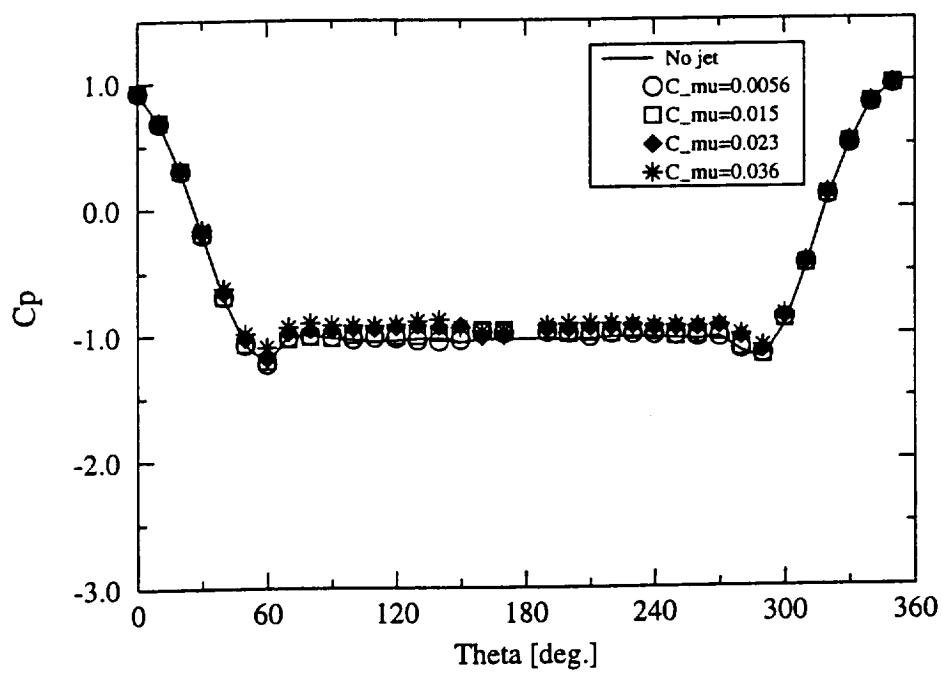


(a)  $Re = 1 \times 10^5$

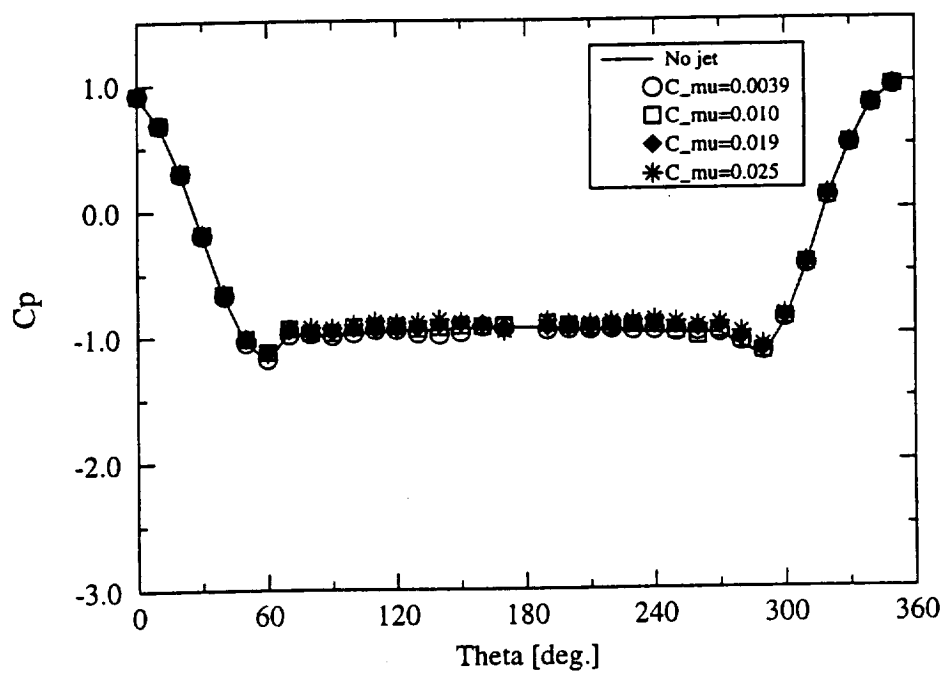


(b)  $Re = 1.5 \times 10^5$

Fig. 6.12 Effect of the jet on pressure distributions.

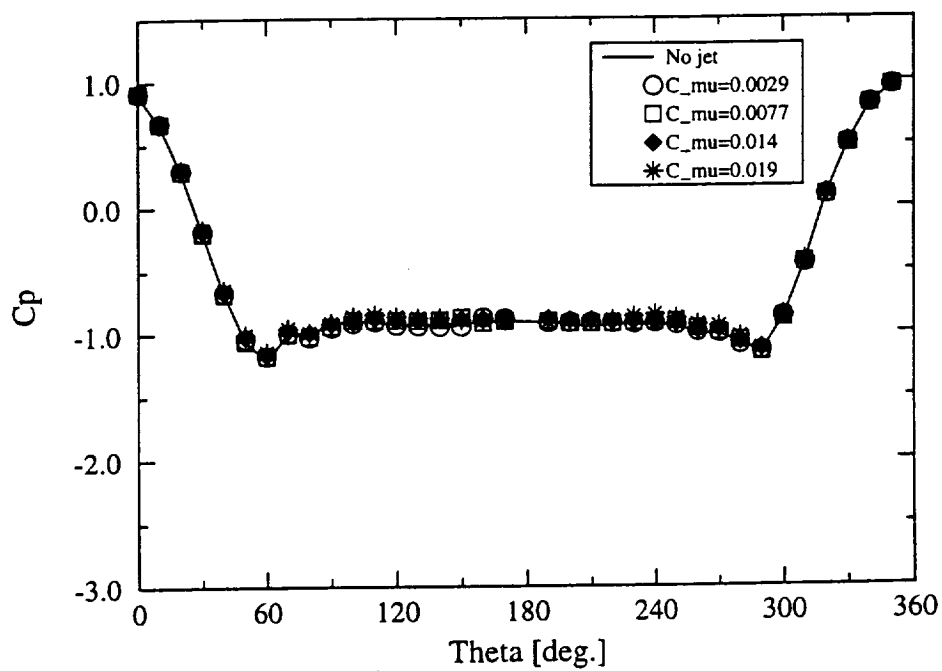


(c)  $Re = 1.8 \times 10^5$

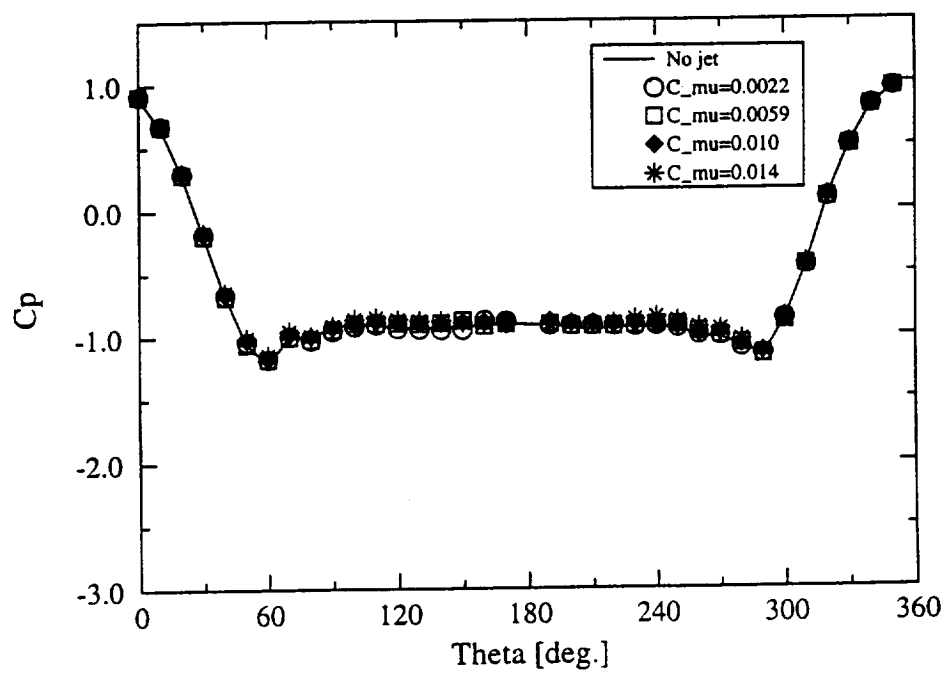


(d)  $Re = 2.2 \times 10^5$

Continued.



(e)  $Re = 2.5 \times 10^5$



(f)  $Re = 3.0 \times 10^5$

Continued.

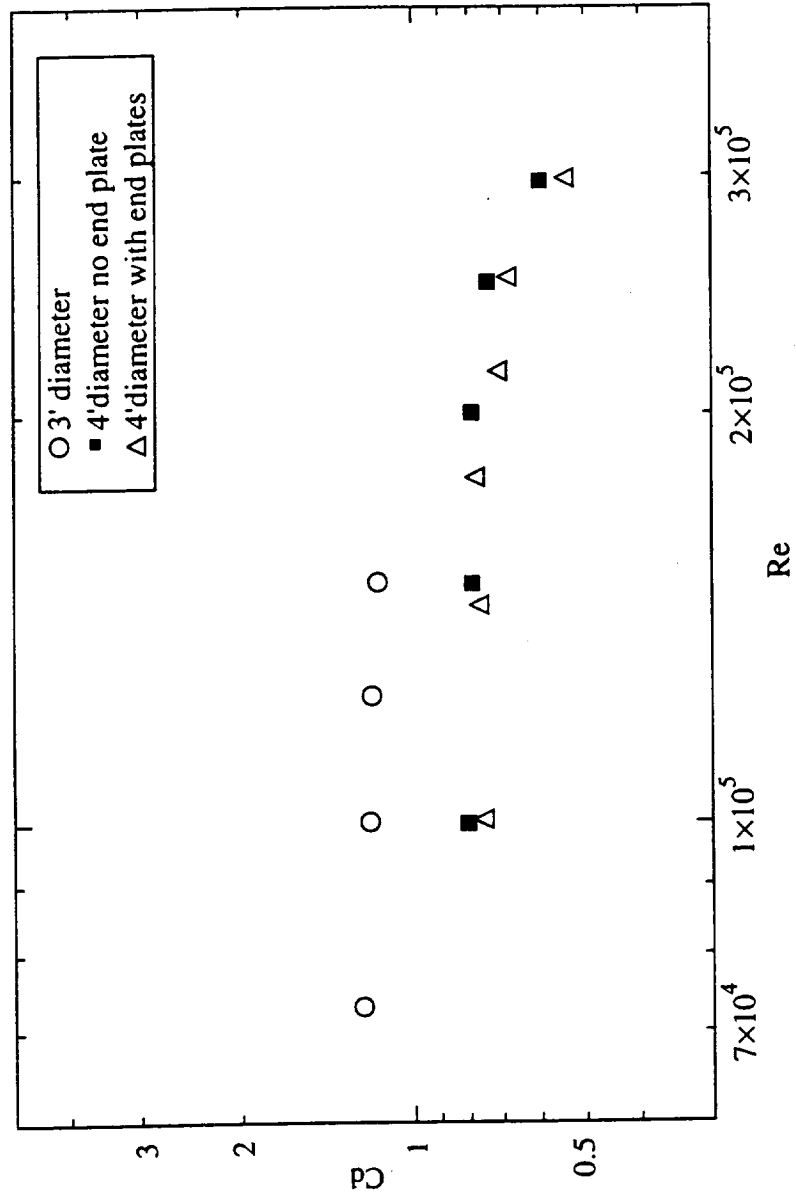


Fig. 6.13 Variation of the drag coefficient with Reynolds number for the non-jet cases.



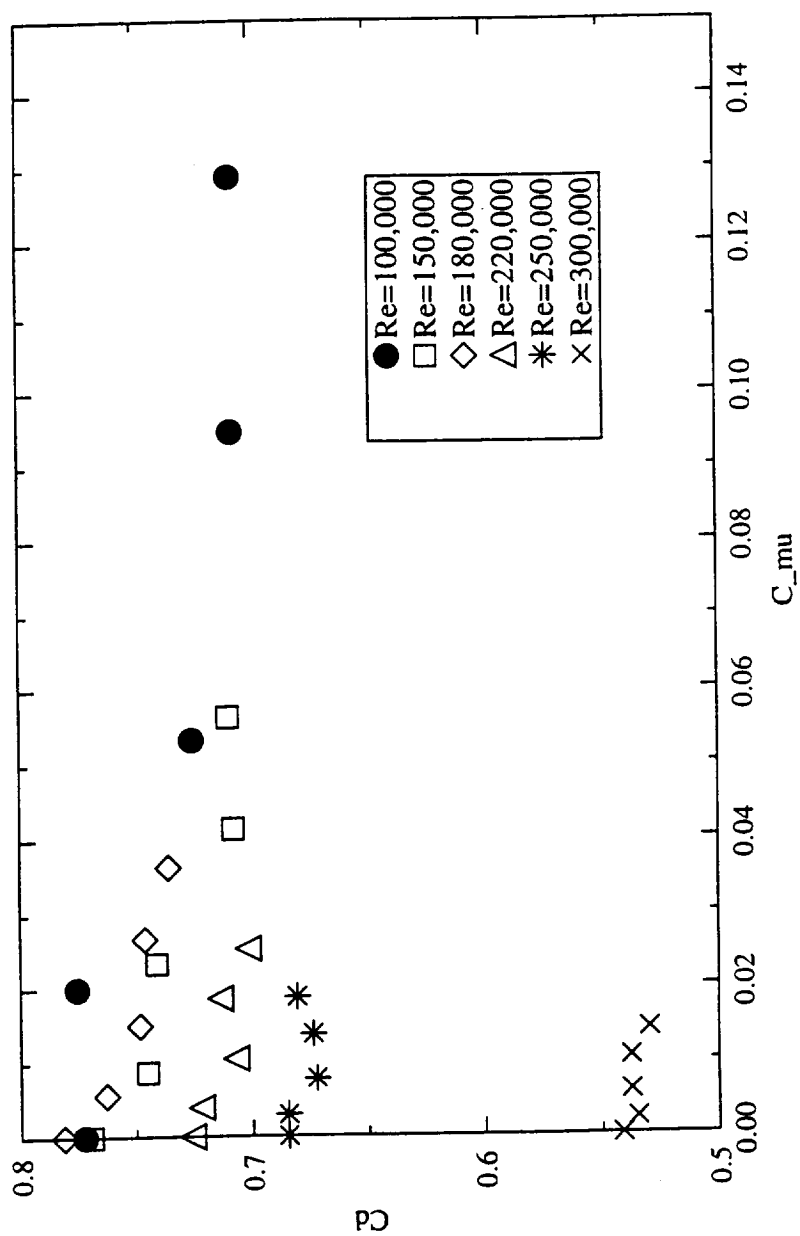


Fig. 6.14 Variations of the drag coefficient with  $C_\mu$  and Reynolds number.

momentum coefficient increases, the drag coefficient reduces; however, beyond certain point the effect is noted to saturate. The higher Reynolds number cases are less affected by the jet injection; however, the amount of jet injected must be increased to obtain the corresponding  $C_\mu$  for these high Reynolds number cases, which was not possible this time due to restriction of the volume flow rate of the jet.

### 6.2.2 Smoke Wire Visualization

Figures 6.15 show the results of the smoke wire visualization. Figures 6.15a, b and c correspond to the no-jet case, the  $C_\mu=0.02$  case and the  $C_\mu=0.13$  case, respectively. Depicted next to the picture are illustrations of the pictures. These visualizations were conducted at the Reynolds number of  $1 \times 10^5$ . Two large alternating eddies can be seen for the no-jet case and the  $C_\mu=0.02$  case. And these two cases show a similar pattern. On the other hand, the corresponding eddies for the  $C_\mu=0.13$  case are seen to be symmetric. More importantly, relatively small perturbations of the smoke can be observed successively at the edges of the smoke behind the cylinder. These perturbations are seen to be symmetric. These relatively symmetric small perturbations cannot be seen for the no-jet case and the  $C_\mu=0.02$  case where no significant drag reduction was observed in the previous section. Therefore one can consider that this discrepancy in the flow structure has a relation to the drag reduction. Since streak lines contain the history of the flow, this fluctuation can be interpreted as a successive fluctuation in the vicinity of the separation points. It is also noted that the size of these fluctuations are smaller than the large eddies which are observed for the no-jet case and the  $C_\mu=0.02$  case.

## 6.3 Selected Comparative Study

### 6.3.1 No-Jet Case

The comparison of the pressure distribution along the cylinder without the jet at  $Re=1 \times 10^5$  for the numerical and experimental results is illustrated in Fig. 6.16. The numerical results of both the unsteady and the steady cases have reasonable agreement with the experimental results. The pressure data from the numerical computation have good agreement especially up to  $\pm 90^\circ$  from the front stagnation. The unsteady calculation represents similar profile around the rear stagnation point, while the steady calculation has discrepancies in this region. However, steady calculation successfully reproduces the pressure distribution profile up to  $\pm 120^\circ$ .

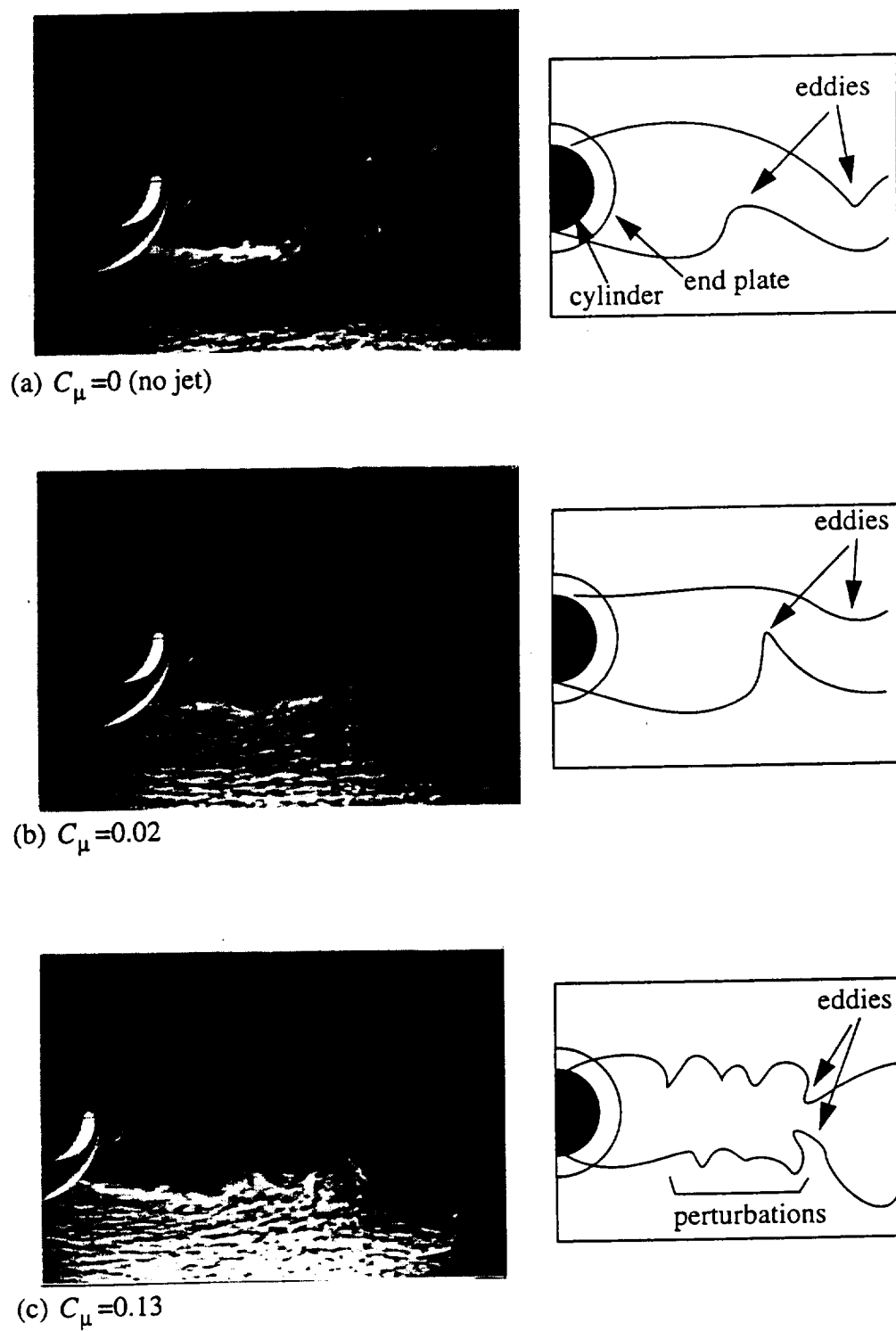


Fig. 6.15 Smoke wire visualization of the flow field behind the cylinder.

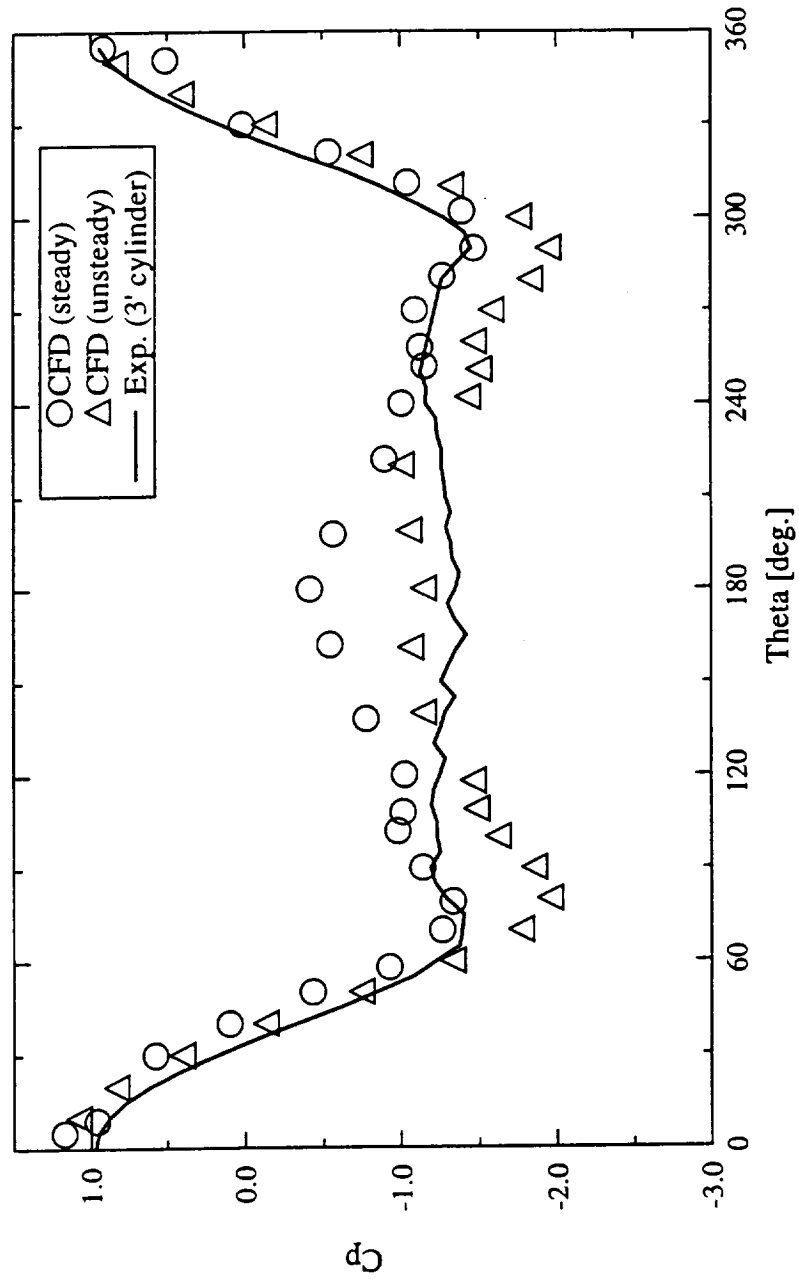


Fig. 6.16 Comparison of pressure distributions from the numerical and experimental results for the non-jet cases.

### 6.3.2 Jet case

The variations of the drag coefficient with respect to the jet-blowing momentum coefficient are plotted in Fig. 6.17. For the  $Re = 1 \times 10^5$  case, the experimental results show that the jet does not have the effect to reduce the drag with  $C_\mu = 0.002$ . When the  $C_\mu$  is increased beyond 0.05 the drag is decreased. On the other hand, the numerical results for the same Reynolds number case shows that there is also a threshold value before which there is no significant change observed. After the threshold value the jet injection works to reduce the drag. However, as  $C_\mu$  increases further, the drag coefficient increase to the level of the non-jet case.

### 6.3.3 Flow Field Pattern

The streak lines are obtained from numerical computations to compare with the results of smoke wire visualization. The streak lines shown in Fig. 6.18a is obtained at the middle point of the lift coefficient for the case when no jet is injected. The results for the  $C_\mu = 0.0005$  case where no significant effect to reduce the drag is noted are depicted in Fig. 6.18b. The streak lines shown in Fig. 6.18c are the results for the  $C_\mu = 0.0041$  case where the drag is reduced by injecting the jet. It is clearly seen that the streak lines are more symmetric behind the cylinder for the case when the drag is reduced (Fig. 6.18a) than ones with no drag reduction (Figs. 6.18b and c). This flow field pattern matches with the result obtained by the smoke wire visualization. Therefore, it is demonstrated that the large flow structure is also influenced by the jet injected from the rear stagnation when the drag reduction is observed.

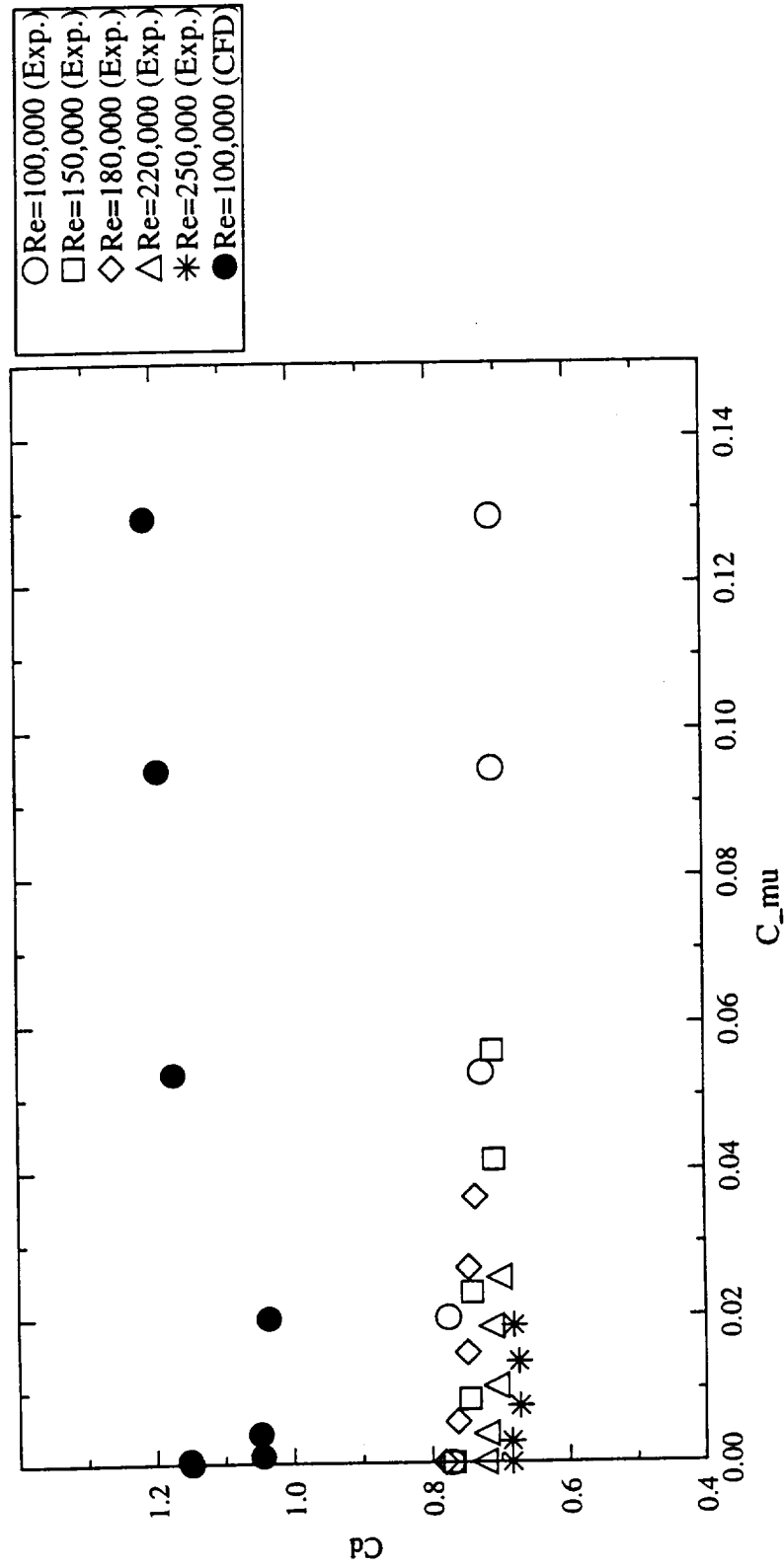
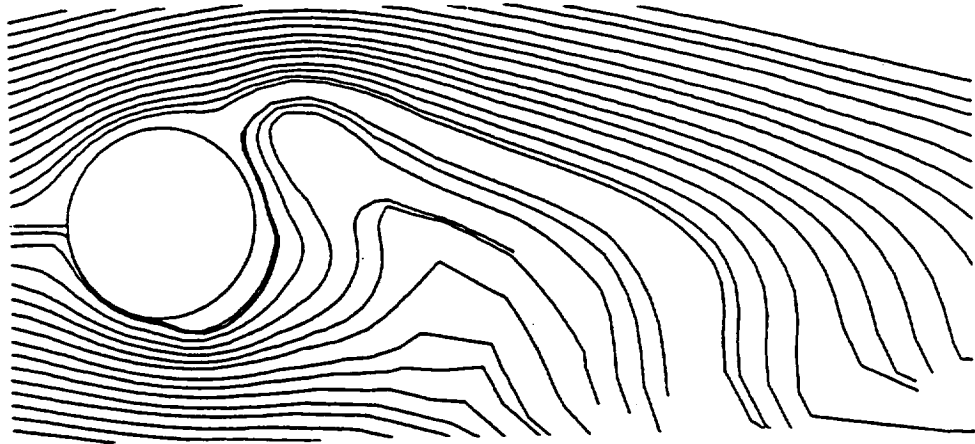
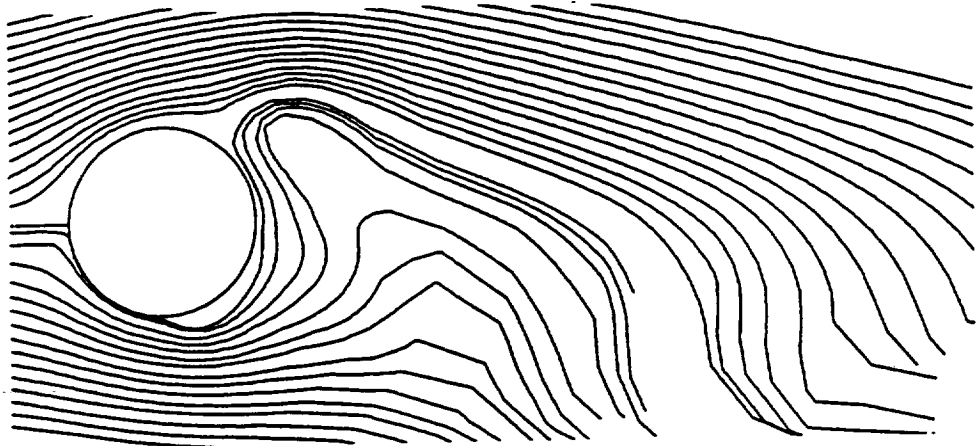


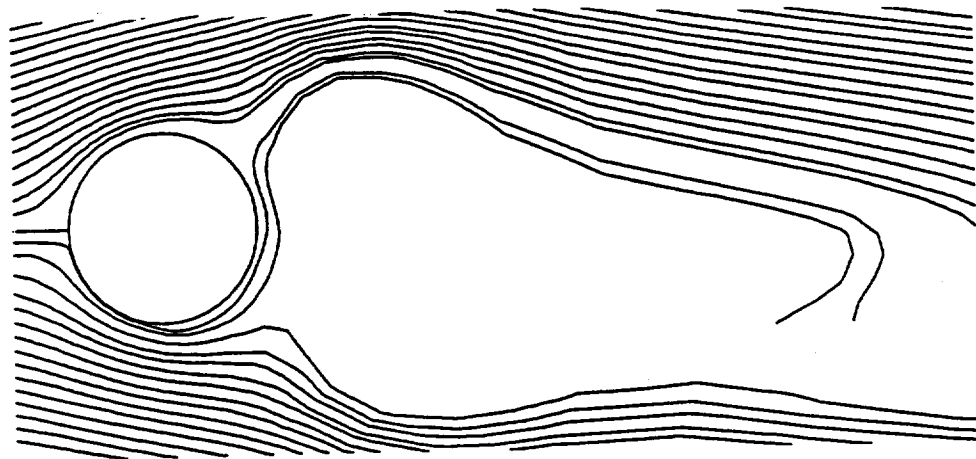
Fig. 6.17 Comparison of the variations of the drag coefficient from the numerical and experimental results.



(a)  $C_\mu = 0$  (no jet)



(b)  $C_\mu = 0.0005$



(c)  $C_\mu = 0.004$

Fig. 6.18 Streak lines from the numerical results.

## Chapter VII

### CONCLUSIONS AND RECOMMENDATIONS

The phenomenon of drag reduction on a two-dimensional circular cylinder was investigated by ejecting jet from the rear stagnation region. The validity of a commercial computational fluid dynamics code (Fluent) for the cylinder was investigated at Reynolds number of  $1 \times 10^5$ . Two grid topologies, namely a rectangular grid with a blocked region and O-grid with a branch cut, were initially proposed. After a sensitivity study, the O-grid topology was selected based on the fluid dynamical and economical analysis. Relatively more grid points were placed in the region where steep gradient of the dependent variable is expected as well as in the region where the aspect ratio of the cell was not adequate.

With the improved O-grid system around the cylinder, fluid dynamical events for the cylinder were successfully reproduced and the results were compared with other available results in the literature with respect to the pressure distribution along the cylinder wall, the drag and the lift coefficients and the Strouhal number. The sensitivity analyses were conducted for a wide range of computational aspects such as Reynolds number, steady and unsteady calculation, grid dependency and the effect of computational area.

Next, the flow phenomena around the cylinder with jet were investigated. The pressure distributions, stream functions and velocity vectors were presented for several jet momentum coefficient cases. It was found that the drag is decreased by a certain amount of jet injected into the flow from the cylinder. In this case, the pressures in the rear portion of the cylinder are mainly affected. Furthermore, when the drag is decreased by the jet, a pair of counter rotating vortices can be seen behind the cylinder and flow pattern becomes more symmetric with respect to the flow direction.

Finally, experimental investigations were conducted to understand the flow behavior. Static pressure along the cylinder was measured to obtain the pressure distribution as well as the drag, while smoke wire visualization technique was used to understand simultaneous flow field structure behind the cylinder. It is found that the profile of the pressure distribution is not significantly affected by the jet. However, the pressures



beyond its minimum point on the surface, which is approximately  $\pm 60^\circ$  from the front stagnation point, are raised uniformly when the drag reduction is observed. It is found that the effectiveness of the jet on the drag reduction varies with the amount of jet ejected as well as Reynolds number. The smoke wire visualization revealed that there are also discrepancies in the characteristic of the flow behind the cylinder when the drag is reduced by the jet: the flow structure becomes rather symmetric and smaller fluctuations are seen along the separated streak lines.

The numerical results were compared with the experimental results; and the following conclusions can be made. The drag of a circular cylinder can be reduced by injecting jet with a certain amount of strength from the rear stagnation point. The injection of jet changes pressure distribution along the cylinder, especially in the rear portion of the cylinder. When the drag reduction is achieved, the flow behind the cylinder becomes rather symmetric.

This study has been conducted mainly based on the steady state assumption; however, investigating this problem as a time dependent problem is highly recommended since the flow is essentially unsteady. Furthermore, the Strouhal number and the magnitude of the lift and/or drag are expected to change by the jet based on the observations of this study.

No turbulent model for the numerical calculation has been used in the present study. Employing a turbulent model may still not be necessary in this problem set up. Also, using a turbulent model causes another problem, particularly in this code; the code automatically assumes the turbulent velocity profile near wall without knowing whether there is turbulent flow in the region or not. It is also recommended to pay more attention to three-dimensionality of this problem. This issue is deeply related to the turbulence. It is suggested that the three-dimensional computation is essential to reproduce physical phenomena exactly.

Also, investigation regarding the discrepancy on the drag coefficient between two different diameter tunnel models is needed. A more detailed information about the flow near the rear stagnation region can be obtained by inserting a smoke wire behind the cylinder. Increasing the amount of the jet is also suggested.

## REFERENCES

1. James, W. D., Paris, S. W., and Malcolm, G. N., "A Study of Viscous Cross-Flow Effects on Circular Cylinders at High Reynolds Numbers," AIAA Paper 79-1477, July 1979.
2. Achenbach, E., "Distribution of Local Pressure and Skin Friction Around a Circular Cylinder in Cross-Flow up to  $Re = 5 \times 10^6$ ," *Journal of Fluid Mechanics*, Vol. 34, Part 4, December 1968, pp. 625-639.
3. Humphreys, J. S., "On a Circular Cylinder in a Steady Wind at Transition Reynolds Numbers," *Journal of Fluid Mechanics*, Vol. 9, Part 4, December 1960, pp. 603-612.
4. Cantwell, B. and Coles, D., "An Experimental Study of Entrainment and Transport in the Turbulent Near Wake of a Circular Cylinder," *Journal of Fluid Mechanics*, Vol. 136, November 1983, pp. 321-374.
5. Kwak, D., Chang, J. L. C., Shanks, S. P. and Chakravarthy, S. R., "A Three-Dimensional Incompressible Navier-Stokes Flow Solver Using Primitive Variables," *AIAA Journal*, Vol. 24, No. 3, March 1986, pp. 390-396.
6. Rogers, S. E. and Kwak, D., "Upwind Differencing Scheme for the Time-Accurate Incompressible Navier-Stokes Equation," *AIAA Journal*, Vol. 28, No. 2, February 1990, pp. 253-262.
7. Sarpkaya, T. and Schoaff, R. L., "Inviscid Model of Two-Dimensional Vortex Shedding by a Circular Cylinder," *AIAA Journal*, Vol. 17, No. 11, November 1979, pp. 1193-1200.
8. Thoman, D. C. and Szewczyk, A. A., "Time-Dependent Viscous Flow Over a Circular Cylinder," *The Physics of Fluids Supplement II*, January 1969, pp. 76-85.
9. Ishii, K., Kuwahara, K., Ogawa, S., Chyu, W. J. and Kawamura, T., "Computation of Flow Around a Circular Cylinder in a Supercritical Regime," AIAA Paper 85-1660, July 1985.
10. Hirsh, C., *Numerical Computation of Internal and External Flows*, Wiley, New York, 1990.

11. Wei, T. and Smith, C. R., "Secondary Vortices in the Wake of Circular Cylinder," *Journal of Fluid Mechanics*, Vol. 169, August 1986, pp. 513-532.
12. Hansen, M. O. L., Sorensen, J. N. and Barker, V. A., "A Numerical Investigation of 3-D Flow Past an Infinite Cylinder," *Computational Fluid Dynamics '92*, Vol. 1, April 1992, pp. 375-381.
13. Beaudan, P. and Moin, P., "Numerical Experiments on the Flow Past a Circular Cylinder at Sub-Critical Reynolds Number," Thermo Science Division, Department of Mechanical Engineering, Stanford University, Report No. TF-62, Stanford, CA, December 1994.
14. Roshko, A., "Experiments on the Flow Past a Circular Cylinder at Very High Reynolds Number," *Journal of Fluid Mechanics*, Vol. 10, Part 3, May 1983, pp. 345-356.
15. Apelt, C. J., West, G. S. and Szewczyk A. A., "The Effects of Wake Splitter Plates on the Flow Past a Circular Cylinder in the Range  $10^4 < R < 5 \times 10^4$ ," *Journal of Fluid Mechanics*, Vol. 61, Part 1, October 1973, pp. 187-198.
16. Bearman, P. W., "Investigation of the Flow Behind a Two-Dimensional Model with a Blunt Trailing Edge and Fitted with Splitter Plates," *Journal of Fluid Mechanics*, Vol. 21, Part 2, February 1965, pp. 241-255.
17. Cete, A. R. and Unal, M. F., "Effects of Splitter Plate on Wake Formation from a Circular Cylinder: A Discrete Vortex Simulation," *Computational Fluid Dynamics '92*, Vol. 1, April 1992, pp. 349-356.
18. Shrader, B. and Duke, M. R., "An Experimental Investigation on the Control of Separated Flow over Cylinders by Means of a Rear Stagnation Jet," AIAA Paper 92-4037, July 1992.
19. Mo, J. D. and Duke, M. R., "An Investigation on the Effects of a Rear Stagnation Jet on the Wake Behind a Cylinder," AIAA Paper 93-3274, July 1993.
20. Dunham, J., "A Theory of Circulation Control by Slot-Blowing, Applied to a Circular Cylinder," *Journal of Fluid Mechanics*, Vol. 33, Part 3 September, 1968, pp. 495-514.
21. Kind, R. J. and Maull, D. J., "An Experimental Investigation of a Low-Speed Circulation-Controlled Airfoil," *The Aeronautical Quarterly*, May 1968, pp. 170-182.

22. Kind, R. J., "A Calculation Method for Circulation Control by Tangential Blowing Around a Bluff Trailing Edge," *The Aeronautical Quarterly*, August 1968, pp. 205-223.
23. Ghee, T. A. and Leishman, J. G., "Unsteady Circulation Control Aerodynamics of a Circular Cylinder with Periodic Jet Blowing," AIAA Paper 91-0433, January 1991.
24. Schlichting, H., *Boundary-Layer Theory*, McGraw-Hill, New York, 1979.
25. Bruun, H. H. and Davies, P. O. A. L., "An Experimental Investigation of the Unsteady Pressure Forces on a Circular Cylinder in a Turbulent Cross Flow," *Journal of Sound and Vibration*, Vol. 40, No. 4, June 1975, pp. 535-559.
26. Kamiya, S., Suzuki, S. and Nishi, T., "On the Aerodynamic Force Acting on a Circular Cylinder in the Critical Range of the Reynolds Number," AIAA Paper 79-1475, July 1979.
27. Przekwas, A. J., Singhal, A. K. and Tam, L. T., "Rocket Injector Anomalies Study, Volume 1: Description of the Mathematical Model and Solution Procedure," NASA CR-174702, Cleveland, OH, July 1984.
28. Fluent Inc., *Fluent Code V. 4.2 User Manual*, Fluent Inc., Lebanon, NH, 1992.
29. Patankar, S. V. and Spalding, D. B., "A Calculation Procedure for Heat, Mass and Momentum Transfer in Three-Dimensional Parabolic Flow," *International Journal of Heat and Mass Transfer*, Vol. 15, No. 10, October 1972, pp. 1787-1806.
30. Leonard, B., "A Stable and Accurate Convective Modeling Procedure Based on Quadratic Upstream Interpolation," *Computer Method in Applied Mechanics and Engineering*, Vol. 19, 1979, pp. 59-98.
31. Britcher, C. P., "Calibration Activities at the Old Dominion University 3 by 4 foot Low Speed Wind Tunnel", Old Dominion University, Norfolk, VA, December 1996.
32. Pressure Systems, Inc., "System 9000 Users Manual", 2nd ed., Pressure Systems, Inc., Hampton, VA, April 1994.
33. Wieselsberger, C., "Neuere Feststellungen uber die Gesetze des Flussigkeits und Luftwiderstands," *Physikalische Zeitschrift*, Vol 22, January 1921, pp. 321-328.
34. Fletcher, C. A. J., *Computational Techniques for Fluid Dynamics*, 2nd ed., Vol. 2, Springer-Verlag, Berlin, 1991.

35. Kovasznay, L. S. G., "Hot-wire investigation of the wake behind cylinders at low Reynolds numbers," *Proceedings of the Royal Society of London, Series A*, Vol. 198, No. 1053, August 1949, pp. 174-190.

## APPENDIX

## APPENDIX A

### REFLAN3D

Detailed theoretical formulations used in REFLAN3D code are presented in this appendix.

#### A.1 Governing Equations

The governing equations used in REFLAN3D is expressed in three-dimensional, cylindrical polar coordinates  $x$ - $r$ - $\theta$ . In the same fashion as described in Chap. 3, all the governing equations can be presented in the general form as

$$\begin{aligned} & \frac{\partial}{\partial x}(\beta u \phi) + \frac{1}{r} \frac{\partial}{\partial r}(r \beta v \phi) + \frac{1}{r} \frac{\partial}{\partial \theta}(\beta w \phi) \\ & - \frac{\partial}{\partial x} \left( \Gamma_{\phi} \frac{\partial \phi}{\partial x} \right) - \frac{1}{r} \frac{\partial}{\partial r} \left( r \Gamma_{\phi} \frac{\partial \phi}{\partial r} \right) - \frac{1}{r} \frac{\partial}{\partial \theta} \left( \frac{1}{r} \Gamma_{\phi} \frac{\partial \phi}{\partial \theta} \right) = S_{\phi} \end{aligned} \quad (\text{A.1})$$

where  $u$ ,  $v$  and  $w$  are velocity components in the  $x$ ,  $r$  and  $\theta$  directions, respectively, while  $\phi$ ,  $\beta_{\phi}$  and  $\Gamma_{\phi}$  are listed in the Table A.1. Equation (A.1) can be applied to the Cartesian coordinates by setting  $r \rightarrow \infty$ ,  $\partial r \equiv \partial y$  and  $r \partial \theta \equiv \partial z$ .

Unlike Fluent described in Chap. 5, REFLAN3D employs the staggered grid practice to improve “checker board” oscillation, where velocities are computed at the cell faces while the other dependent variables are calculated at the cell center. Moreover, in this code “backward boomerang” arrangement is used to assign the nodal point. These features are illustrated in Fig. A.1.

To present integration over the control volume,  $x$ -dimensional case is discussed here.

At the west and east faces, convective fluxes  $C_w^x$  and  $C_e^x$  defined as

$$C_w^x = (\rho u A)_w \quad (\text{A.2a})$$

Table A.1 Conservation terms corresponding to Eq. (A.1)

Equation	$\phi$	$\beta_\phi$	$\Gamma_\phi$	$S_\phi$
mass	1	$\rho$	0	0
axial x-momentum	$u$	$\rho$	$\mu$	$-\frac{\partial p}{\partial x} + \frac{\partial}{\partial x} \left( \mu \frac{\partial u}{\partial x} \right) + \frac{1}{r} \frac{\partial}{\partial r} \left( r \mu \frac{\partial u}{\partial r} \right) + \frac{1}{r^2} \frac{\partial}{\partial \theta} \left[ \mu \frac{\partial}{\partial \theta} (r w) \right]$ $-\rho g_x - \frac{2}{3} \frac{\partial}{\partial x} (\mu_{eff} \nabla \bullet U + \rho k)$
radial r-momentum	$v$	$\rho$	$\mu$	$-\frac{\partial p}{\partial r} + \frac{\partial}{\partial x} \left( \mu \frac{\partial u}{\partial r} \right) + \frac{1}{r} \frac{\partial}{\partial r} \left( r \mu \frac{\partial v}{\partial r} \right) + \frac{1}{r^2} \frac{\partial}{\partial \theta} \left[ \mu \frac{\partial}{\partial r} (r w) \right]$ $-\frac{2}{r} \frac{\partial}{\partial \theta} (\mu r w) - \frac{2\mu}{r^3} \frac{\partial}{\partial \theta} (r w) + \frac{\rho w^2}{r} - \frac{2\mu}{r^2} \nu$ $-\rho g_y - \frac{2}{3} \frac{\partial}{\partial r} (\mu_{eff} \nabla \bullet U + \rho k)$
circumferential $\theta$ -momentum	$rw$	$\rho$	$\mu$	$-\frac{\partial p}{\partial \theta} + \frac{\partial}{\partial x} \left( \mu \frac{\partial u}{\partial \theta} \right) + \frac{\partial}{\partial r} \left( \mu \frac{\partial v}{\partial \theta} \right) + \frac{1}{r^2} \frac{\partial}{\partial \theta} \left[ \mu \frac{\partial}{\partial \theta} (r w) \right]$ $+ \frac{2}{r} \frac{\partial}{\partial \theta} (\mu v) + \frac{\mu \partial v}{r \partial \theta} - \frac{2}{r} \frac{\partial}{\partial \theta} (\mu r w)$ $-\rho g_y - \frac{2}{3} \frac{\partial}{\partial r} (\mu_{eff} \nabla \bullet U + \rho k)$





$$C_e^x = (\rho u A)_e \quad (\text{A.2b})$$

where  $\rho$  is an upwind density, if the flow is variable density flow, defined as

$$\rho_w = \rho_w : \text{if } u_w \geq 0 \quad (\text{A.3a})$$

$$\rho_w = \rho_p : \text{if } u_w < 0 \quad (\text{A.3b})$$

and  $A$  is cell face area.

## A.2 Discretization of the Governing Equation

Integrating Eq. (A.1) in time and once in space in the x-direction yields

$$\begin{aligned} & \frac{(\rho\phi V) - (\rho\phi V)^{old}}{\Delta t} + (\rho u\phi A)_e - (\rho u\phi A)_w \\ & + \left\{ \left( A\Gamma_{\phi} \frac{\partial\phi}{\partial x} \right)_e - \left( A\Gamma_{\phi} \frac{\partial\phi}{\partial x} \right)_w \right\} = S_{\phi} V \end{aligned} \quad (\text{A.4})$$

Derivatives in the diffusion terms (the fourth and fifth terms) in Eq. (A.4) can be replaced by the second-order central finite-difference formula by referring to Fig. A.1 as

$$\left( A\Gamma_{\phi} \frac{\partial\phi}{\partial x} \right)_e \approx A_e \Gamma_{\phi e} \frac{\phi_E - \phi_P}{\Delta x_E} = D_e (\phi_E - \phi_P) \quad (\text{A.5a})$$

$$\left( A\Gamma_{\phi} \frac{\partial\phi}{\partial x} \right)_w \approx A_w \Gamma_{\phi w} \frac{\phi_P - \phi_W}{\Delta x_W} = D_w (\phi_P - \phi_W) \quad (\text{A.5b})$$

where  $D_e \equiv \frac{A_e \Gamma_{\phi e}}{\Delta x_E}$  and  $D_w \equiv \frac{A_w \Gamma_{\phi w}}{\Delta x_W}$  are "diffusion link coefficients" and  $\Delta x_E$  and  $\Delta x_W$  are distances from  $P$  to  $E$  and  $W$  to  $P$ , respectively. Since  $\Gamma_{\phi e}$  and  $\Gamma_{\phi w}$  are evaluated at the cell faces where no dependent variable is stored except for the velocities, suitable function should be used to interpolate the values. On the other hand, the convection terms in Eq. (A.4) is evaluated by the upwind values such that

$$(\rho u\phi A)_e \approx C_e \phi_P : \text{if } C_e \geq 0 \quad (\text{A.6a})$$

$$(\rho u\phi A)_e \approx C_e \phi_E : \text{if } C_e < 0 \quad (\text{A.6b})$$

For the convection term at the west cell face can be expressed in the same fashion.

To reduce computational difficulty, the source term in Eq. (A.4) is linearized in the form

$$S_\phi V = Su_\phi + Sp_\phi \phi_P \quad (\text{a.7})$$

Introducing the following notation,

$$[a,b] \equiv \max(a, b) \quad (\text{A.8})$$

as

$$(\rho u \phi A)_e \approx [0, C_e] \phi_P + [0, -C_e] \phi_E \quad (\text{A.9a})$$

and

$$(\rho u \phi A)_w \approx [0, C_w] \phi_W + [0, -C_w] \phi_P \quad (\text{A.9b})$$

and using Eqs. (A.5) to (A.7), Eq. (A.4) can be written as

$$\begin{aligned} \dot{M}_\phi - \dot{M}_\phi^{old} \phi_P^{old} + [0, C_e] \phi_P + [0, -C_e] \phi_E - [0, C_w] \phi_W - [0, -C_w] \phi_P \quad (\text{A.10}) \\ - D_e(\phi_E - \phi_P) + D_w(\phi_P - \phi_W) = Su_\phi + Sp_\phi \phi_P \end{aligned}$$

where

$$\dot{M}_\phi = \frac{\rho V}{\Delta t} \quad \text{and} \quad \dot{M}_\phi^{old} = \frac{\rho^{old} V^{old}}{\Delta t}$$

Superscript *old* represents the value at the previous time level.

Collecting terms with respect to the cell location, Eq. (A.10) can be rewritten as

$$a_P \phi_P = a_E \phi_E + a_W \phi_W + SU_\phi + \dot{M}_\phi^{old} \phi_P^{old} \quad (\text{A.11})$$

Equation (A.11) can easily be extended to three-dimensional flows such that

$$a_P \phi_P = a_E \phi_E + a_W \phi_W + a_N \phi_N + a_S \phi_S + a_H \phi_H + a_L \phi_L + SU_\phi + \dot{M}_\phi^{old} \phi_P^{old} \quad (\text{A.12})$$

where subscripts H and L represent the upper (High) and lower (Low) cell center in the  $\theta$

direction.

### A.3 Modification for Non-Orthogonal Grid

It is required to modify the convective terms in Eqs. (A.6) to evaluate the net flux across the cell faces when the control cell is not orthogonal. Such example is illustrated in Fig. A.2. For the non-orthogonal grid, the convective flux across the south cell face  $C_s$ , for example is computed as

$$C_s = \rho_s A_s v_s - \rho_s A_{sx} u_s \quad (\text{A.13})$$

where  $A_s$  is cell face area projected in the horizontal plane while  $A_{sx}$  is cell face area projected in the vertical plane. It is easily shown that

$$A_{sx} = A_s \tan \alpha \quad (\text{A.14})$$

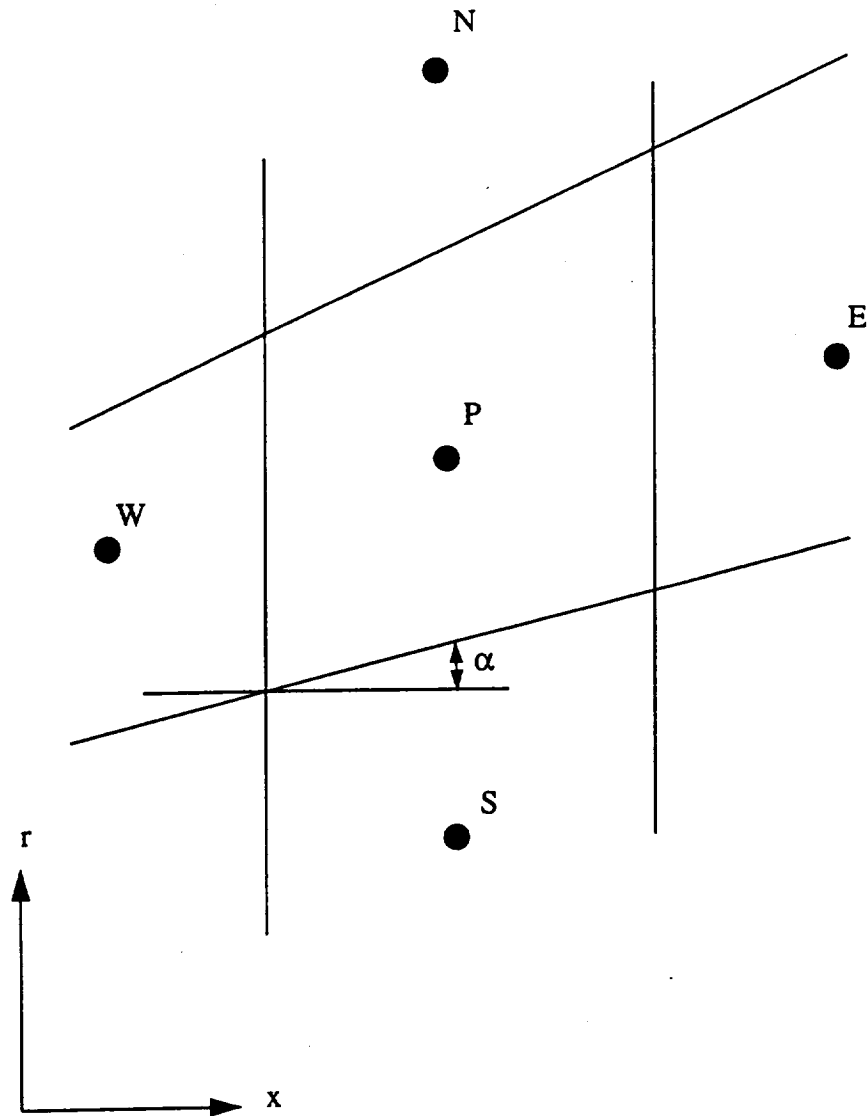


Fig. A.2 Non-orthogonal grid